

**MODELING THERMOHYDROLOGICAL-MECHANICAL
BEHAVIOR OF GRANULAR BENTONITE IN A
LABORATORY COLUMN TEST**

Prepared for

**U.S. Nuclear Regulatory Commission
Contract No. NRC-HQ-12-C-02-0089**

Prepared by

**Stuart Stothoff
Chandrika Manepally
Goodluck Ofoegbu
Biswajit Dasgupta**

**Center for Nuclear Waste Regulatory Analyses
San Antonio, Texas**

and

Randall Fedors

**U.S. Nuclear Regulatory Commission
Washington, DC**

January 2015

ABSTRACT

This report describes numerical modeling performed as part of participation by the U.S. Nuclear Regulatory Commission (NRC) and the Center for Nuclear Waste Regulatory Analyses (CNWRA[®]) in the **Development of Coupled Models and Their Validation Against Experiments** (DECOVALEX) 2015 project. Several groups, including NRC/CNWRA, participated in the modeling exercise under DECOVALEX 2015 Task B1, which has an overall objective of understanding the thermohydrological-mechanical (THM) processes relevant to the performance of a nuclear waste disposal design that includes a bentonite buffer in an argillaceous host rock. Task B1 involves modeling THM processes in (i) the host rock (HE-D heater test), (ii) buffer material (column of granular bentonite used as a buffer for the HE-E test), and (iii) integrated buffer materials and host rock (HE-E heating experiment).

The focus of this report is modeling a laboratory experiment that measured THM processes in a column of granular bentonite (used as a physical-chemical buffer) when subject to heating and hydration. The laboratory column test was designed to mimic the boundary conditions for the buffer material in the HE-E test by prescribing the temperature of the heater at the bottom and a source of hydration (host rock rewetting) at the top. In the HE-E test, the heater is a horizontal cylinder in a buffer-filled drift, with radial rewetting from the host rock. The column test is analogous to accelerated rewetting in the column above the heater. The HE-E test is likely to evolve more slowly than the column test, because the host rock may not be able to supply water as quickly as the column test apparatus.

The modeling approach couples two existing simulators, *xFlo* (which models thermohydrological processes) and FLAC (which models mechanical processes with a user-defined constitutive model for unsaturated expansive soils). Comparisons of measured temperature and relative humidity at three probe locations with model results indicated that the *xFlo* model, in general, is able to adequately represent the moisture redistribution during the thermal phase. However, comparison of water intake measurements indicated that the *xFlo* model poorly represented moisture redistribution during the injection phase. Subsequent analysis suggests that omitting a porous plate above the bentonite in the model strongly affected the simulation results. Comparison of the measured and calculated axial pressures indicates that the mechanical model qualitatively represents the mechanical response. Current constitutive relationships describing flow in *xFlo* may need revision to better account for changes in the bulk hydraulic conductivity as the granular bentonite macro- and microporosity structure evolves with changes in moisture content.

In addition, this report also discusses current efforts to improve the representation of complex swelling behavior of the buffer in numerical models by processes at a pore scale (macro- and micropores). THM modeling capabilities are being enhanced in preparation for the next step of Task B1, which involves modeling the HE-E Test. The HE-E Test focuses on THM behavior of the buffer and its interaction with the host rock. Several conceptual models and constitutive relationships that account for flow at all pore-scales available in literature were examined. One or more of these models could be used to augment *xFlo* capabilities. Staff considerations regarding (i) several potential augmentations to *xFlo* and (ii) procedures to better link *xFlo* and FLAC are also discussed.

CONVERSION FACTORS

Length, pressure and temperature conversions have been included in the text. The conversions for other parameters are provided in this table.

Name	SI Unit	Conversion
Density	1 g/cc 1 kg/m ³	= 0.036 lb _m /in ³ = 0.06243 lb _m /ft ³
Heat transfer rate	1 W	= 3.4123 Btu/h
Length	1 cm 1 m	= 0.394 in = 3.28 ft
Permeability	1 m ²	= 10.76 ft ²
Power	1 W	= 3.412 Btu/h
Pressure and Stress*	1 N/m ² (1 Pa) 1 MPa	= 0.000145 psi = 145 psi
Specific heat	1 kJ/Kg.K	= 0.2389 Btu/lb _m .°F
Thermal conductivity	1 W/m.K	= 0.57782 Btu/h.ft.°F
Temperature	T °C	°F = 1.8 × T °C + 32
Viscosity (dynamic)†	1 N.s/m ²	= 5.8016 × 10 ⁻⁶ lb _f .h/ft ²
Mass	1 g	= 0.002 lb _m
Physical Constants		
Gravitational Acceleration (Sea Level)		$g = 9.807 \text{ m/s}^2 = 32.174 \text{ ft/s}^2$
*The SI name for the quantity pressure is Pascal (Pa) having units N/m ² or Kg/m.s ²		
†Also expressed in equivalent units of kg/s.m		

CONTENTS

Section	Page
ABSTRACT	ii
CONVERSION FACTORS.....	iii
FIGURES	vi
TABLES	viii
ACKNOWLEDGMENTS	ix
1 INTRODUCTION	1-1
1.1 Description of the Column Experiment	1-1
1.2 Description of the Numerical Modeling Approach	1-3
2 NUMERICAL MODELING OF THE COLUMN TEST.....	2-1
2.1 <i>xFlo</i> Model.....	2-1
2.1.1 Input Parameters	2-1
2.1.1.1 Thermal Conductivity	2-1
2.1.1.2 Water Retention and Relative Permeability Relationship	2-2
2.1.1.3 Hydraulic Conductivity	2-2
2.1.1.4 Klinkenberg Parameter	2-3
2.1.1.5 Water Properties.....	2-3
2.1.2 Boundary and Initial Conditions	2-4
2.1.2.1 Heat Loss (COMSOL Model).....	2-5
2.1.2.2 Heat Loss (<i>xFlo</i> Model)	2-8
2.2 Mechanical Analysis (FLAC) Model.....	2-10
2.2.1 Input Parameters	2-10
2.2.2 Geometrical Model and Boundary and Initial Conditions	2-13
3 RESULTS	3-1
3.1 Thermohydrological Analyses	3-1
3.1.1 Thermal Phase	3-1
3.1.2 Injection Phase	3-5
3.2 Results from Geomechanical Modeling.....	3-14
3.2.1 Change in Porosity	3-14
3.2.2 Axial Pressure.....	3-14
3.3 Conclusions From the Column Study	3-17
4 PREPARATION FOR HE-E TEST MODELING.....	4-1
4.1 Conceptual Model for Flow in Bentonite, Sand/Bentonite Mixtures, and Granular Bentonite Pellets.....	4-1
4.1.1 Swelling and Permeability in Continuous Bentonite	4-3
4.1.2 Sand/Bentonite Mixtures.....	4-5
4.1.3 Bentonite Pellets.....	4-6
4.1.4 Gas Flow in Bentonite.....	4-6
4.1.5 Liquid Flow in Bentonite.....	4-7
4.2 Constitutive Models for TH Processes in Bentonite Media.....	4-8
4.2.1 Multicontinuum Retention	4-9
4.2.2 Multicontinuum Permeability.....	4-13
4.2.3 Multicontinuum Vapor Diffusion	4-14

CONTENTS (continued)

Section	Page
4.2.4 Multicontinuum Thermal Capacity and Conductivity	4-14
4.2.5 Threshold Gradients and Flexible Flux Definitions	4-18
4.3 Potential Modifications to xFl_0	4-21
4.4 Proposed Modifications to Link xFl_0 and FLAC	4-22
5 SUMMARY	5-1
6 REFERENCES	6-1

FIGURES

Figure	Page
1-1 Column Test Cell (A) Before Being Wrapped With the Insulation Material and (B) With Improved Insulation	1-2
1-2 Exchange of Information Between <i>xFlo</i> and FLAC/FLAC3D Models	1-4
2-1 COMSOL Model Domain With Thick Insulation	2-6
2-2 Temperature Contours (Yellow Through Red) and Streamlines (Gray) Near the Heater As Calculated by COMSOL for the Thin Insulation Model	2-7
2-3 <i>xFlo</i> Model Domain for Heater Phase 1 (Left) and Other Phases (Right)	2-9
2-4 Bishop Parameter χ Versus s Relationship for the Column Test Granular Bentonite Mix	2-11
2-5 Suction Pressure p_s Versus s Relationship for the Column Test Granular Bentonite Mix	2-11
2-6 Preconsolidation Pressure P_c Versus s Model Based on $P_{c0} = 2$ MPa	2-12
2-7 Bulk Modulus K Versus s Model	2-12
3-1 Simulation State at the End of the Thermal Phase	3-2
3-2 Change in State From the Start of Heating to the End of the Thermal Phase	3-3
3-3 Time History of State Variables at Probe Locations Over the Thermal Phase	3-4
3-4 Simulation State at the End of the Injection Phase	3-6
3-5 Change in State From the Start of Heating to the End of the Injection Phase	3-7
3-6 Change in State From the Start of Injection to the End of the Injection Phase	3-8
3-7 Time History of State Variables at Probe Locations Over the Thermal and Injection Phases	3-9
3-8 Time History of Cumulative Inflow Over the Injection Phase	3-11
3-9 Simulation State at the End of the Injection Phase With a Porous Plate	3-12
3-10 Time History of State Variables at Probe Locations Over the Thermal and Injection Phases With Porous Plate	3-13
3-11 Contours of Calculated Vertical Deformation at the End of Testing	3-15
3-12 Contours of Void Ratio Change, Showing Areas of Void Ratio Increases Relative to the Initial Void Ratio	3-15
3-13 Contours of Void Ratio Change, Showing Areas of Void Ratio Decreases Relative to the Initial Void Ratio	3-16
3-14 Calculated and Measured Axial Pressure Histories at the Top of the Bentonite Column, Showing Results for the Entire Test History	3-16
3-15 Calculated and Measured Axial Pressure Histories at the Top of the Bentonite Column, Showing Results for the Infiltration Test Phase	3-18
4-1 Conceptual Description of Bentonite Pore Structures	4-2
4-2 Electrostatic Component of Disjoining Pressure Compared to Compression	4-4
4-3 Bulk Water Retention as a Function of Capillary Pressure for Several Data Sets	4-12
4-4 Estimated Gas and Liquid Permeability, Scaled by Relative Permeability, as a Function of Saturation for FEBEX Bentonite	4-15
4-5 Measured Thermal Conductivity for FEBEX Bentonite at Various Void Ratios	4-17
4-6 Flux Reductions Stemming From Gradient Reduction in Low-Permeability Media for Selected Reference Hydraulic Gradients	4-19

FIGURES (continued)

Figure		Page
4-7	Wetting-Front Advance (Top) and Total Mass Uptake (Bottom) for a Semi-Analytic Isothermal Model With Parameters for the DECOVALEX Bentonite-Pellet Column	4-20

TABLES

Table		Page
1-1	Experimental Schedule and Boundary Conditions	1-4
2-1	<i>xFlo</i> Input Parameters	2-2
4-1	Areas Identified for Potential <i>xFlo</i> Augmentation	4-22

ACKNOWLEDGMENTS

This report was prepared to document work performed by the Center for Nuclear Waste Regulatory Analyses (CNWRA[®]) for the U.S. Nuclear Regulatory Commission (NRC) under Contract No. NRC–HQ–12–C–02–0089. The activities reported here were performed on behalf of the NRC Office of Nuclear Material Safety and Safeguards, Division of Spent Fuel Alternative Strategies. The report is an independent product of CNWRA and does not necessarily reflect the views or regulatory position of NRC. The NRC staff views expressed herein are preliminary and do not constitute a final judgment or determination of the matters addressed or of the acceptability of any licensing action that may be under consideration at NRC.

The authors would like to thank Gary Walter for his technical review and English Percy for his programmatic review. The authors also appreciate Arturo Ramos for providing word processing support in preparation of this document.

This work was performed in conjunction with the DECOVALEX-2015 collaborative project, Task B1 (see www.decovalex.org). The Column Test experiments, modeled in this report as part of Task B1, have received funding from the European Atomic Energy Community's Seventh Framework Programme (FP7/2007-2011) under grant agreement n° 249681.

QUALITY OF DATA, ANALYSES, AND CODE DEVELOPMENT

DATA: All CNWRA-generated data contained in this report meet quality assurance requirements described in the Geosciences and Engineering Division Quality Assurance Manual.

ANALYSES AND CODES: The computer software FLAC[™] (Itasca Consulting Group, 2011), *xFlo* Version 1.0 β (Painter, 2006), and COMSOL Multiphysics[®] were used in the analyses contained in this report. *xFlo* (Version 1.0 β) is controlled under Technical Operating Procedure (TOP)–018, Development and Control of Scientific and Engineering Software. COMSOL Multiphysics, FLAC and MATLAB are commercial software also controlled under TOP–018. Documentation for the calculations can be found in Scientific Notebooks 1103E (Ofoegbu and Dasgupta, 2014) and 1177 (Stothoff, 2014).

REFERENCES

Itasca Consulting Group. “FLAC V 7.0, Fast Lagrangian Analysis of Continua, User’s Guide.” Minneapolis, Minnesota: Itasca Consulting Group. 2011.

Ofoegbu, G.I. and B. Dasgupta. “Development of Constitutive Relations for Unsaturated Soil and Thermal-Hydrological-Mechanical Coupling.” Scientific Notebook No. 1103E. San Antonio, Texas: Center for Nuclear Waste Regulatory Analyses. 2014.

Painter, S. “*xFlo* Version 1.0 β User’s Manual.” San Antonio, Texas: Center for Nuclear Waste Regulatory Analyses. 2006.

Stothoff, S. “*xFlo* Development and Analyses”, Scientific Notebook No. 1177. San Antonio, Texas: Center for Nuclear Waste Regulatory Analyses. 2014.

1 INTRODUCTION

The **Development of Coupled Models and Their Validation Against Experiments** (DECOVALEX) project is an international collaboration of modeling teams focused on modeling thermal-hydrological-mechanical-chemical (THMC) processes associated with the deep geologic disposal of high-level radioactive waste and spent nuclear fuel¹. The project works to improve the reliability of modeling tools and performance predictions through comparisons with data from laboratory and large-scale field experiments. An important component of the project is the evolution and improvement of modeling tools through comparisons of different approaches, both within each team and among modeling teams. Task B1, in the current phase of DECOVALEX (D2015), is designed to improve understanding of the thermal-hydrological-mechanical (THM) processes in a bentonite buffer and argillaceous host rock at the Mont Terri Underground Research Laboratory (URL), Switzerland. The task is based on three tests:

- (1) HE-D heating test at Mont Terri (rock only)
- (2) Laboratory column test on granular bentonite (used as a buffer for the HE-E test)
- (3) HE-E heating experiment at Mont Terri (integrating buffer materials and host rock)

The HE-E test is an *in-situ* experiment that is part of the Performance of Engineered Barrier Systems (PEBS) project, funded by the seventh framework project of the European Commission (Gaus, et al., 2014). The modeling of the HE-D test was summarized in a previous milestone (Ofogebu, et al., 2013a).

This report provides a current snapshot of the progress of the NRC/CNWRA team in modeling swelling clays used for buffer materials. The report summarizes work related to (i) developing a numerical model for the column test for the granular bentonite (Chapters 2 and 3) and (ii) developing an approach to represent thermohydrological (TH) behavior of swelling clays at a pore-scale (macro- and micropores) in *xFlo* (Chapter 4) for the next task (HE-E test). The modeling process is iterative; therefore, insights in this report and gained in subsequent HE-E test modeling may be used to update the *xFlo*/FLAC modeling tool. As the *xFlo*/FLAC modeling tool evolves, revisiting the column test analyses may be warranted.

1.1 Description of the Column Experiment

The laboratory column test was designed to mimic the boundary conditions for the buffer material in the HE-E test by prescribing temperature of the heater at the bottom and a source of hydration (host rock rewetting) at the top (Villar, et al., 2012, 2014). Compared to a field test, a laboratory test has the advantage of identifying and quantifying THM processes in a shorter duration with relatively less uncertainty regarding the boundary conditions. Although the column tests included both granular bentonite and sand/bentonite mixtures, the scope of the DECOVALEX task (and this report) was limited to modeling the column test containing granular bentonite. The granular bentonite used in this test corresponds to a mixture proposed for use in the Swiss disposal concept. This material contains sodium bentonite MX-80 from Wyoming. The granular bentonite (shown in Figure 1-1) has an initial water content of 6.4 percent (liquid saturation of 22 percent). Thermal conductivity measurement at room temperature, using the transient hot wire method, resulted in a value of 0.12 W/m-K for the granular bentonite.

¹<http://decovallex.org/index.html>

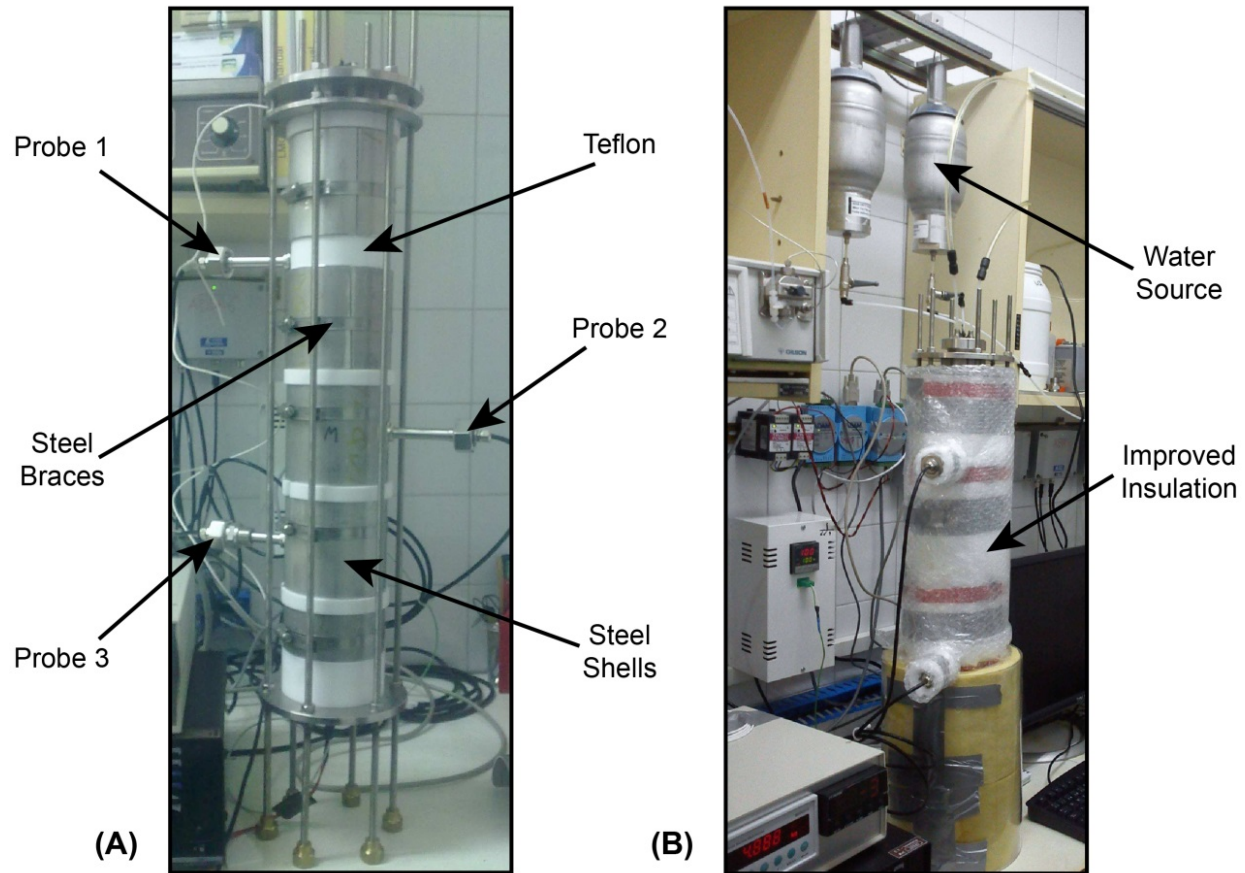


Figure 1-1. Column Test Cell (A) Before Being Wrapped With the Insulation Material and (B) With Improved Insulation

The cylindrical cells used in the experiment had a nominal internal diameter of 7 cm [2.76 in] and length of 50 cm [19.7 in] (Figure 1-1). The cell walls were made of Teflon®. The outer cell wall was covered with semicylindrical steel shells to avoid the deformation of Teflon caused by bentonite swelling. The shells were, in turn, wrapped in insulation wool to reduce heat loss from the cell walls. The bottom part of the cell had a planar stainless steel heater. The upper part consisted of a cooling chamber that circulated water at room temperature, thus ensuring a nearly constant temperature difference between top and bottom of the column (room temperature fluctuated diurnally and seasonally). For the injection phase, water was injected into the column through the upper part of the cell. Synthetic saline water was used for hydration, and was a sodium-rich solution with a composition similar to the Opalinus Clay formation pore water.

The heating and hydration phases in the column test were as follows:

1. Heating Phase 1: The bottom heater temperature was set to 100 °C [212 °F] and the column was insulated with dense foam (termed as “thin insulation” in this report).
2. Improved Insulation Phase: The bottom heater temperature remained set to 100 °C [212 °F] but the insulation material was replaced to mitigate excessive lateral heat loss. The new insulation was Superwool, covering the entire column, with an additional outer

layer of ISOVER material placed from the lowest probe to the countertop (Figure 1-1). The combination of Superwool and ISOVER is termed “thick insulation” in this report.

3. Heating Phase 2: The heater temperature was increased to 140 °C [284 °F].
4. Hydration Phase: Saline water was introduced via an injection tube at the top of the cell. The water was supplied from a pressure bladder surcharged with a pressure of 0.01 MPa [0.1 bar] above atmospheric. The bladder was elevated above the core. The water composition was similar to the Opalinus Clay formation pore water.

Temperature and relative humidity were simultaneously measured at three locations: Probe 1 placed at 40 cm [15.7 in] from the bottom, Probe 2 at 22 cm [8.7 in] and Probe 3 at 10 cm [3.9 in]. The water intake was measured by means of an electronic load cell measurement system. A ring load cell was used to determine the axial pressure generated during the test.

1.2 Description of the Numerical Modeling Approach

The THM model is implemented in a two-dimensional (2-D) axisymmetric coordinate system centered along the axis of the column. Four test phases are included in the model, as specified in Table 1-1.

Two different simulators were used to represent the coupled THM processes. TH processes were modeled using *xFlo*. Four simulations were performed, with the final state from one simulation used as the initial condition for the next. Geomechanical processes were modeled using FLAC with the input for TH conditions taken from the sequence of state outputs calculated by *xFlo*; the equivalent version of FLAC for three spatial dimensions, FLAC3D, will be coupled to *xFlo* for three-dimensional problems. A 2-D axisymmetric model was developed for *xFlo*, representing the bentonite, heater, Teflon cylinder, steel bands, and insulation. The FLAC model used only the portion of the grid representing the bentonite, without considering other materials. A detailed description of the grid is provided in Section 2.1. The exchange of information between the *xFlo* and FLAC/FLAC3D models is illustrated in Figure 1-2.

This phase of the modeling was, in part, intended to assess the magnitude of potential total porosity changes stemming from bentonite displacement, and the porosity output from FLAC was not used to update total porosity in *xFlo* (denoted by a dashed line in Figure 1-2) for the column test. Total porosity refers to the sum of micro- and macroporosity. Micro- and macroporosity may be more directly related to TH constitutive properties than total porosity, and any constitutive relationship partitioning total porosity into micro- and macroporosity (and developing associated TH constitutive relationships) would be implemented internally to *xFlo* in future work. If the magnitude of changes in total porosity warrants explicit representation for the HE-E test, this capability will be developed for modeling the HE-E test.

Phase		Initial Time [hours]	Final Time [hours]	Bottom Boundary Condition		Top Boundary Condition	
				T (°C)		T (°C)	
Heating Phase 1	H1.1	0	1,500	100	$f_w = 0$	22	$f_w = 0$
Improved Insulation	H1.2	1,500	3,524	100	$f_w = 0$	22	$f_w = 0$
Heating Phase 2	H2.1	3,524	5,015	140	$f_w = 0$	22	$f_w = 0$
Hydration	H2.2	5,015	19,850	140	$f_w = 0$	22	$p_w = 0.1192 \text{ MPa}$

T = temperature
 f_w = water flux ($\text{mol}/\text{m}^2/\text{s}$)
 p_w = pore water pressure
 $^{\circ}\text{F} = (1.8 \times T \text{ } ^{\circ}\text{C} + 32)$; 1MPa = 145 psi

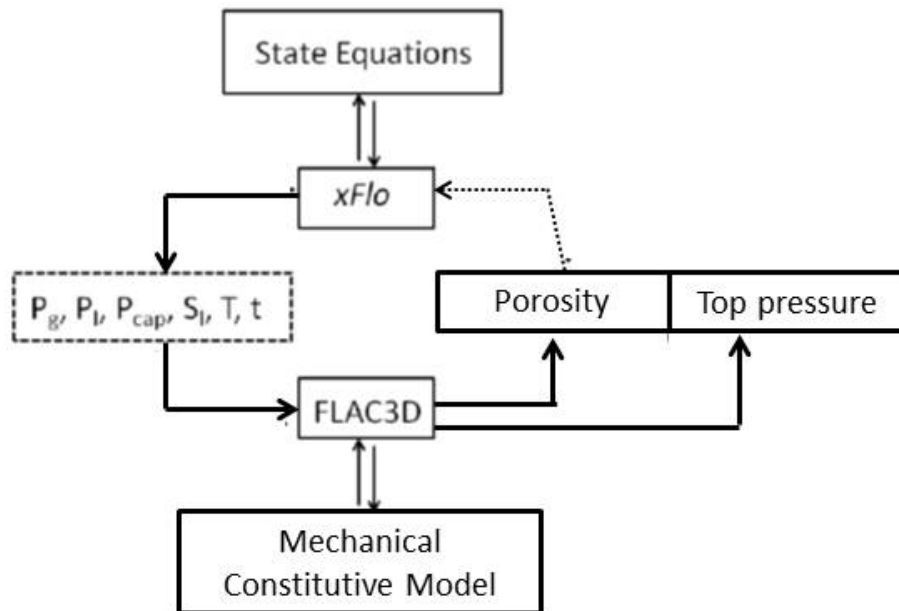


Figure 1-2. Exchange of Information Between *xFlo* and FLAC/FLAC3D Models. P_g = Gas Pressure, P_l = Liquid Pressure, P_{cap} = Capillary Pressure, S_l = Liquid Saturation, T = Temperature, t = Time

2 NUMERICAL MODELING OF THE COLUMN TEST

2.1 *xFlo* Model

The *xFlo* model (Painter, 2006) is an integrated finite volume model developed for the U.S. Nuclear Regulatory Commission (NRC) by the Center for Nuclear Waste Regulatory Analyses (CNWRA[®]) that uses a computational framework similar to the well-known TOUGH model family (Pruess, et al., 2012). *xFlo* considers mass balance of two phases (liquid and gas) and two components (water and air), as well an energy balance. Equilibrium and saturation constraint equations are employed to reduce the equation set to three fully coupled equations for (i) total mass, (ii) gas mass, and (iii) energy.

Air and water are assumed present in both the liquid and gas phases within the bentonite, and *xFlo* solves the fully coupled set of water, air, and energy balance equations. Within the other system components (e.g., steel, Teflon), *xFlo* also solves the mass and energy balance equations, but porosity, hydraulic conductivity, and the vapor diffusion coefficient are each set to zero, with the result that thermal conduction is the only process considered.

2.1.1 Input Parameters

Bentonite is modeled as a single continuum with a single value for porosity and saturated hydraulic conductivity. We recognize that swelling in granular bentonite is a complex process, involving interaction of macro- and micropores given its bimodal pore size distribution (Seiphoori, et al., 2014). Conventional approaches such as van Genuchten (1980) soil water retention relationship and a constant saturated hydraulic conductivity in *xFlo* were insufficient to match the results. The discussion in the following section details the changes made to some of the *xFlo* input parameters listed in Table 2-1.

2.1.1.1 Thermal Conductivity

One of the modeling subtasks was to assess the thermal conductivity based on the laboratory observations. We examined a range of thermal conductivity values to assess sensitivity, including a number of different gridding and insulation options. The range of thermal conductivity values was based on two laboratory tests:

- (1) Villar, et al. (2012) reported a value of 0.12 W/m-K for a sample with a density of 1.5 g/cc and water content of 6 percent.
- (2) Wieczorek and Miehe (2011) reported preliminary values in the range of 0.34 to 0.45 W/m-K for samples at varying density (1.6 to 1.7 g/cc) and water content (dry to 6 percent).

In general, increasing the bentonite thermal conductivity tended to increase temperatures in the bentonite, because larger values of thermal conductivity of bentonite enabled more heat to enter the bentonite rather than contributing to heat loss to the sides or bottom of the experiment. We selected the measured thermal conductivity as our representative value because it provided reasonable temperature distributions given other uncertainties. This process is discussed in Section 3.1. Note that the laboratory experiment had a relatively small range of water contents in the lower portion of the column near the heater, which has the largest temperature gradients. Therefore, the experiment may not provide a strong confirmation of changes in thermal conductivity due to changes in moisture content.

Bentonite Property	Value	Comments
Thermal conductivity (W/m-K)	0.105 (dry) 0.137 (wet)	Measured value for pellets*
Moisture retention curve	—	Measurements.† Capillary pressure accounts for temperature-dependent surface tension
Klinkenberg parameter (Pa)	9.2×10^{11}	—
Intrinsic permeability (m ²)	7.74×10^{-21}	Calculated from saturated hydraulic conductivity measurement‡,‡
Gas tortuosity	2	Artificially enhanced vapor diffusion

*Villar, M.V., P.L. Martin, R. Gomez-Espina, F.J. Romero, and J.M. Barcala. "THM Cells for the HE-E Test: Setup and First Results." PEBS Report D2.2.7a. Madrid, Spain: Long-Term Performance of Engineered Barriers Systems Project. 2012.
†Rizzi, M., A. Seiphooori, A. Ferrari, D. Ceresetti, and L. Laloui. "Analysis of the Behaviour of the Granular MX-80 Bentonite in THM-Processes." AN 12-102. Wettingen, Switzerland: Nagra. 2012.
‡Karnland O., U. Nilsson, H. Weber, P. Wersin. "Sealing Ability of Wyoming Bentonite Pellets Foreseen as Buffer Material—Laboratory Results." *Physics and Chemistry of the Earth*. Vol. 33. pp. S472–S475. 2008.

By default, *xFlo* scales thermal conductivity from fully unsaturated to fully saturated using the square root of saturation (Painter, 2006). We selected a dry thermal conductivity of 0.105 W/m-K and wet thermal conductivity of 0.137 W/m-K, so that the measured value of 0.12 W/m-K at saturation of 0.22 is estimated using the relation for thermal conductivity saturation function in *xFlo*.

2.1.1.2 Water Retention and Relative Permeability Relationship

The moisture retention properties are based on the measured values in Rizzi, et al. (2012). The van Genuchten model (1980) is used, assuming that the retention relationship describing capillary pressure is derived at a reference temperature of 20 °C [68 °F]. At other temperatures, capillary pressure is multiplied by the ratio of surface tensions under the actual and reference temperatures. Scaling capillary pressure by surface tension accounts for the change in the shape of the water/air meniscus with changing surface tension, and is a common approach in multiphase applications. Vapor transport in bentonite turned out to be sensitive to this temperature-dependent adjustment under the moisture and temperature conditions in the experiment, because relative humidity strongly depends on the capillary pressure in relatively dry porous media. In *xFlo*, relative permeability in the liquid phase is related to liquid saturation by combining van Genuchten's relation with Mualem's (1976) model (Painter, 2006).

2.1.1.3 Hydraulic Conductivity

Hydraulic conductivity was represented differently in the thermal phase and the injection phase for most of the modeling work, until a porous plate at the top of the column was appropriately represented. Based on our preliminary modeling, moisture redistribution occurs primarily by vapor diffusion in the thermal phase, but liquid transport dominates in the injection phase. Vapor transport is not sensitive to hydraulic conductivity. As such, the precise value of hydraulic conductivity does not influence moisture redistribution significantly in the thermal phase (as long as hydraulic conductivity is small enough that vapor transport dominates gravity drainage) but is important in the injection phase. The nominal saturated hydraulic conductivity during the thermal phase is based on interpolation of laboratory experiments by Rizzi, et al. (2012).

A more complete model would account for changes in hydraulic conductivity due to swelling during injection, but such a model has not yet been implemented in *xFlo*. As discussed in more detail in Section 3.2, the nominal saturated hydraulic conductivity value was multiplied by an artificial scaling factor (equal to 20) during the injection phase to approximately capture the observed water inflow. Section 3.2 discusses the limitations of this approach. Subsequent modeling revealed that the porous plate at the top of the column greatly increased inflow by spreading water over the top surface of the column, and the scaling factor was no longer needed.

2.1.1.4 Klinkenberg Parameter

Bentonite permeability is likely to be larger at low water saturations than at high water saturations, because the macropore space increases as the bentonite grains shrink. This change in pore structure implies that unsaturated permeability may be significantly larger than permeability calculated using the measured saturated hydraulic conductivity, unlike the case for porous media composed of nonswelling grains. This phenomenon is especially pronounced in a medium initially composed of dry bentonite granules. Under the initial conditions of low water content, the granules have a size distribution similar to a loamy sandy clay, but the pore space around the granules disappears as the granules swell on wetting. On subsequent drying, the same total pore volume is recovered but the connected inter-granule pore space is lost.

xFlo was modified to include the ability to adjust the gas conductivity using a constant Klinkenberg parameter as an initial first-order probing of the effect of saturation-dependent permeability on gas transport. The Klinkenberg model provides a convenient way to adjust the gas conductivity independent of the liquid (intrinsic) permeability. The increased permeability at low water saturations was approximately accounted for by multiplying the gas relative permeability by the Klinkenberg factor. Increased permeability was not considered for liquid transport, because vapor transport dominates under dry conditions.

Adjusting the Klinkenberg parameter provided a means to artificially scale gas conductivity to approximately consider very conductive conditions, as also noted by Rutqvist, et al. (2013). A Klinkenberg parameter 10 orders of magnitude larger than atmospheric pressure will increase gas conductivity by 10 orders of magnitude in the column test. Our numerical calculations indicate that the simulations are insensitive to the Klinkenberg parameter prior to water injection when it is at least 4 or 5 orders of magnitude larger than the atmospheric pressure. Applying the adjusted Klinkenberg model under saturated conditions (e.g., adjacent to the water injection in the imbibition phase) may drastically overestimate gas permeability. Further, a different Klinkenberg parameter may be appropriate if the bentonite was dried after saturating, because the inter-granule pore structure does not return on drying once the granules have merged. These considerations suggest that a more complete representation of the underlying physics may be appropriate for future modeling.

2.1.1.5 Water Properties

Water properties are assumed to be described by National Institute of Standards and Technology Steam Table (e.g., http://enpub.fulton.asu.edu/ece340/pdf/steam_tables.PDF). The gas phase is assumed to be governed by the ideal gas law. Dissolved air is assumed to be in equilibrium with the gas phase through Henry's Law. Water vapor is assumed to be in equilibrium with the liquid phase, considering temperature- and capillary-pressure-dependent vapor pressure lowering using the Kelvin equation.

2.1.2 Boundary and Initial Conditions

Several thermal-related parameters were measured in the laboratory experiment: (i) computer-controlled heater temperature, (ii) energy flux to the heater, (iii) temperatures at three probes, (iv) approximate cooling-bath temperature, and (v) laboratory temperature (during the injection phase). The experiment also measured relative humidity at the three probes, cumulative inflow of water during injection, and axial pressure at the top of the column. The water source was a bladder that was pressurized to 0.01 MPa [0.1 bar] above atmospheric; the difference in elevation between the water surface and the top of the bentonite was not provided.

Boundary and initial conditions for mass balance within the bentonite are straightforward. All materials bordering the bentonite are assumed impermeable except the injection cylinder (during the injection phase). The injection cylinder overlaps the innermost two grid cells at the top of the bentonite. During the injection phase, the injection cylinder is assumed to provide deaerated water at a pressure corresponding to atmospheric pressure plus 0.01 MPa [0.1 bar] (the pressure surcharge in the bladder) plus hydrostatic pressure from 90 cm [35.4 in] elevation difference between the top of the water in the bladder to the top of the bentonite², corresponding to a pressure of 0.12015 MPa [17.4 psi]. Gas is allowed to exit through the injection cylinder. The inlet water is assumed to be at room temperature {fixed at 22 °C [71.6°F]}. The initial bentonite saturation is assumed to be 0.22.

Reported room temperatures varied from 18.5 to 23 °C [65.3 to 73.4 °F] over the duration of the injection test, and at times changed by more than 2 °C [3.6 °F] within 48 hours. This variability should be relatively unimportant for understanding the transport processes in the column, and the model assumed a constant room temperature of 22 °C [71.6°F]. We expect that laboratory temperatures may fluctuate by several degrees within a few hours. The column temperatures equilibrate to the room temperatures within a day, thus fluctuations over a few hours should be unimportant but seasonal fluctuations may affect measured column temperatures. To simplify the analysis, it was assumed that seasonal variations could be ignored. This assumption is partially warranted because differences in lab temperatures have a secondary impact on temperature gradients between the sample and the outside of the insulation—an assumption that may be revisited at a later time.

The long and thin geometry of the bentonite column suggests that the temperature field within the bentonite should be approximately one-dimensional (1-D), especially with the relatively uniform temperatures applied at the top and bottom. However, thermal analysis must consider the effect of conduction within the steel bands supporting the Teflon cylinder and heat loss to the atmosphere. To examine the effect of different thermal boundary condition treatments, we developed a thermal-only model that considered the experimental apparatus in detail using COMSOL Multiphysics (hereafter called the COMSOL model). This provided guidance for selection of the domain and boundary conditions used for *xFlo* thermal analyses. All of the COMSOL and *xFlo* simulations assume a constant room temperature initial condition of 22 °C [71.6°F] throughout the model domain.

²Estimated from Villar et al. (2012) Figure 19

2.1.2.1 Heat Loss (COMSOL Model)

The COMSOL model considers a detailed representation of the column in a two-dimensional (2-D) axisymmetric grid. Above the heater, the COMSOL model considers the same domain as the *xFlo* model, but the COMSOL model also considers components below the heater element. Figure 2-1 illustrates the COMSOL domain with thick insulation and Figure 2-2 illustrates the lower part of the COMSOL domain with thin insulation. The thin insulation model is identical to the thick insulation model, except that the insulation is thinner and extends just to the bottom steel plate.

The COMSOL model is supplied energy at the heater element within the steel domain below the bentonite, and loses energy to (i) specified temperature boundaries set to 22 °C [71.6°F] at the top of the bentonite and top of the domain and (ii) surface-to-ambient radiation along the outer domain boundaries. Sensitivity analyses were performed to examine the effect of different bentonite properties, steel representations, outer boundary conditions, and components included in the domain. Four temperatures were used to assess the effects of different assumptions, at the heater itself and at the three probe locations. Two options were considered for thermal boundary conditions within the air space enclosed by insulation at the column bottom: (i) surface-to-ambient radiation (Option 1 in Figure 2-1) and (ii) thermal conduction in a stagnant air column (Option 2).

From our sensitivity calculations, we concluded that

- The steel shells are extremely important in the overall energy balance (see Figure 2-2). Energy conducts in and out of the bentonite based on the position of the steel and gaps, which will locally affect moisture condensation. The steel shells, 50 to 140 times as conductive as bentonite, carry a much larger fraction of the total axial heat flux than the bentonite.
- Much of the supplied energy is lost below the heater element. Merely adding and subtracting surface area and metal components had a significant effect on the energy balance.
- The boundary conditions outside the insulation should result in insulation surface temperatures between room temperature (maximum heat loss) and the surface-to-ambient-radiation temperature (minimum heat loss, because it does not consider cool air moving past the surface). Surface temperatures are much larger than room temperature near the heater with thin insulation, but are quite similar with thick insulation.
- Reasonably good matches to the observed temperatures were obtained with the bentonite thermal conductivity set to 0.33 W/m/K assuming surface-to-ambient radiation losses, once heat loss below the heater was adjusted to achieve the computer-controlled heater temperatures.
- The lowest steel reinforcing band collects energy from the side of the heater element (and bottom, in thick insulation scenarios) and transports it above the heater. This creates a thermal divide below the actual heater element.
- The central 2.5 cm [0.98 in] of the steel heater where it contacts the bentonite is essentially at the same temperature as the heater element. Temperatures along the top

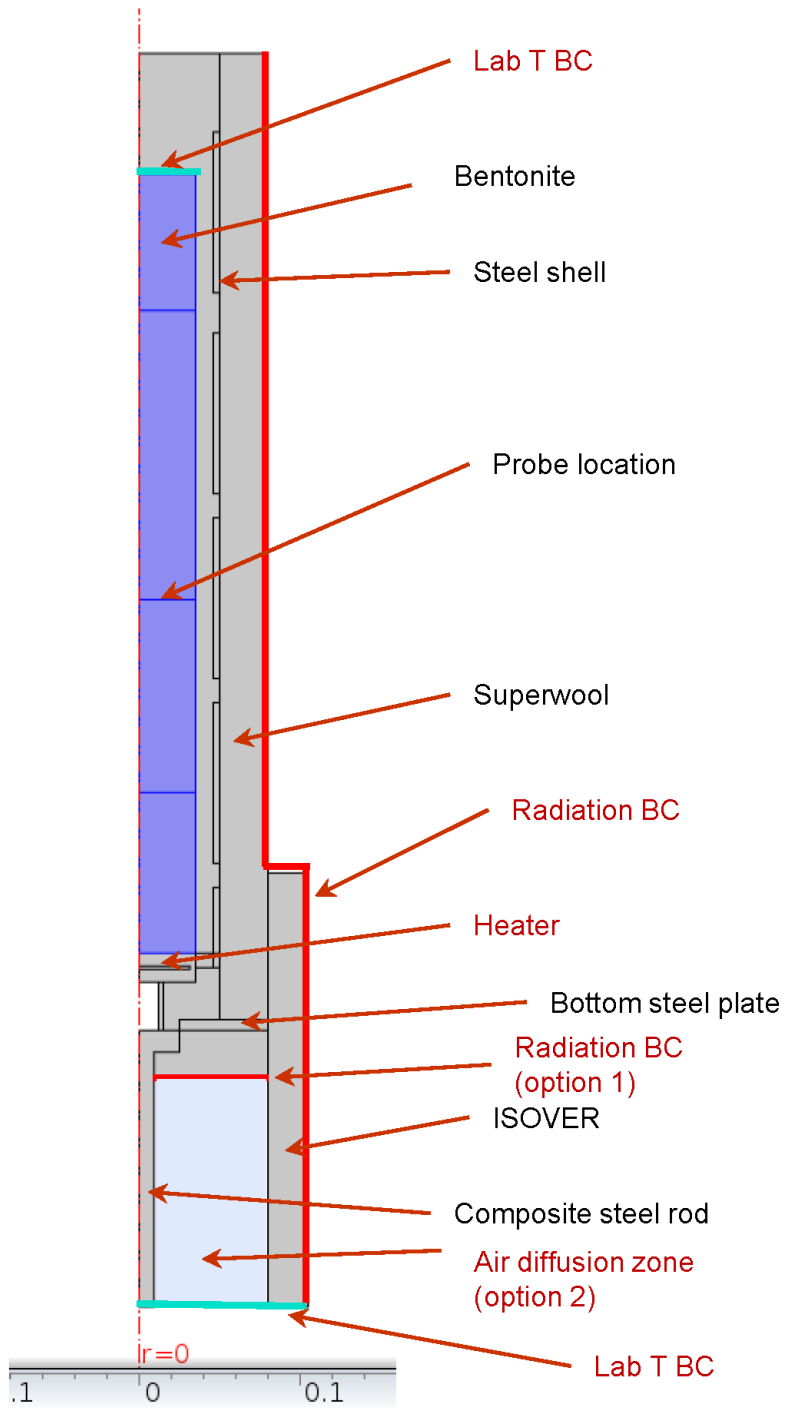


Figure 2-1. COMSOL Model Domain With Thick Insulation

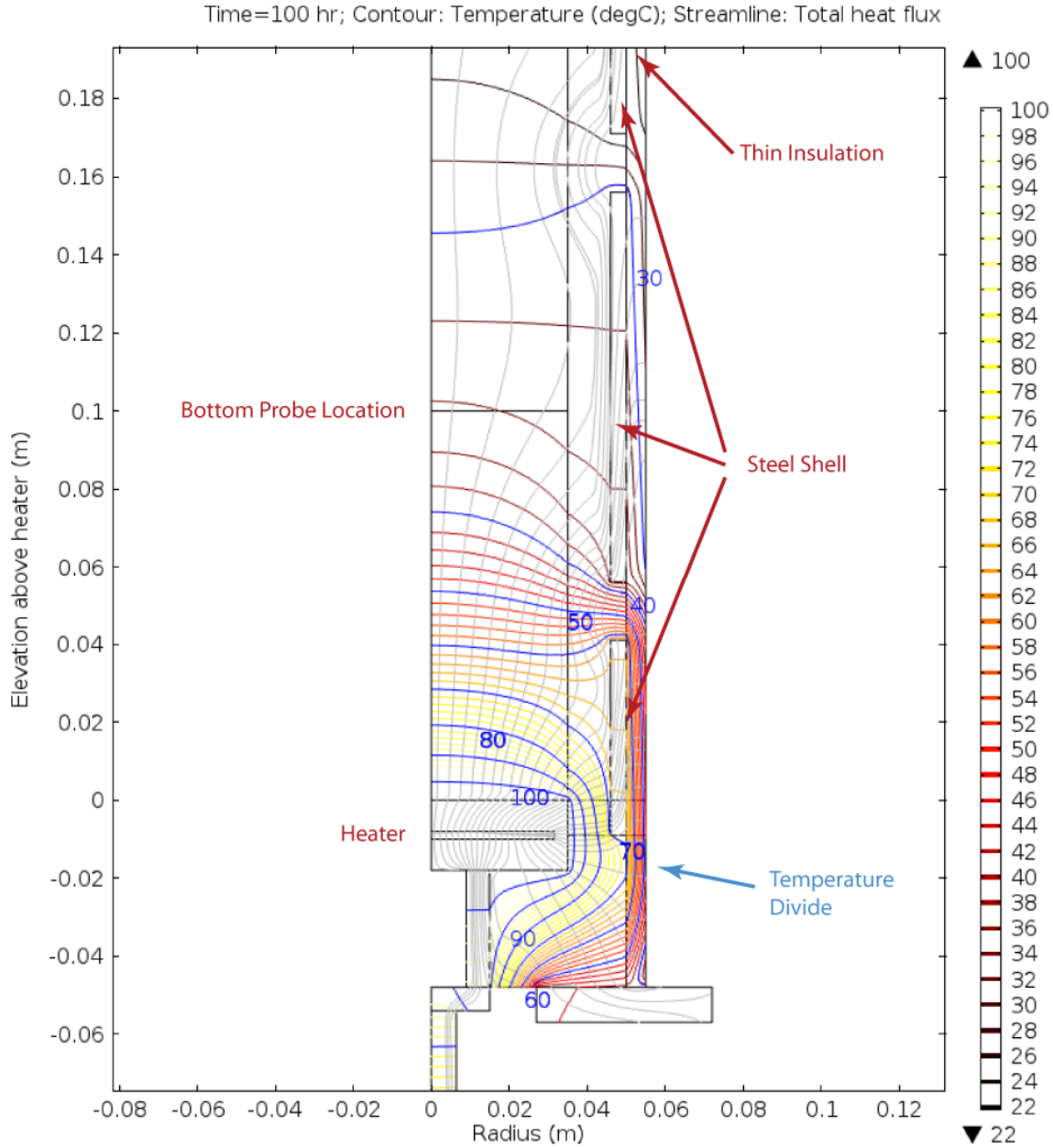


Figure 2-2. Temperature Contours (Yellow Through Red) and Streamlines (Gray) Near the Heater As Calculated by COMSOL for the Thin Insulation Model
 $^{\circ}\text{F} = (1.8 \times T\text{ }^{\circ}\text{C} + 32)$

and outer edges of the steel heater generally are the same to within 1.5 °C [2.7°F]. For the purposes of modeling mass transport in the bentonite, it should be adequate to (i) make the bottom of the domain correspond to the thermal divide elevation and (ii) assign the heater temperature to the inner 3 cm [1.2 in] of the bottom of the domain. This was the strategy used for *xFlo* simulations.

2.1.2.2 Heat Loss (*xFlo* Model)

With the insights gained from the COMSOL modeling, the *xFlo* model is designed such that

- The top of the bentonite is set to room temperature {22 °C [71.6°F]}.
- The domain extends 1.5 cm [0.59 in] below the bentonite, including projections of the steel heater, the Teflon cylinder, the steel reinforcing band, and the insulation. The temperature at the bottom of the domain is either 100 or 140 °C [212 or 284 °F] within a radius of 3 cm [1.2 in] from the axis.
- The computational grid changes in the insulation when the insulation is changed, but the same number of cells are present. The insulation grid cells are simply stretched radially to represent the new insulation configuration, and are assigned new thermal conductivities.
- The *xFlo* model does not include a surface-to-ambient radiation boundary condition akin to the COMSOL boundary condition, so the boundary temperature outside the insulation is set to room temperature.
- Some of the sensitivity tests applied an artificially small thermal conductivity to reduce heat loss over the lower portion of the thin insulation (from the top of the lowest steel band to the bottom of the domain), approximately mimicking surface-to-ambient radiation.

The computational domain for the *xFlo* model is shown in Figure 2-3. With these assumptions, the *xFlo* and COMSOL models produce similar matches to the probe temperatures. However, *xFlo* requires a smaller bentonite thermal conductivity (by about a factor of three) to approximately match probe temperatures. Good matches to the observed temperatures occur for thermal conductivity less than 0.12 W/m/K for *xFlo* (corresponding to the measured value for the granular bentonite) and approximately 0.33 W/m/K for COMSOL [corresponding to the values reported by Wieczorek and Miehe (2011)]. Poor matches are obtained if the models are provided with the opposite thermal conductivity values.

Subsequent verification testing with simplified boundary conditions showed that the COMSOL and *xFlo* models match very well when all boundary conditions are identical. The testing revealed that, in addition to the different treatment of the radiation boundary condition, two factors influenced the discrepancy in thermal conductivity: (i) incorrect grid input to *xFlo* and (ii) subtly different top boundary conditions. A special-purpose MATLAB routine developed to generate the *xFlo* input files calculated interfacial areas that were too small by a factor of two in the radial direction. This gridding error effectively created anisotropy in the thermal conductivity, over-emphasizing axial conduction, and is primarily responsible for the lower estimated thermal conductivity in *xFlo*. A small discrepancy in temperatures at the top of the column resulted from subtle differences in the top boundary condition. The COMSOL model included a temperature boundary condition at the top of the bentonite but extended the steel shell past the temperature condition (see Figure 2-1), while the *xFlo* model stopped the domain at the top of the bentonite. The COMSOL model allowed greater heat exchange between the cold bath and the top steel shell, dropping temperatures at the top of the column relative to the *xFlo* model.

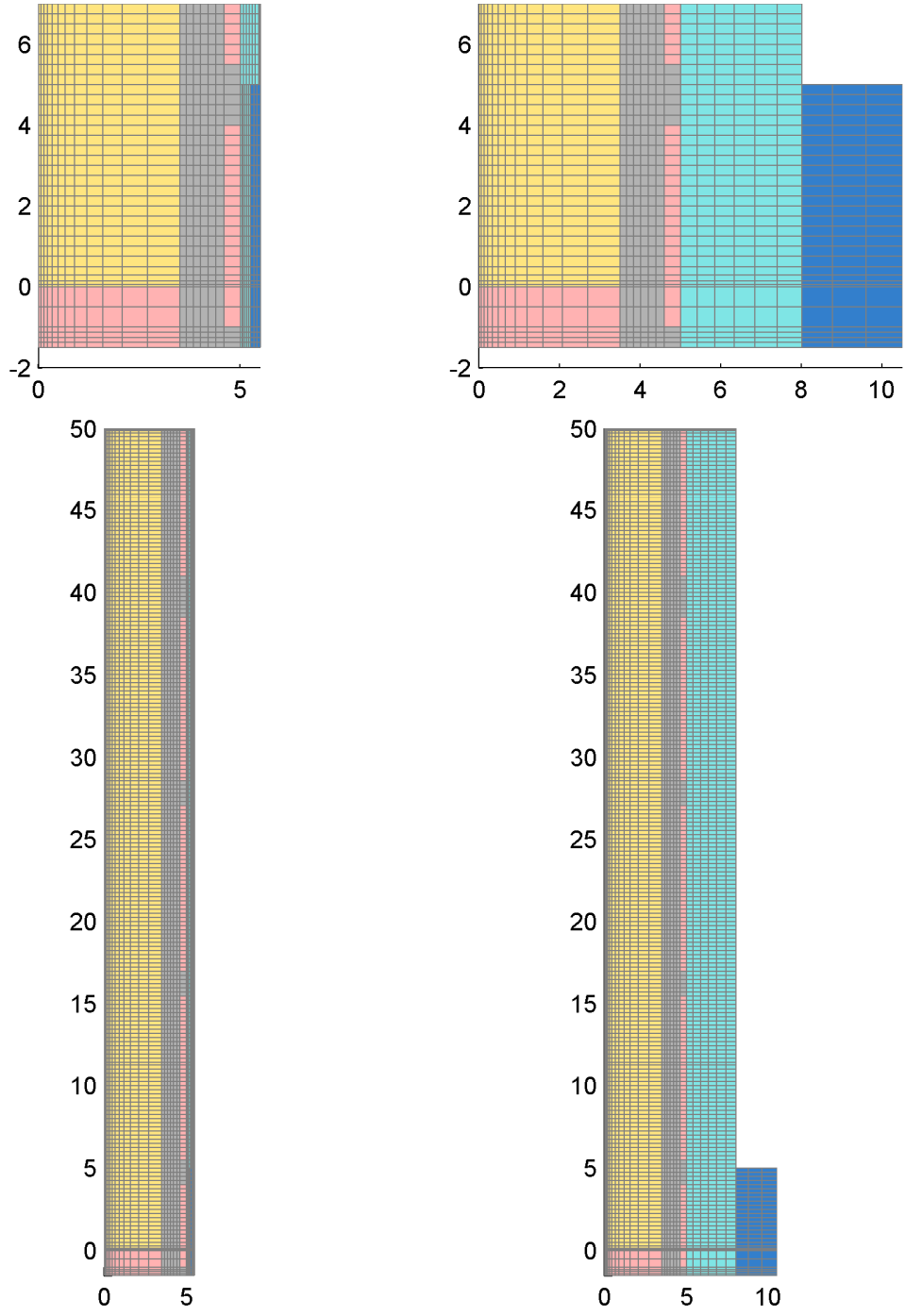


Figure 2-3. *xFlo* Model Domain for Heater Phase 1 (Left) and Other Phases (Right). The Grids at the Top of the Figure Are Enlargements to Better Illustrate the Bottom of the Domain. Bentonite Is Yellow, Teflon Is Gray, Steel Is Pink, and Insulation Is Cyan and Blue.

2.2 Mechanical Analysis (FLAC) Model

The mechanical model uses the temperature, liquid saturation, and gas pressure calculated in the thermohydrological (TH) model as inputs to calculate the mechanical response in terms of deformation (porosity change) and pressure. The mechanical analysis was performed using the MCUS (modified CAM-clay model for unsaturated soils) constitutive model (Ofoegbu, et al., 2013b) implemented for numerical computation using FLAC. As Ofoegbu, et al. (2013b) described, MCUS is based on using the Bishop principle of effective stress to represent the effects of suction on soil stress, incorporates the effects of suction and compaction on mechanical properties, and uses stress-strain relationships based on elasto-plasticity. The model is currently implemented for use with FLAC but will be transitioned to FLAC3D in the future.

2.2.1 Input Parameters

The Bishop parameter χ is set equal to the effective saturation S_e and is described as a function of suction (s) in Figure 2-4. The resulting suction contribution to soil pressure (i.e., suction pressure, p_s) based on the Bishop parameter is shown in Figure 2-5. The suction pressure from this figure was combined with the value of preconsolidation pressure for saturated conditions (P_{c0}) based on data from Rizzi, et al. (2012) to obtain the preconsolidation pressure model shown in Figure 2-6. As Ofoegbu, et al. (2013b) described, the soil bulk modulus (K) is a function of pressure (p) and void ratio, which translates to a variation with s as shown in Figure 2-7. The K - p relationship is influenced by P_{c0} , the unload-reload slope (denoted κ_r), and a fitting parameter K_∞ that represents an asymptotic maximum bulk modulus. The relationship in Figure 2-7 was derived using $K_\infty = 50$ MPa [7250 psi]. An examination of relationships among the various parameters indicated this value to be appropriate. A slightly smaller or larger value could work but could result in inappropriate values for other parameters.

The additional parameters are κ_r , virgin compression slope (λ_s), and reference specific volume ($v_{\text{ref}0}$); which were prescribed as functions of s , as follows (pressure and s in MPa) based on simulated oedometer compression testing and data from Rizzi, et al. (2012); unit swelling potential (α_{cW}), and thermal expansivity (α_{Th}).

$$v_{\text{ref}0} = 2.0 - \frac{s}{175 + 3.7s} \quad (2-1)$$

$$\kappa_r = 0.15 - \frac{s}{5000 + 25s} \quad (2-2)$$

$$\lambda_s = 0.23 + \frac{s}{100 + 20s} \quad (2-3)$$

$$\alpha_{cW} = 0.5 - 1.75(\theta_l - 0.075) \text{ if } \theta_l \geq 0.075; \alpha_{cW} = 0 \text{ if } \theta_l < 0.075 \quad (2-4)$$

$$\alpha_{Th} = 10^{-5} / ^\circ\text{C} \quad (2-5)$$

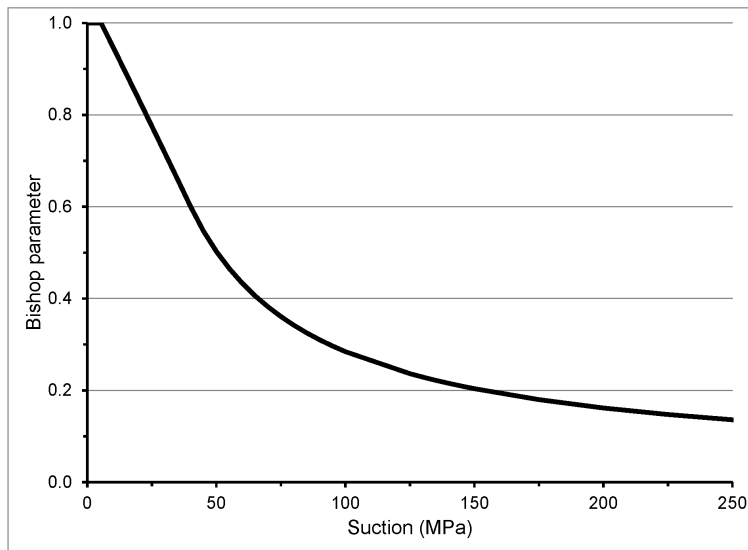


Figure 2-4. Bishop Parameter Versus Relationship for the Column Test Granular Bentonite Mix, Based on Rizzi, et al. (2012) Moisture Retention Curve [1 MPa = 145 psi]

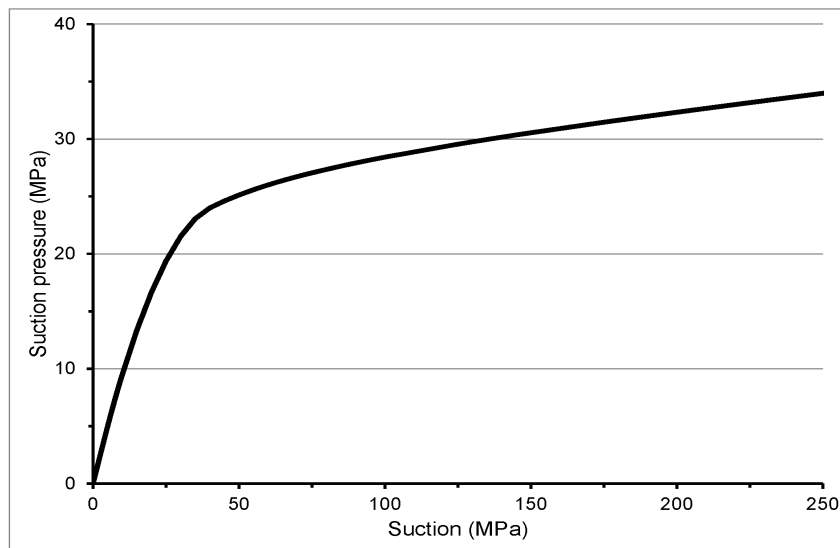


Figure 2-5. Suction Pressure Versus Relationship for the Column Test Granular Bentonite Mix, Based on the - Relationship From Figure 2-4 [1 MPa = 145 psi]

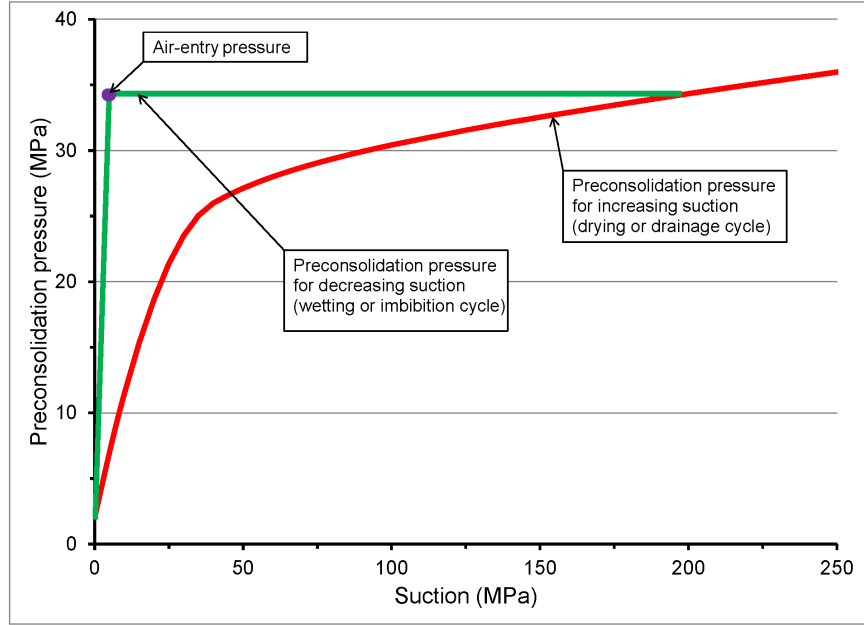


Figure 2-6. Preconsolidation Pressure Versus Model Based on MPa [For Saturated Condition, Based on Rizzi, et al. (2012) Data] and Suction Pressure From Figure 2-5 [1 MPa = 145 psi]

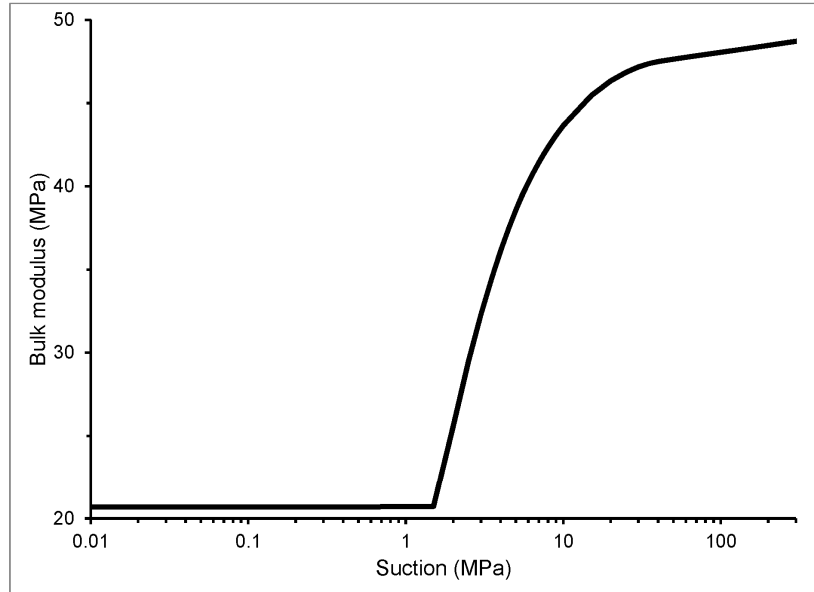


Figure 2-7. Bulk Modulus Versus Model Based on Ofoegbu, et al. (2013b) - Relationship and Parameter Values Described in This Report [1 MPa = 145 psi]

Oedometer free-swelling test results from Rizzi, et al. (2012) indicate an α_{CW} of approximately 2 for the Column Test moisture content (θ_l) range. However, this value of α_{CW} resulted in excessive swelling pressure. Therefore, α_{CW} was reduced to the value shown in Eq. (2-4). Based on a literature search and available data, a different model for shrinkage and swelling is not warranted. Therefore, the same model is used for swelling and shrinkage, which implies full reversibility of swelling and shrinkage strains.

2.2.2 Geometrical Model and Boundary and Initial Conditions

The bentonite column was modeled as an axisymmetric solid of radius 0.035 m [0.115 ft] and height of 0.5 m [1.64 ft], which was discretized into 204 rows of cells of 12 per row. An additional row of relatively stiff cells was placed at the top of the assemblage to represent the top load-cell and was used to capture the axial pressure. The top row was modeled as linear-elastic and was not assigned any TH variables or properties. The 204 rows representing the bentonite were modeled using the constitutive model described in Section 2.2.1.

The base and top of the model were restrained vertically and the lateral boundary was restrained horizontally. An initial compressive stress of approximately 30 MPa [4350 psi] magnitude (i.e., suction pressure from Figure 2-5 for the initial suction of approximately 140 MPa [20300 psi]) was applied in every cell. The initial TH conditions were derived from *xFl*o simulations, as described in Section 2.1.2.

3 RESULTS

3.1 Thermohydrological Analyses

Thermohydrological (TH) analyses are conveniently broken into the thermal period, when mass is neither added nor lost while the column is heated, and the injection phase, when liquid enters and gas escapes while heating continues. The thermal period consists of three phases (described previously in Section 1.1) simulated separately: (i) heating phase 1, (ii) improved insulation, and (iii) heating phase 2, for a total of 5,015 hours. The injection phase is the next 14,835 hours. The last two thermal phases and the injection phase are initialized using the final state from the previous simulation.

3.1.1 Thermal Phase

Figures 3-1 and 3-2 show (i) the system state and (ii) the change in state at the end of the thermal phase calculated by *xFlo* using the best-estimate input parameters. The center top subfigure (temperature) shows the full domain used for the temperature calculations in the thick insulation configuration, and the remaining subfigures show just the bentonite domain. Calculations were performed on half of the domain, but the output is mirrored at the central axis to aid with visualization. The three horizontal lines in each subfigure indicate the probe locations, and the vertical tan bars indicate the position of the steel reinforcement bands. Note that Figure 3-2 uses a symmetric color scale with gray indicating no change, with the positive and negative limits representing the positive and negative of the absolute value of the largest change. Some quantities, such as temperature, only change in one direction. Gauge pressure is absolute pressure minus atmospheric pressure {assumed to be 0.101325 MPa [14.6 psi]}.

The wetting saturation profiles suggest that the steel reinforcement (because of its high thermal conductivity) perturbs the temperature field sufficiently to locally enhance condensation where heat is drawn from the bentonite. This can be seen between the top two probes. The same behavior occurred lower in the profile, but has been erased as the drying zone propagated upward.

Figure 3-3 shows the time history of the state variables during the thermal period at the three probe locations indicated in Figures 3-1 and 3-2. The symbols plotted for relative humidity and temperature are the laboratory measurements. Laboratory room temperature fluctuated over the experiment duration, and the probe measurements differed by as much as 3 °C [5.4 °F] during nominally steady conditions. The temperature symbols are adjusted to remove changes in laboratory temperature from the initial reading using simultaneous changes in all three probes, allowing a better comparison with the *xFlo* assumption of a constant room temperature. Correcting the measurements using the average of the three probes provided a smoother trace than correcting with the provided laboratory room temperatures (which were only available for the injection phase), suggesting that the probe temperatures lag the laboratory temperatures.

Calculated temperatures are slightly below the measured values during heating phase 1, and are somewhat too large in later phases. The indicator of moisture state, relative humidity, suggests that the lower probe is responding approximately correctly during heating phase 1 but is drying too rapidly afterwards. The center and upper probes are responding at approximately the correct pace but are not gaining enough moisture from the bottom of the column. Artificially adjusting the boundary conditions or thermal conductivity to better match the temperatures tends to bring the relative humidity closer to the measured values. It may also be that the

State at end of heating

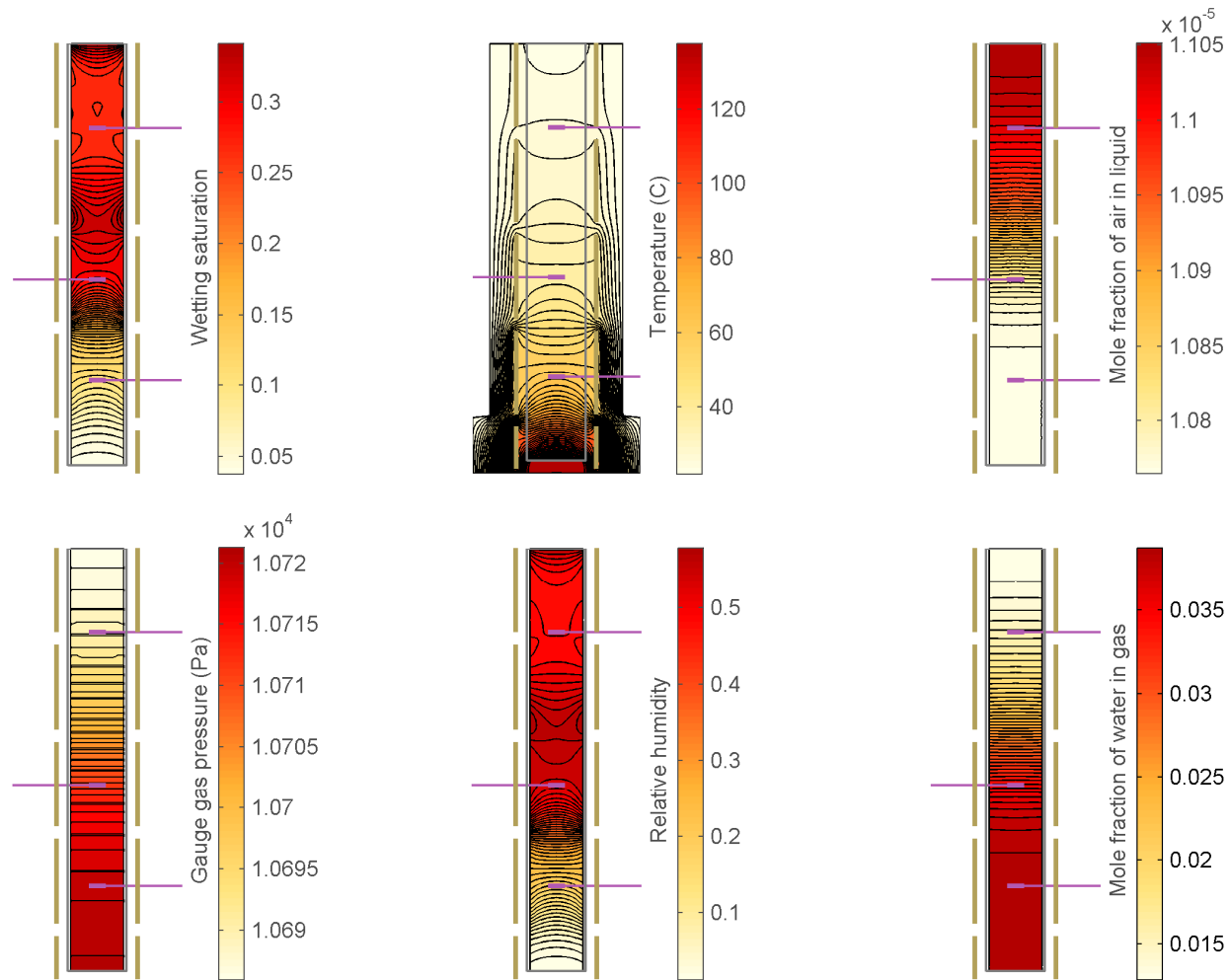


Figure 3-1. Simulation State at the End of the Thermal Phase
 {1 Pa = 0.000145 psi; °F = [1.8 × T °C + 32]}

Cumulative change to end of heating

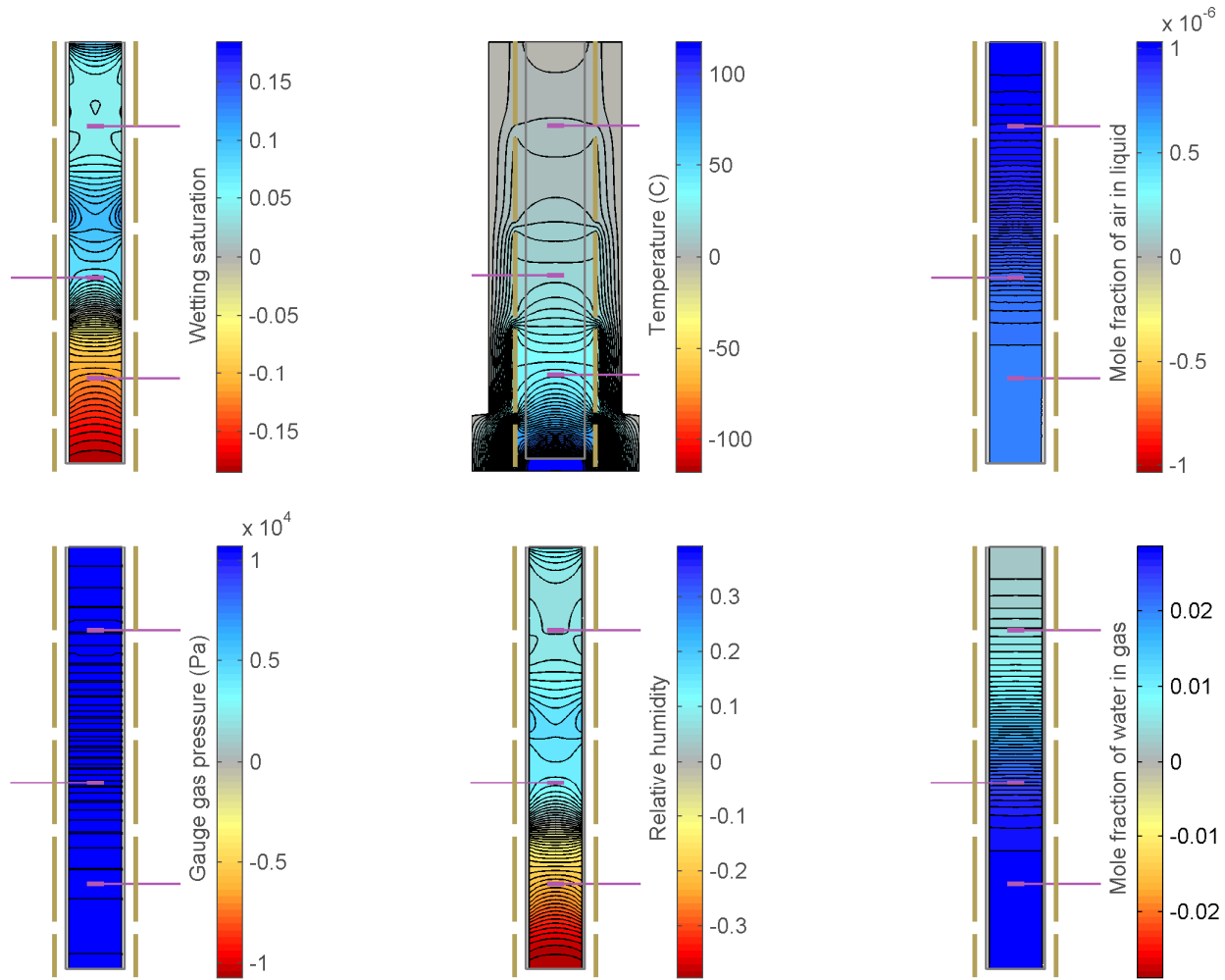


Figure 3-2. Change in State From the Start of Heating to the End of the Thermal Phase
 {1 Pa = 0.000145 psi; °F = [1.8 × T °C + 32]}

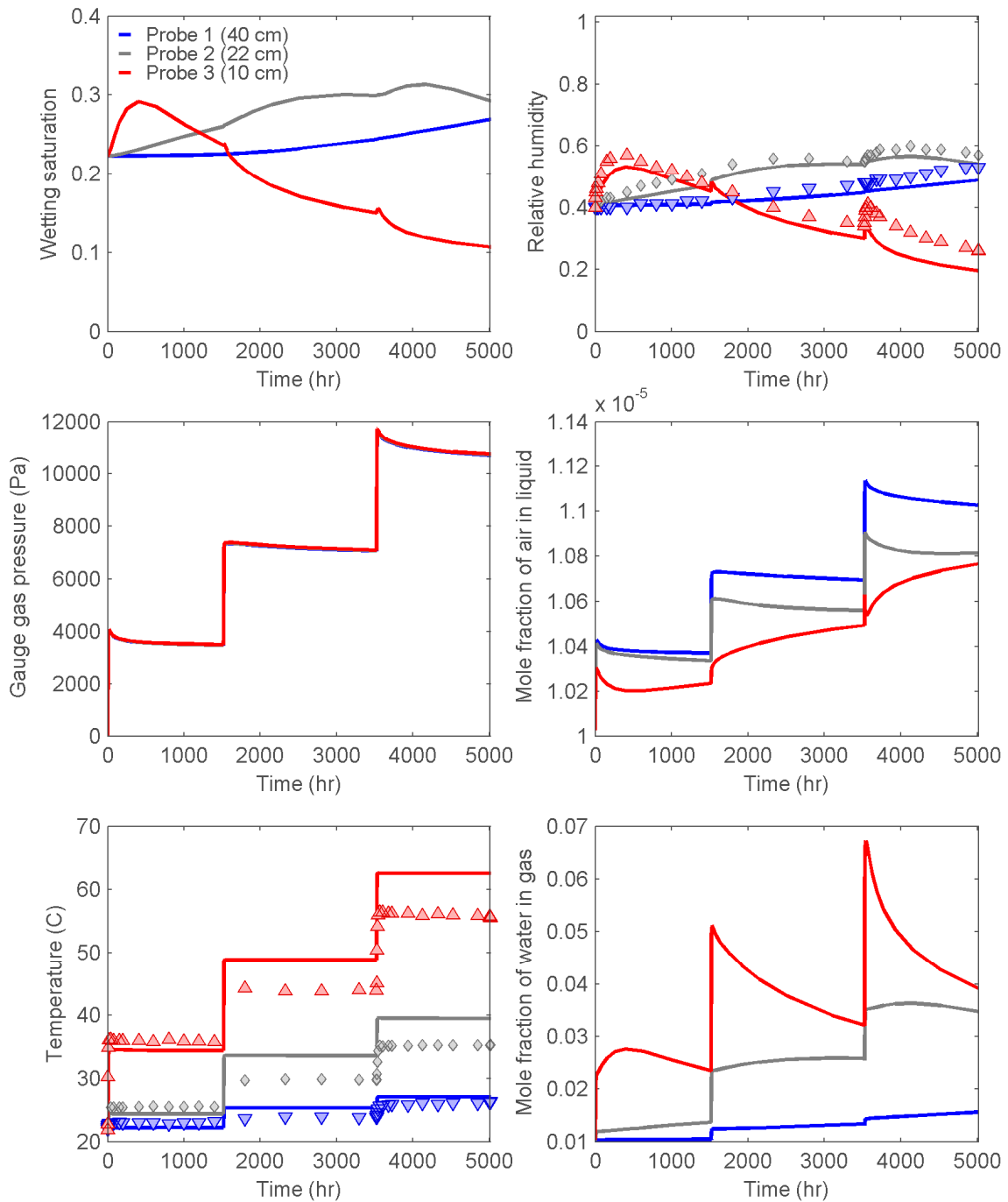


Figure 3-3. Time History of State Variables at Probe Locations Over the Thermal Phase. Symbols Indicate Laboratory Measurements and Lines Indicate Model Results. {1 cm = 0.39 in; 1 Pa = 0.000145 psi; °F = [1.8 × T °C + 32]}

effective vapor diffusion coefficient should be slightly higher as the saturation increases to reflect condensation and evaporation at opposite ends of continuous water pathways within the granules that “short-circuit” the vapor pathway under a thermal gradient (Philip and de Vries, 1957). Ho (2006) estimates that enhanced effective vapor diffusion through a liquid throat ($q_{v,evd}$) is approximately described by

$$q_{v,evd} \approx 10 \frac{A_t}{A_p} q_{v,Fick} \quad (3-1)$$

where $q_{v,Fick}$ is vapor diffusion through Fickian diffusion and A_t and A_p are the area of the throat and air-filled pore space, respectively. Enhanced vapor diffusion is increasingly important relative to Fickian diffusion under wetter conditions, because A_t monotonically increases and A_p monotonically decreases as saturation increases. Enhanced vapor diffusion requires that water is mobile within the connected liquid pathway, which may be a limiting factor for the process in bentonite.

The jumps in gauge gas pressure are approximately 80 percent of the jumps in measured axial pressure.

3.1.2 Injection Phase

Water and air are allowed to move across the top boundary during the injection phase. As discussed in Section 2.1.2, the injection boundary condition explicitly represents the geometry of the injection nozzle. Within the nozzle area, the boundary condition is fully saturated with a specified pressure corresponding to a pressurized bladder elevated above the column. The boundary condition allows liquid and gas exchange within the nozzle, but no mass exchange on the remainder of the column. In most of the modeling work, the nozzle was placed directly on the top of the bentonite, but the resulting inflows were difficult to reconcile with measurements using a reasonable range of parameters. A porous plate was included in the model during later modeling work, with the nozzle placed at the top of the plate, and calculations with this approach provided results that were much closer to measured values.

When the porous plate was neglected, the bentonite saturated hydraulic conductivity was artificially increased to 20 times larger than the measured value. This was done only for the injection phase, because such a large value deteriorated the moisture balance during the thermal phase. This artificial increase in saturated hydraulic conductivity was selected to approximately match the measured cumulative inflow over the injection period. Figures 3-4, 3-5, and 3-6 show (i) the system state at the end of the injection phase, (ii) the change in state from the start of heating to the end of the injection phase, and (iii) the change in state from the start of injection to the end of the injection phase as calculated by *xFlo* using the best estimate input parameters. Figure 3-7 shows the time history of the state variables at the probe locations.

The *xFlo* calculations show essentially no change in the temperature profile during the injection phase. The time history of the measured relative humidity suggests that the *xFlo*-calculated wetting front is smeared relative to the actual laboratory experiment. Water is moving to depth too rapidly at low saturations in the *xFlo* calculations because the elevated saturated hydraulic conductivity permits relatively rapid gravity drainage. The laboratory experiment appears to be essentially saturated behind the front and likely has a quite sharp wetting front, which is more consistent with diffusion-dominated inflow.

State at end of injection

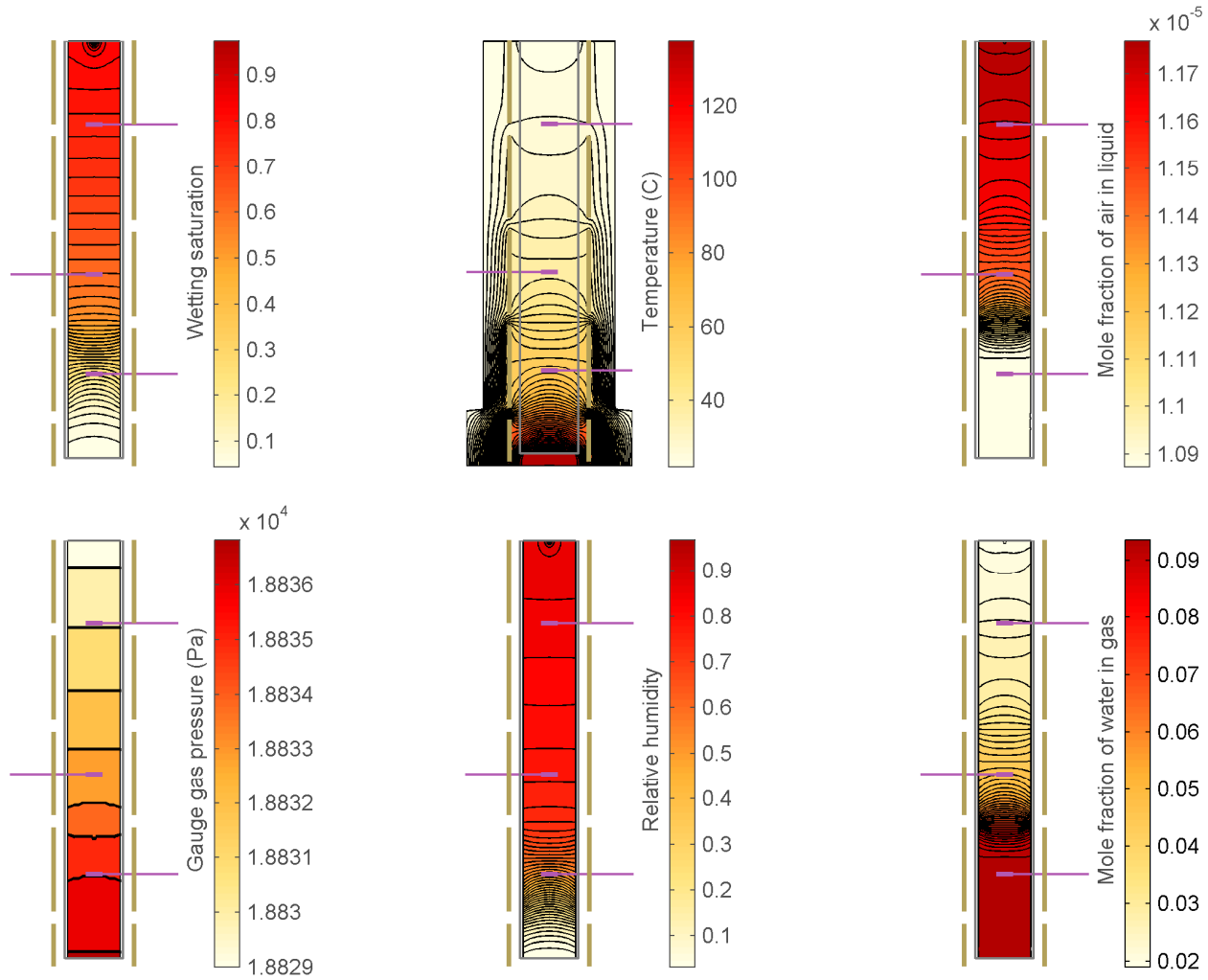


Figure 3-4. Simulation State at the End of the Injection Phase
 {1 Pa = 0.000145 psi; °F = [1.8 × T °C + 32]}

Cumulative change to end of heating

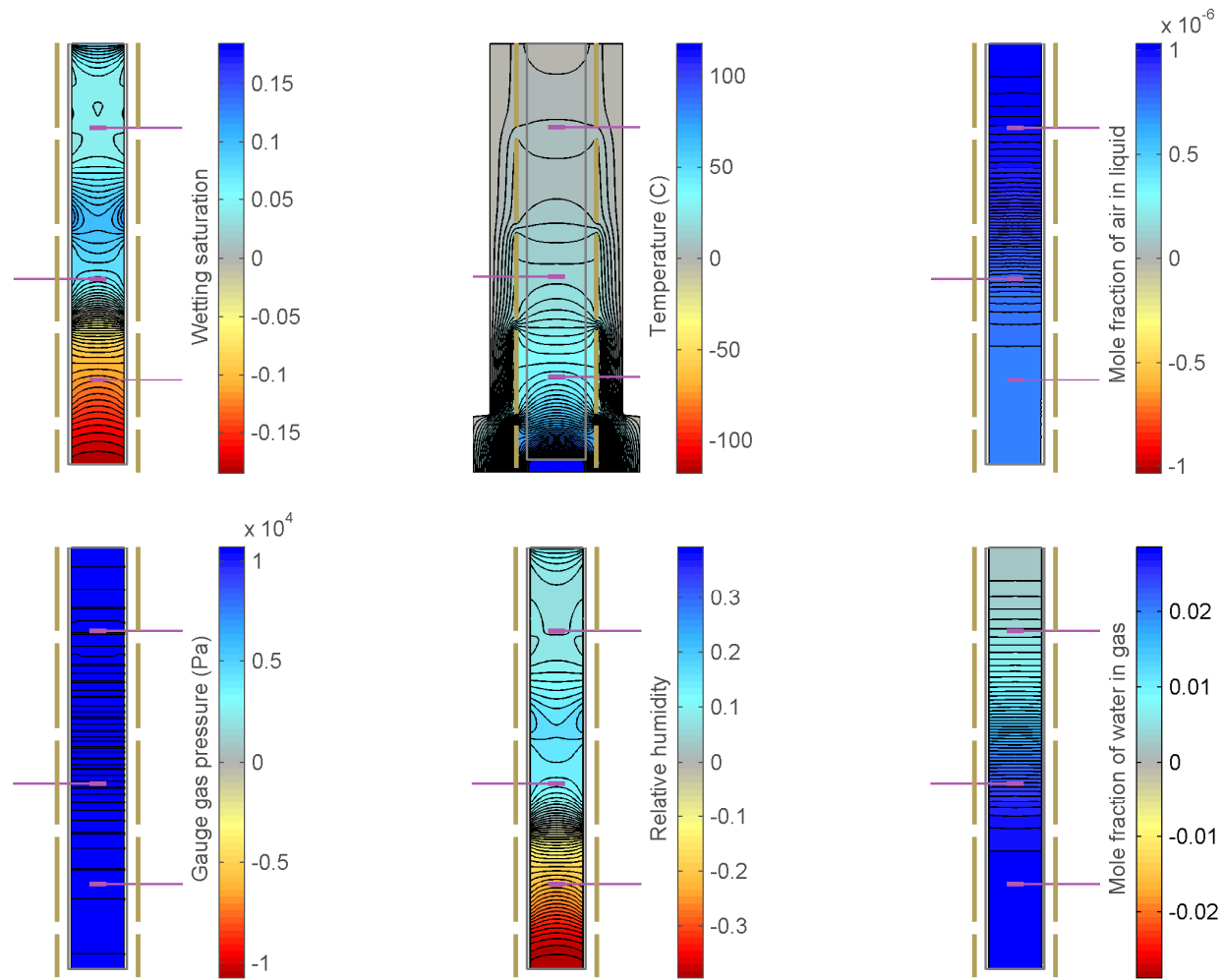


Figure 3-5. Change in State From the Start of Heating to the End of the Injection Phase
 {1 Pa = 0.000145 psi; $^{\circ}\text{F} = [1.8 \times \text{T } ^{\circ}\text{C} + 32]$ }

Cumulative change over injection

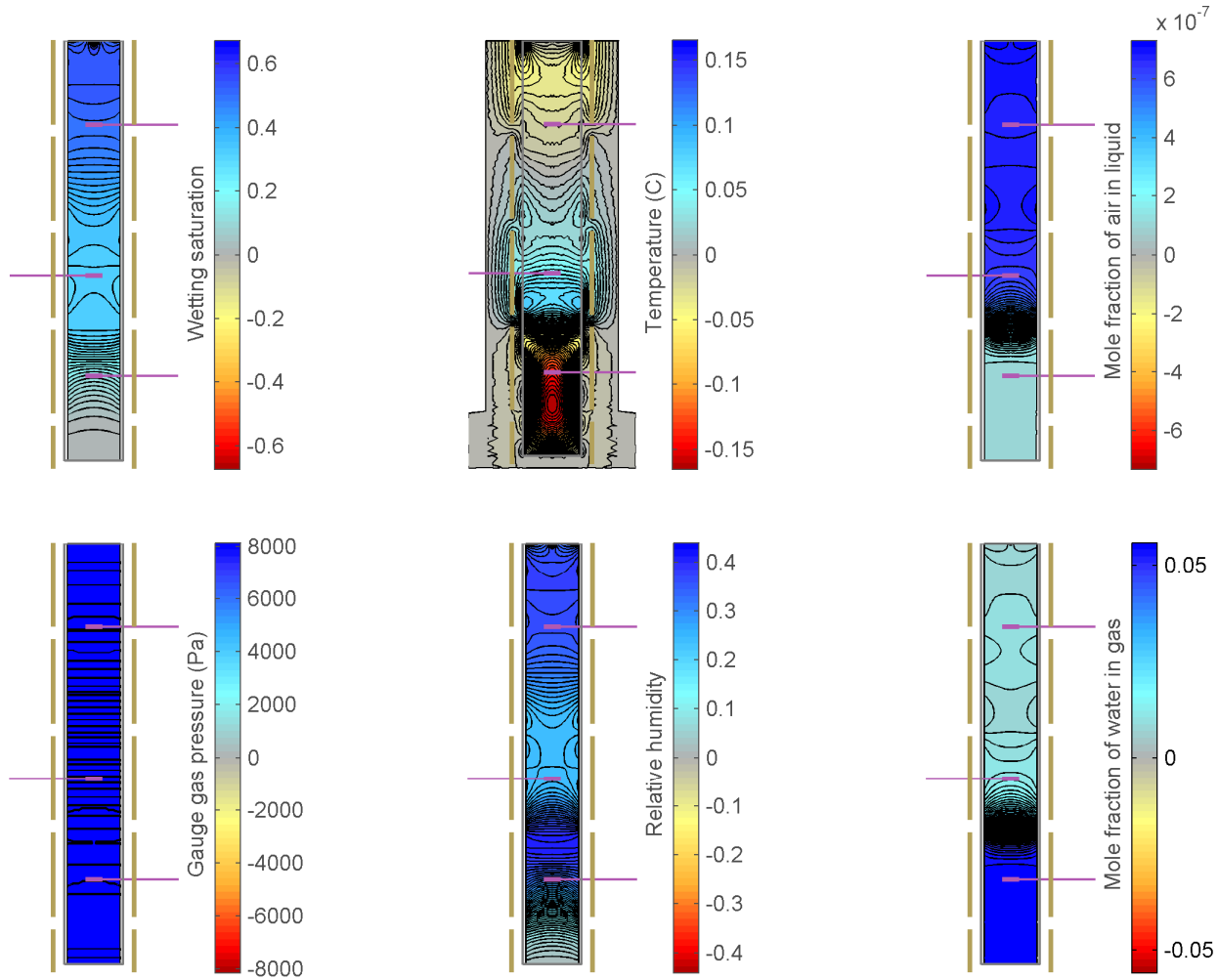


Figure 3-6. Change in State From the Start of Injection to the End of the Injection Phase
 {1 Pa = 0.000145 psi; °F = [1.8 × T °C + 32]}

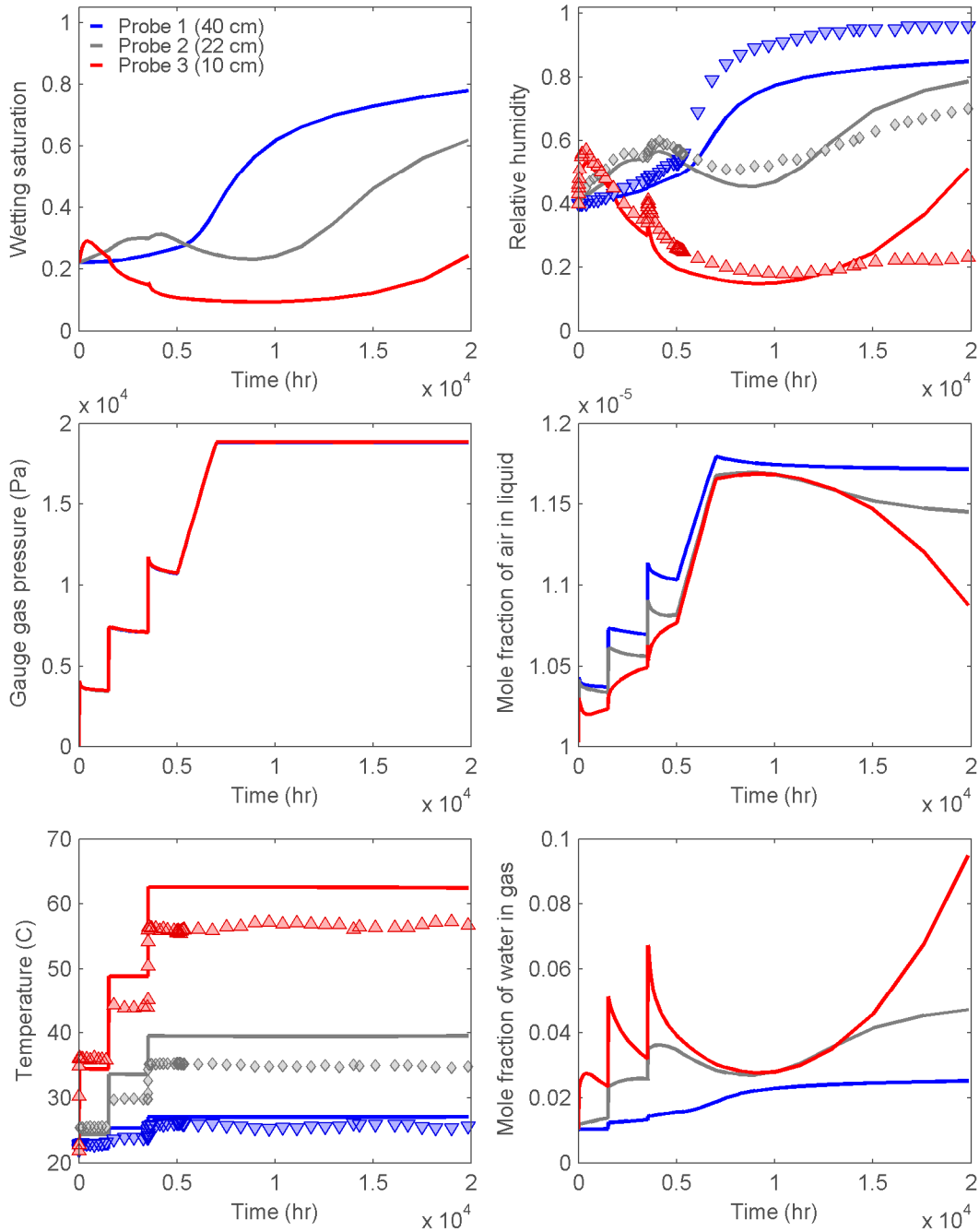


Figure 3-7. Time History of State Variables at Probe Locations Over the Thermal and Injection Phases. Symbols Indicate Laboratory Measurements and Lines Indicate Model Results {1 cm = 0.39 in; 1 Pa = 0.000145 psi; °F = (1.8 × T °C + 32)}

Figure 3-8 illustrates cumulative inflow as measured by the experiment and cumulative change in water mass as calculated by *xFlo* (the curve labeled “*xFlo*: $k \times 20$, no plate”). The two appear to be governed by very different processes, because they behave entirely differently over time. The actual inflow is characteristic of a diffusion-like process, because the rate of inflow scales with $t^{-1/2}$. The *xFlo*-calculated inflow is essentially constant over time, characteristic of an advection-dominated process (gravity drainage). Sensitivity studies suggested that the simulated inflow rate is dominated by gravity drainage even with much reduced saturated hydraulic conductivity.

These observations suggest that the *xFlo* implementation of a single-continuum van Genuchten constitutive model for retention in bentonite does not reflect the hydraulic behavior of the swelling pellets. The saturated hydraulic conductivity must be increased by a factor of 20 or more in order to achieve similar cumulative inflow over the experiment duration, but this results in drier conditions (smaller saturations) near the top of the column than inferred from the relative humidity measurements. Further, the factor of 20 is only appropriate for the actual duration of the test, and would be incorrect if the test were terminated at a different point in time.

A subsequently developed semianalytic approach to modeling the column test, discussed in Section 4.2.5, was used to further evaluate the retention model. The semianalytic approach calculated inflow rates similar to the measured rates without adjusting the parameters. The semianalytic approach provides a good comparison model to identify the source of the discrepancy. Results from a set of one-dimensional isothermal *xFlo* simulations were compared with the semianalytic approach using a consistent parameter set based on the column test parameters. The two approaches agreed very well, suggesting that *xFlo* is appropriately representing imbibition and the discrepancy between *xFlo* output and measured values is associated with the injection boundary condition.

Preliminary simulations using a single layer of grid cells to represent the porous plate over the bentonite exhibit inflows that are much closer to the observed values without artificially adjusting the saturated hydraulic conductivity. Figure 3-8 (curve labeled “*xFlo*: $k \times 1$, plate”) indicates that the mass intake is dominated by advection for the first 100 hr, then is dominated by a diffusion-like process for the remainder of the test. Total imbibition is approximately 80 percent of the measured value. The measured intake can be achieved by slightly increasing the intrinsic permeability, which would be inconsistent with measurements of saturated hydraulic conductivity, or by increasing the relative permeability at intermediate saturation levels using a different constitutive relationship. Figures 3-9 and 3-10 illustrate the final state at the end of the test and the state values at the probe locations, which correspond to Figures 3-4 and 3-7, respectively. The saturation profile during imbibition is much sharper with this change, and the lower two probes show less response than measured. Some of this discrepancy may be due to the overheated conditions in the model, and some may be due to constitutive relationships that are not quite appropriate at small to intermediate saturations.

Including the porous plate is necessary for matching the results, because it allows water from the nozzle to spread over the entire top surface of the bentonite, but no properties are available to describe the plate. For this modeling exercise, the plate was assumed to be coarser-textured than the bentonite. The intrinsic permeability was assumed to be approximately four orders of magnitude larger than the saturated intrinsic permeability for the bentonite and the bubbling pressure was assumed to be approximately an order of magnitude smaller. With these assumptions, the equilibrium state of the porous plate is almost completely desaturated at the initial conditions for the bentonite, thus almost all water in the porous plate would be rapidly drawn into the bentonite at the start of the experiment. A porous plate is typically saturated

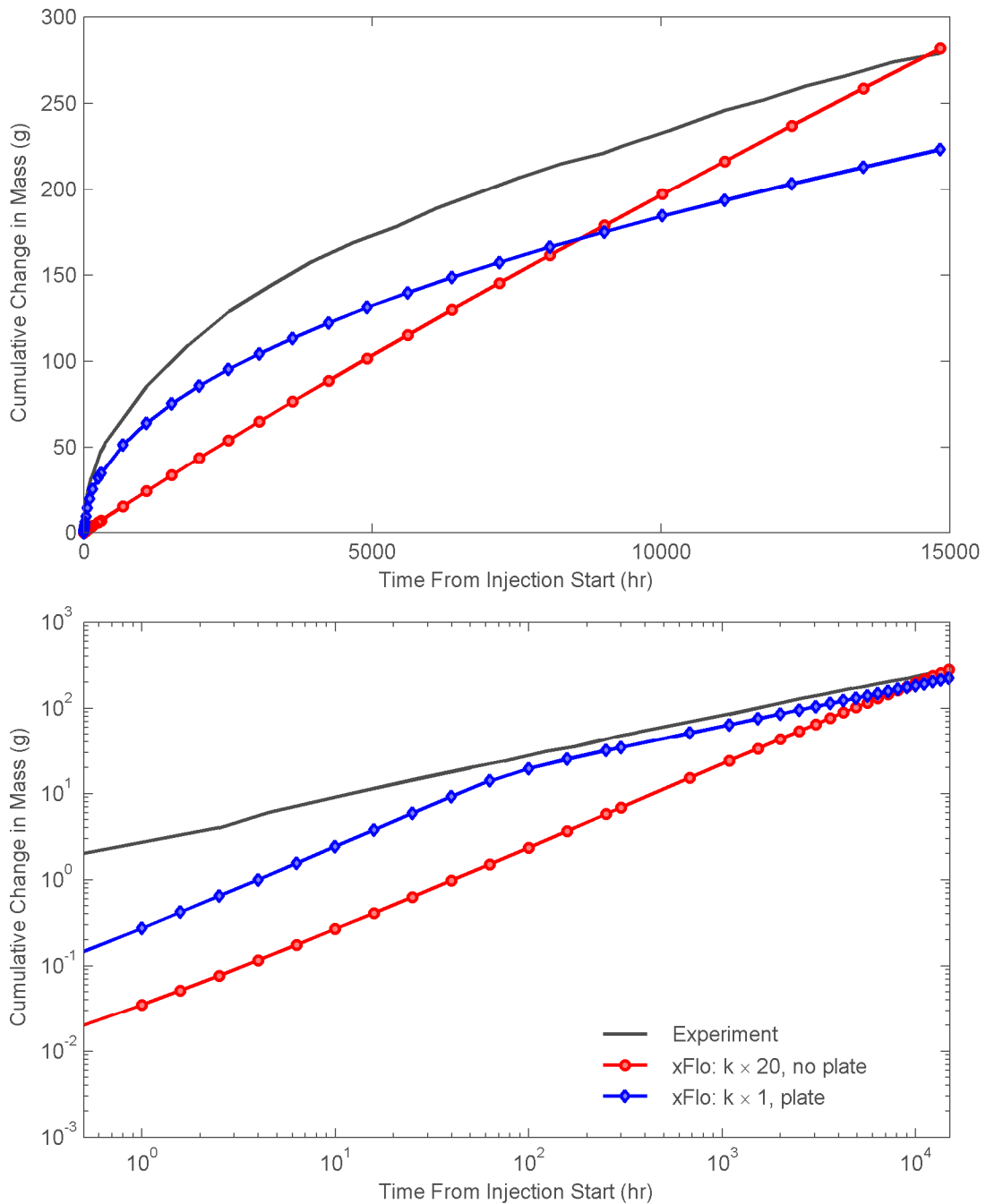


Figure 3-8. Time History of Cumulative Inflow Over the Injection Phase. Measured Cumulative Rate Is Proportional to $t^{1/2}$ and xFlo-Calculated Cumulative Rate Is Proportional to t Unless a Porous Plate is Included in the Model

State at end of injection

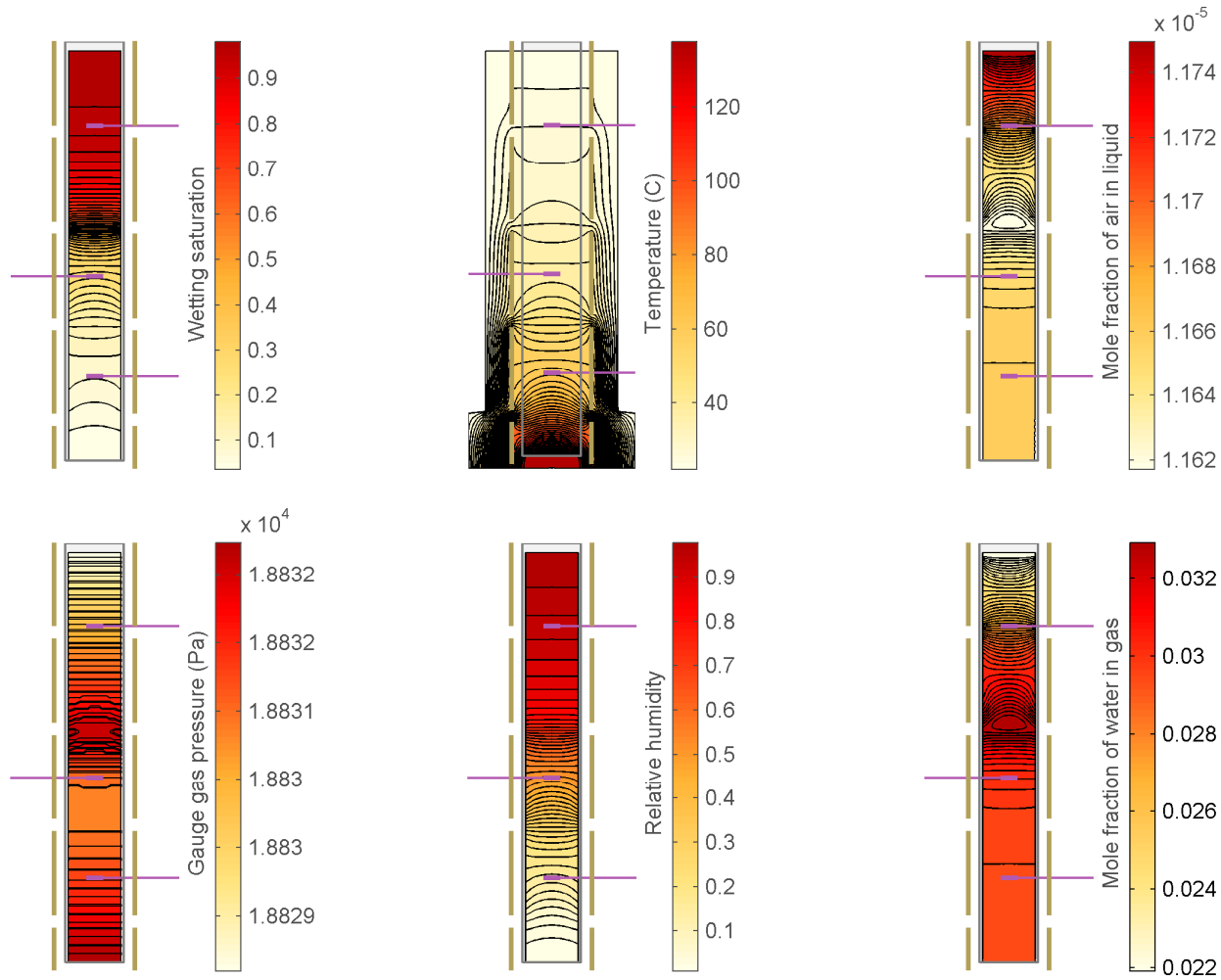


Figure 3-9. Simulation State at the End of the Injection Phase With a Porous Plate
 {1 Pa = 0.000145 psi; °F = [1.8 × T °C + 32]}

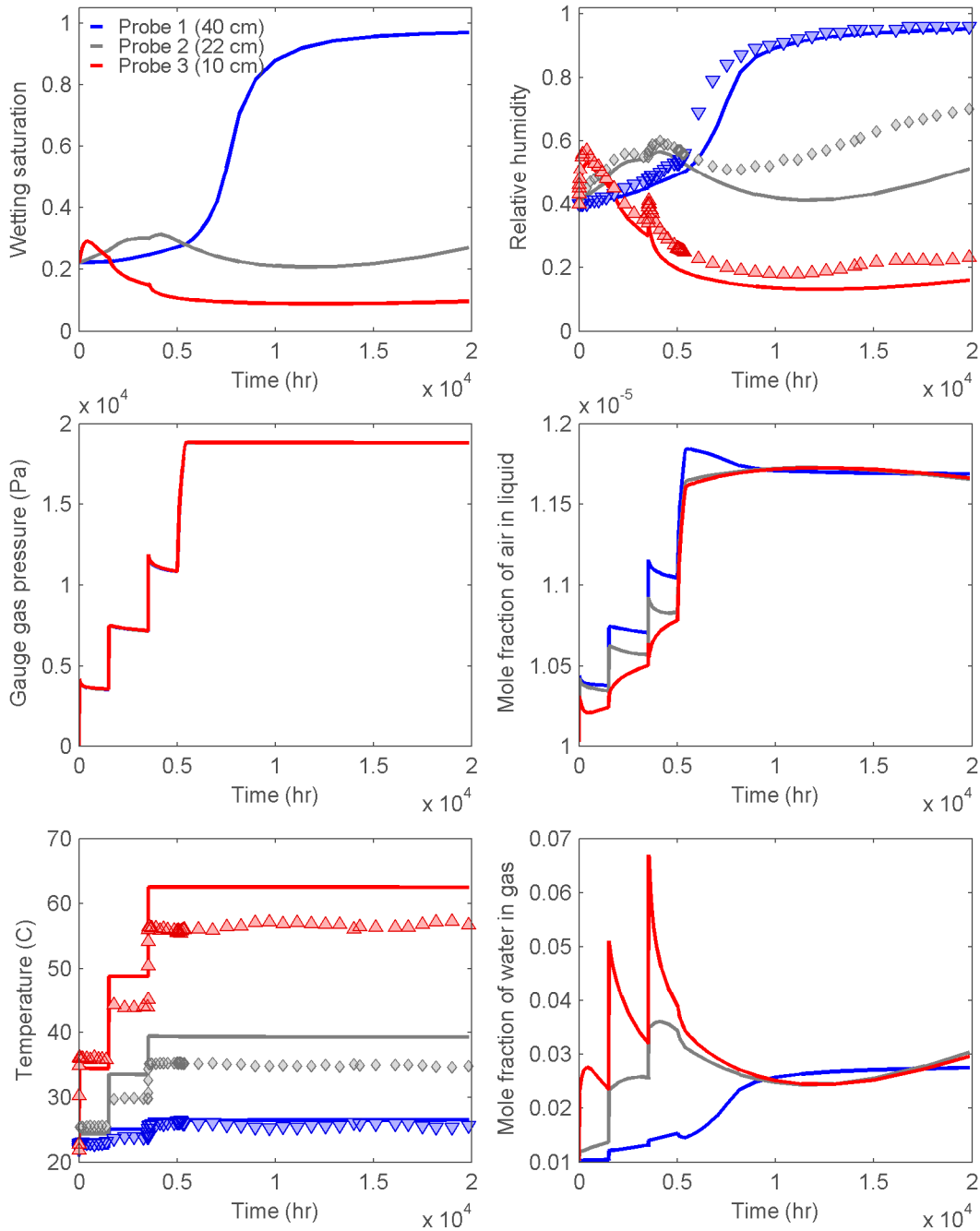


Figure 3-10. Time History of State Variables at Probe Locations Over the Thermal and Injection Phases With Porous Plate. Symbols Indicate Laboratory Measurements and Lines Indicate Model Results {1 cm = 0.39 in; 1 Pa = 0.000145 psi; °F = [1.8 × T °C + 32]}

before installation, but the initial water content of the plate cannot be determined from the available information. For the modeling exercise, the plate was assumed to be initially in hydraulic equilibrium with the bentonite to speed computations. This assumption has little effect on the moisture dynamics. Water draining from a saturated porous plate with porosity of 0.2 would have increased the total water content in the column by approximately 3.4 percent, sufficient to advance the wetting front during imbibition by approximately 1 mm [0.04 in].

The gas pressure response is consistent with gradual pressurization of entrapped air by invading water until reaching a threshold pressure. At this threshold, gas overcomes capillary effects and escapes out the injection cylinder. The duration of the pressurization phase depends on the pressure applied at the injection cylinder. We noticed that the computational time step becomes much smaller as the threshold is approached, but increases once the threshold is passed. The threshold pressure is likely to depend on the constitutive relationship for gas conductivity in near-saturated conditions.

3.2 Results from Geomechanical Modeling

The geomechanical model (Section 2.2) was used to calculate deformation (porosity change) and pressure histories within the bentonite column. The plot of vertical deformation shown in Figure 3-11 (labeled “Y-displacement” in the figure) shows the deformation pattern at the end of the test consists of extension in the top zones {elevation of approximately 0.15 m [0.49 ft] or greater} and compression near the base (elevation smaller than 0.15) of the bentonite column. The vertical deformation is downward everywhere and reaches a maximum at the elevation of approximately 0.15 m [0.49 ft]. This deformation pattern can be interpreted to indicate extension in the top zones and compression in the base zones. The pattern implies an increase in porosity in the top zones and decrease in the base zones. However, the porosity change appears small as discussed subsequently.

3.2.1 Change in Porosity

The porosity change is shown in Figures 3-12 and 3-13 in terms of the change in void ratio relative to the initial void ratio. Figure 3-12 shows the zones of void ratio increase, varying from an increase of approximately 0.005 near the elevation of 0.1 m [0.33 ft] to an increase of approximately 0.025 near the top of the column. Figure 3-13 shows a decrease in void ratio of up to 0.05 in the base zones, which is greater than the increase in the top zones. For an initial void ratio of 0.797 (initial porosity of 0.444), the calculated changes imply a final void ratio of 0.747–0.822 (porosity of 0.428–0.451). The hydrological significance of such a change will be evaluated as part of subsequent model calculations.

3.2.2 Axial Pressure

As Figure 3-14 shows, the measured axial pressure was essentially constant at 0.1–0.2 MPa [14.5–29 psi] for the first 5,000 hours (heating phase) of the test, increased rapidly to approximately 1 MPa [145 psi] during the first 500 hours of infiltration, and increased slowly toward approximately 1.4 MPa [203 psi] during the remainder of the infiltration phase. In contrast, the calculated axial pressure is negative during the first 3,500 hours of the heating phase and increased thereafter. During the infiltration phase, the calculated axial pressure increased at a different rate than measured. Our calculations indicate that the axial pressure was controlled by moisture redistribution throughout the test. The contribution of thermal expansion to the axial pressure appears negligible. The negative axial pressure early in the heating phase suggests that the model unit swelling coefficient needs to be increased so the

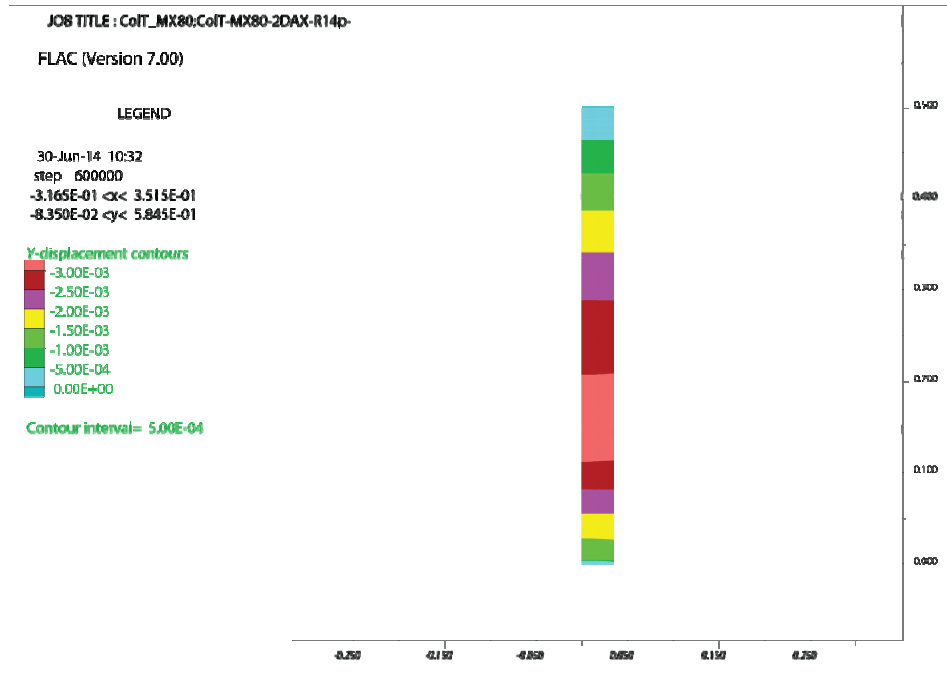


Figure 3-11. Contours of Calculated Vertical Deformation at the End of Testing (Time of 20,000 Hours)

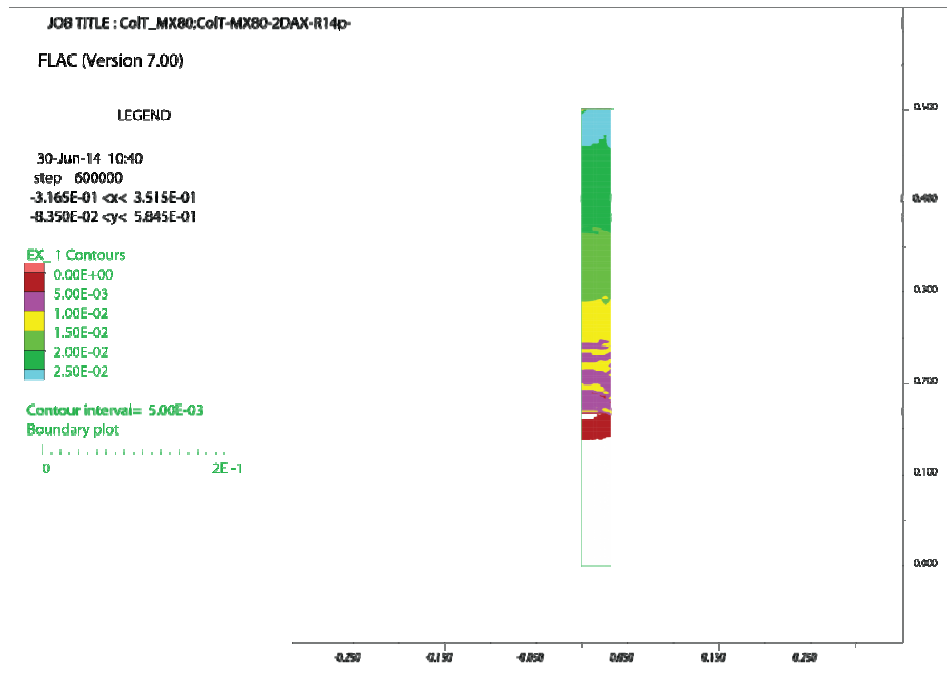


Figure 3-12. Contours of Void Ratio Change, Showing Areas of Void Ratio Increases Relative to the Initial Void Ratio

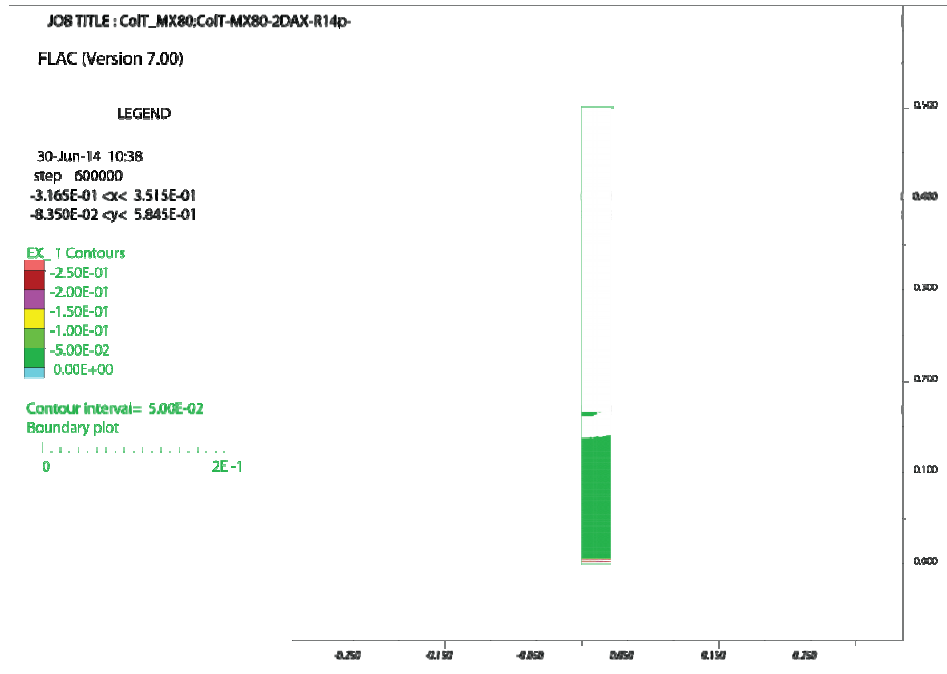


Figure 3-13. Contours of Void Ratio Change, Showing Areas of Void Ratio Decreases Relative to the Initial Void Ratio

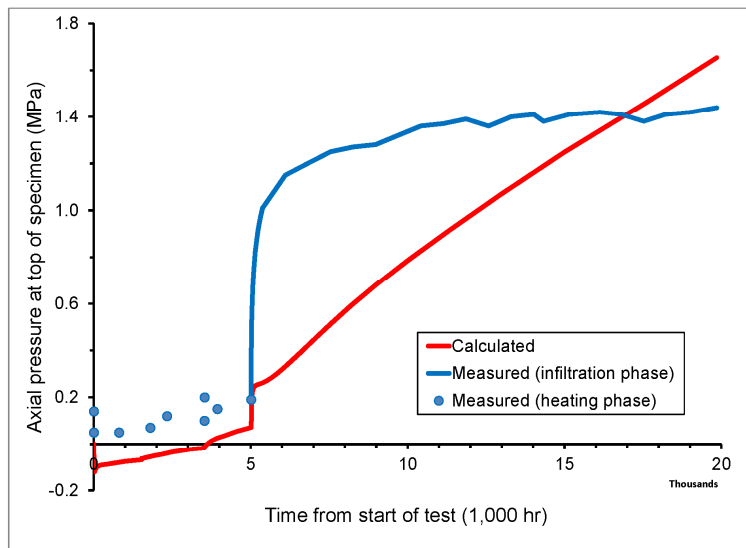


Figure 3-14. Calculated and Measured Axial Pressure Histories at the Top of the Bentonite Column, Showing Results for the Entire Test History

swelling pressure generated during this period will overcome a small decrease in pressure due to mechanical response to suction change (compression of bentonite specimen due to decrease in stress and stiffness caused by suction release) (cf., Ofoegbu, et al., 2013b, Figure 7). However, the calculated axial pressure history during the infiltration phase suggests that a change in the calculated water-intake rate is needed and it may be better to implement the change before modifying the swelling coefficient.

The calculated axial pressure is controlled by mechanical parameters bulk modulus (K) and unit swelling potential (α_{cW}), and the moisture content and its spatial gradient. The effects of moisture content and its spatial gradient can be discerned from Figure 3-15, which shows the calculated and measured axial pressure histories during the infiltration phase along with the calculated and measured cumulative water intake. As the figure suggests, the difference between the calculated and measured axial pressure for the infiltration phase is likely caused by the difference between the calculated and measured cumulative water intake. Therefore, further work on the TH modeling to better reflect the water intake as closely as possible is needed before attempting further adjustment of the mechanical parameters relevant to swelling pressure modeling.

3.3 Conclusions From the Column Study

Several observations and conclusions can be drawn from the progress on modeling the bentonite pellet column test.

- Vapor transport in hot and dry bentonite is relatively well characterized in the *xFlo* model, but may be somewhat underestimated in cooler conditions. The model better matches observations when temperature- and capillary pressure-dependent vapor pressure lowering is used, and when capillary pressure is adjusted to account for changes in surface tension.
- Under cooler conditions, connected liquid pathways in the pellets may provide a short circuit that enhances vapor transport under a thermal gradient. Further work would be necessary to characterize this process in granular bentonite. Enhanced vapor transport may be less important for overall moisture transport during rewetting.
- The thermal conductivity for bentonite is difficult to determine from the experimental measurements because of uncertainties related to heat loss and the dominant effect of highly conductive steel reinforcement bands in the laboratory setup. The COMSOL model, which more accurately represents thermal boundary conditions and apparatus geometry, suggests that the bentonite thermal conductivity is approximately 0.33 W/m/K prior to the injection phase. The *xFlo* model, which accounts for latent heat transport but does not consider radiation boundary conditions, suggests that the bentonite thermal conductivity may be less than the measured value of 0.12 W/m/K. The discrepancy between models should be addressed in future work.
- Thermal phase measurements could not be matched unless the gas relative permeability was increased by several orders of magnitude in the dry media. The Klinkenberg relationship does not address the root cause of this condition, but provides a convenient mechanism for scaling gas phase transport. Simply scaling intrinsic permeability allows too much water drainage, suggesting that constitutive relationships reflecting capillary processes should be examined more closely.

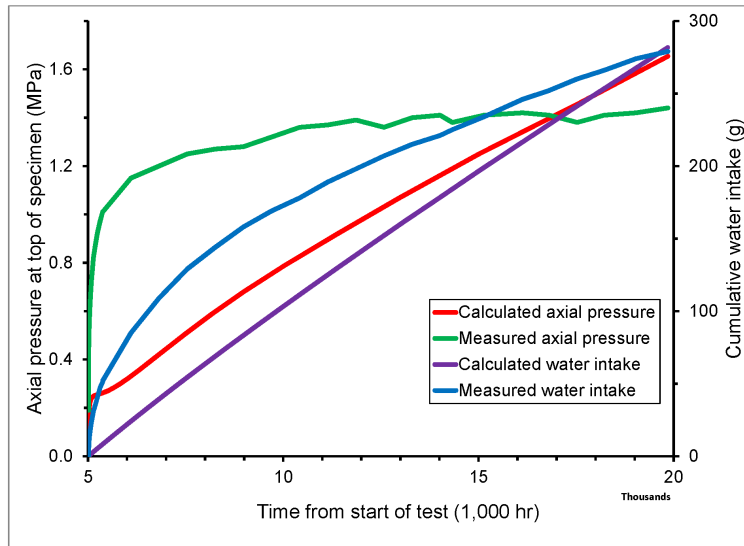


Figure 3-15. Calculated and Measured Axial Pressure Histories at the Top of the Bentonite Column, Showing Results for the Infiltration Test Phase

- Imbibition was not well represented in the *xFlo* model of the column test without including the porous plate at the top of the bentonite. Measured water imbibition was consistent with control by a diffusion-like process, but artificially increasing bentonite intrinsic permeability to match the total experimental inflow resulted in the *xFlo* model calculating control by gravity drainage. An isothermal one-dimensional (1-D) semianalytic model using the same hydraulic properties, discussed in Section 4.2.5, closely matches the measured injection rates, and the *xFlo* model closely matches the semianalytic model for a representative imbibition case. A substantial source of the discrepancy between measured and calculated imbibition rates without the porous plate stemmed from a poorly represented top injection boundary condition in the column test model.
- The model initially did not include the porous plate at the top of the bentonite because no information on its thickness or hydraulic properties was available. The laboratory experiment included the porous plate to help redistribute the flow radially, making flow into the bentonite more 1-D. At late time, diffusion must be essentially vertical from geometric constraints. The consistent trend in the injection slope implies that there was no transition from spherical diffusion to vertical diffusion or the transition occurred in the first few hours, consistent with essentially 1-D vertical imbibition from the start of injection. Preliminary simulations including a permeable porous plate suggest that omitting the plate strongly reduces imbibition into the bentonite by reducing the area exposed to wetting.
- The most pressing model development need is to better represent the unsaturated hydraulic conductivity behavior of swelling bentonite in *xFlo*. Addressing this model need is a priority for future work.

- The geomechanical model qualitatively represents the observed behavior (i.e., the changes in axial pressure). However, parameter adjustments may be necessary but will be dealt with better after the hydrological model change regarding unsaturated hydraulic conductivity.

4 PREPARATION FOR HE-E TEST MODELING

As stated earlier, modeling the field-scale HE-E test is the focus of the next task under Task B1 of DECOVALEX 2015. This test considers two bentonite buffer scenarios—granular bentonite and sand/bentonite mixture (a 65-percent sand/35-percent bentonite) (Gaus, et al., 2014). The HE-E test consists of two 4-m [13 ft] heaters within a 1.3-m [4.3 ft]-diameter tunnel bored in clay rock at the Mont Terri Rock Laboratory. The heaters will be located inside a 0.3-m [0.9 ft] diameter steel liner and will be isolated within the liner with Teflon plugs. The steel liner will rest on solid bentonite blocks, and the two heaters will be surrounded by different buffer media. The same buffer media were used for the column tests. Concrete plugs will be emplaced in the tunnel (outside the steel liner) at the heater ends and between the heaters.

There are three bentonite-based media included in the HE-E test, the two buffers and the solid blocks. The column test results suggest that the constitutive models implemented in *xFlo* can reasonably represent vapor-dominated transport in a medium consisting of granular bentonite pellets, at the cost of artificially increasing air permeability by several orders of magnitude. Given this observation, it is not clear that the constitutive models implemented in *xFlo* correctly represent liquid hydraulic conductivity and thermal conductivity. Accordingly, preparations for the HE-E test should include further examination of the constitutive relationships describing mass and energy transport in bentonite-based media to better understand how swelling processes might affect the constitutive models.

Section 4.1 provides a short description of current staff thinking regarding conceptual models for flow in bentonite-based media, which features pores at vastly different sizes. Section 4.2 presents and examines several current constitutive models that might be applied or extended to represent the different pore scales in an equivalent continuum framework. Constitutive models for clay are being actively developed by the international technical community, thus Section 4.2 necessarily represents a snapshot of a rapidly evolving field. One or more of these models could be used to augment *xFlo* capabilities. Section 4.3 considers several potential augmentations to *xFlo* that staff are currently considering to better represent thermohydrological (TH) processes in bentonite; some of these may be suitable to better represent the HE-E test. Section 4.4 describes procedures that staff are considering in order to better link *xFlo* and FLAC for the HE-E test.

4.1 Conceptual Model for Flow in Bentonite, Sand/Bentonite Mixtures, and Granular Bentonite Pellets

Bentonite exhibits (i) swelling properties as water is added; (ii) low permeability; and (iii) high cation exchange capacity, making bentonite an attractive component of a buffer for isolating waste packages in a geologic repository. Bentonite is typically considered for emplacement in three general categories: (i) solid blocks, (ii) mixed with sand, and (iii) granular pellets. Typical emplacement concepts rely on emplacing unsaturated bentonite as a buffer, which subsequently swells to eliminate residual fast pathways during rehydration.

Bentonite includes pore structures at several different scales, which strongly influences how bulk hydraulic properties such as capillary pressure, water permeability, and air permeability respond to changing moisture content because water preferentially enters the smallest available pores (Figure 4-1). Bentonite consists of a mixture of nonswelling mineral grains and expansive grains, with pore space around the grains. In the following, the expansive grains, formed of platy smectite minerals, are referred to as platelets. Intergrain surface forces tend to

- 1a: Mobile inter-aggregate water
- 1b: Immobile bulk water
- 2a: Mobile intra-aggregate water
- 2b: Immobile intra-aggregate water
- 3: Inter-layer water

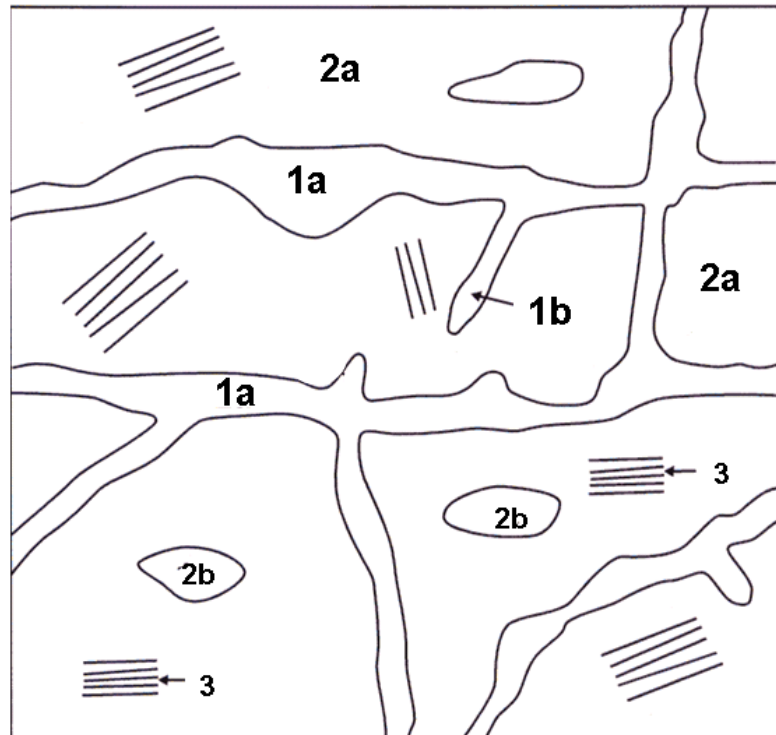


Figure 4-1. Conceptual Description of Bentonite Pore Structures

draw grains into larger structures, called aggregates, which have pore space between the aggregates. In bentonite/sand mixtures, pore space exists between the sand grains at a larger scale than pores within the bentonite aggregates. The space between the sand grains is partially or completely filled with bentonite aggregates. When bentonite pellets, which are formed from many aggregates, are used, pore space is present between the pellets at a larger scale than pores within the bentonite aggregates. As measured by techniques such as mercury intrusion porosity (MIP), the resulting pore size distribution is typically bimodal or trimodal because of these different scales (e.g., Romero, 2013). The typical pore size between clay grains tends to be on the order of 10 to 100 nm and increases by 1 to 2 orders of magnitude to aggregates and another 1 to 3 orders of magnitude to sand grains or pellets. Partially saturated hydraulic properties strongly depend on the characteristic radius of a pore space, thus the hydraulic properties strongly differ among the modes of the pore-size distribution. Further, the bulk hydraulic properties strongly depend on the fraction of the pore space for each mode and any changes in the distribution of the modes.

The pore-size distribution changes on compaction. Expansive clays also respond to degree of wetting, electrolyte concentration and composition, and electrolyte composition bound to the mineral layers in the platelets. Expansive clays are sensitive to wetting and electrolytes because of the layered and charged nature of the minerals. The charges are repulsive. The pressure exerted to hold the mineral layers together against their mutual repulsion, and therefore their separation, depends on the capillary and osmotic state of the surrounding liquid and on pressures transmitted by intergrain contact. The pore space between the layers increases and water moves into the interlayer space as the layers spread. This pore space is typically an order of magnitude or so smaller than the pore space around the clay grains, at too fine of a scale to be accessed with MIP techniques but accessible with X-ray diffraction

techniques (e.g., Holmboe, et al., 2012), but the layers can largely dissociate when clay is mixed with water in dilute solutions.

4.1.1 Swelling and Permeability in Continuous Bentonite

Bentonite gains its swelling property from the presence of platy smectite minerals, primarily montmorillonite, that swell when wetted. A smectite fragment or platelet consists of a stack of solid mineral layers that may be tens of layers thick, structured so that electrical charges are oriented parallel to the layering. Edge effects preferentially align platelets so that the mineral layers are parallel as the platelets are drawn together during deposition, resulting in extensive aligned platy crystalline structures growing as the platelets join together. Layers with the same charge repulse each other, thus water molecules and positively charged ions preferentially enter between the solid layers. Water existing in 1, 2, or 3 pseudo-layers within a pair of solid layers is called crystalline water and is strongly bound to the layer surfaces. A platelet substantially increases in thickness as water atoms are added; a montmorillonite layer is approximately 0.96 nm thick and each water layer is approximately 0.28 nm thick, so a platelet almost doubles in volume when three pseudo-layers are added. The water between mineral layers is referred to as inter-layer water, and this pore space is called inter-layer pore space. The inter-layer pore space is typically fully water saturated (no air enters the pore space). Some of the layers may dissociate with sufficient available water.

The layer thickness between two bounding mineral surfaces is related to the disjoining pressure, which is the pressure acting on the face of each of the bounding surfaces. The disjoining pressure is the sum of interactions associated with the surfaces, such as electrostatic forces and van der Waals forces, plus the pressure in the bulk fluid outside the clay particle. If the interactions between the surfaces are not exactly balanced by the bulk pressure, the residual pressure required for equilibrium is called the swelling pressure. Tuller and Or (2003) summarize experimentally determined layer spacing data for Na-montmorillonite from Warkentin, et al. (1957) and Low (1980), and provide theoretical relationships for disjoining pressure components. The data are well fit (Figure 4-2) using the Langmuir formula for the electrostatic component of the disjoining pressure in the form

$$\Pi_e = 2\epsilon \left(\frac{\pi kT}{zeh} \right)^2 \quad (4-1)$$

where Π_e is electrostatic disjoining pressure, ϵ is dielectric permittivity, k is the Boltzmann constant, T is absolute temperature, z is the signed ion valence, e is the elementary charge, and h is layer spacing (inter-layer thickness). The Langmuir formula suggests that h is 1 (~4 water layers) and 10 nm when Π_e is approximately 10 and 0.1 MPa, respectively, implying that the inter-layer pore space is half of the grain volume at 10 MPa with no other forces restraining inter-layer expansion. Tuller and Or (2003) present equations for other components of the disjoining pressure, but the values are much smaller than that due to the electrostatic forces for Na-montmorillonite.

Intra-aggregate pores (pores around clay grains) are reported on the order of 5 to 50 nm. Inter-aggregate pores are on the order of 100 to 10,000 nm. A single inter-aggregate pore is much more important for fluid transport than a single intra-aggregate pore, because the equivalent permeability of a tube is roughly proportional to the cube of the tube diameter and because the intra-aggregate pores tend to be dead-end pores because of the way that the platelets aggregate into platy layers. The size of the pore also influences the effective properties of the water in the pore, because the viscosity and density of the water change as a

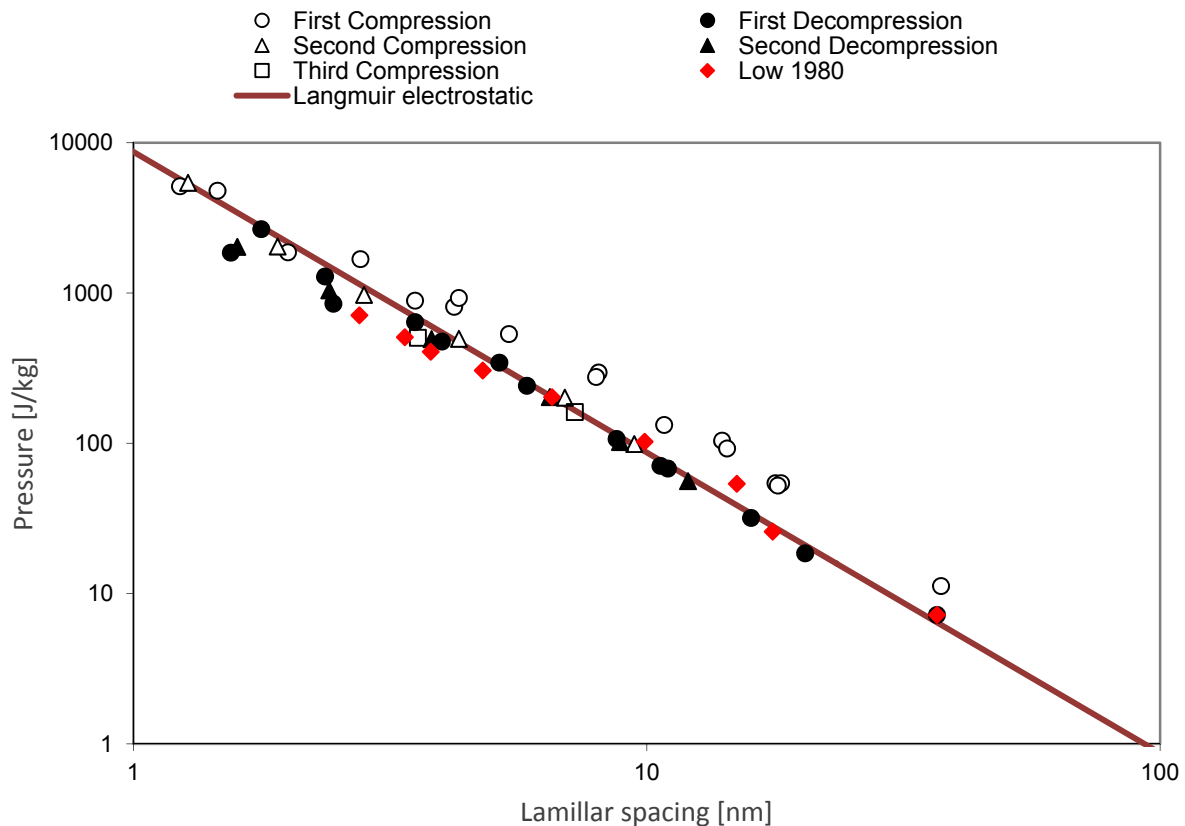


Figure 4-2. Electrostatic Component of Disjoining Pressure Compared to Compression Measurements by Warkentin, et al. (1957) and Low (1980)

result of forces acting immediately adjacent to a surface. Water immediately next to the surface is relatively immobile compared to the free water away from the surface. Assuming that four water layers are affected by surface forces, for example, suggests that approximately 1 nm of water is affected around the pore diameter, which can be a significant fraction of the water in intra-aggregate pores, thus the permeability of intra-aggregate pores is smaller than suggested by geometric factors alone. The area of an inter-aggregate pore is orders of magnitude larger than the affected thickness, thus surface forces in inter-aggregate pores are negligible except under very dry conditions.

The inter-layer and intra-aggregate pores can be considered as two interacting and overlapping continua with related but different swelling and hydraulic behavior. During hydration of an initially desiccated bentonite aggregate, surface forces dominate so that water molecules are drawn into the smaller inter-layer pore space and form a comparably thin layer on the outside surfaces of the platelet. Water entering an inter-layer pore creates new inter-layer pore space by separating the mineral layers, thereby thickening the clay platelet. If the bentonite consists only of platelets perfectly aligned by surface forces, the intra-aggregate pore space may also swell like an inter-layer pore space. If a bentonite aggregate consists of a mixture of randomly oriented platelet structures and nonswelling grains, when the platelets become thicker than some threshold value the surrounding intra-aggregate pores also become bigger on average as the swelling platelets push apart the nonswelling clay grains. Because the total mineral volume remains constant while the pore space increases, the total aggregate swells. The aggregate

also becomes more permeable as the intra-aggregate pores become larger. It can be inferred that the rate of creation of new intra-aggregate pore space with inter-layer swelling decreases with moisture content to some extent, however, because (i) fragments may rotate into newly created pore space and (ii) adding water layers between the mineral layers in a stack may allow the mineral layers to slide like a deck of cards.

Available pore-size distributions, determined from MIP and other methods, suggest that the primary modes of the pore-size distributions scale during changes in moisture content (Nowamooz and Masroui (2010), Dieudonné, et al. (2013)). In other words, the modes primarily translate up and down on a log scale without much changing the spread about the mode. By implication, a van Genuchten retention relationship (van Genuchten, 1980) for the intra-aggregate medium would have a similar pore-size index parameter regardless of moisture content (i.e., the van Genuchten m and n parameters). The air-entry pressure scales inversely with pore effective radius, thus scales inversely with the cube root of intra-aggregate porosity.

Swelling of the bentonite aggregates has a different consequence for overall permeability depending on whether the volume of continuous bentonite medium is fixed or allowed to swell. When the volume of the continuous medium is fixed, the increase in inter-layer and intra-aggregate pore space must be exactly balanced by a decrease in inter-aggregate pore space. This is akin to inflating a group of balloons in a box, using the air between the balloons to blow up the balloons. Inter-aggregate pore space is squashed by deforming aggregates, dramatically reducing its permeability.

When a small bentonite sample is allowed to swell in all directions during hydration, that is, unconfined, the swelling aggregates are forced apart. Conceptually this is like inflating a group of balloons without constraining them. The net effect likely depends on the aggregate stiffness, which can be inferred to decrease with increasing saturation. A stiff (dry) aggregate would increase the inter-aggregate pore size and increase permeability in the same way that thickening stacks create new intra-aggregate pore space. A highly deforming (wet) aggregate will tend to preferentially squeeze the inter-aggregate pore space before bulk swelling occurs. Accordingly, it is likely that both the air entry pressure and the pore-size index depend on degree of swelling.

When the sample is only unconstrained in one direction, it is reasonable to expect that existing inter-aggregate pores are lengthened in the unconstrained direction while the swelling aggregates reduce the pore diameters in the perpendicular plane, reducing permeability in the unconstrained direction. It is not immediately obvious whether permeability in the plane perpendicular to the unconstrained direction will tend to increase or decrease in this process. In large samples, gravity will make the upper portion of the sample behave like a small sample and will make the lowest portion behave more like a constrained sample. Confinement pressure increases linearly with overburden thickness, giving an exponential transition rate between the unconfined and confined behavior.

4.1.2 Sand/Bentonite Mixtures

Sand may be added to bentonite to control swelling pressure, increase thermal conductivity, provide greater mechanical resistance, and reduce costs. In addition, these mixtures exhibit a relatively high permeability to gas in the unsaturated state and a comparably low gas entry/break-through pressure in the saturated state relative to the host rock. These properties are useful in dissipating gas formed due to waste package corrosion, while maintaining its ability to act as a barrier to flow for radionuclide transport (De Bock, et al., 2009). A sand/bentonite

mixture introduces a larger pore scale, corresponding to the space between the sand grains. At low ratios of bentonite to sand, the sand forms a structural skeleton and bentonite aggregates occupy part of the pore space between sand grains, leaving residual pores potentially larger than the inter-aggregate pores. At high bentonite/sand ratios, the bentonite forms the structural skeleton and the sand grains are separated from one another or form clumps without necessarily forming a connected pore space. Komine (2010) discusses hydraulic conductivity of sand/bentonite mixtures with respect to swelling deformation using experiments with bentonite contents of 10, 20, 30, and 50 percent (it is not clear whether the percentage is by volume or mass) in two different packing density categories. The bentonite is 48 percent montmorillonite. The measured hydraulic conductivity in 1-cm [0.4 in] thick samples allowed to swell vertically increases monotonically with swelling strain for the 10 and 50 percent bentonite content samples, but exhibits a dip for intermediate swelling strains (less than approximately 15 percent) for the 20 and 30 percent samples. Hydraulic conductivity increases by 5 to 6 orders of magnitude for a swelling strain of 1 percent for the 10 percent sample, but increases by less than an order of magnitude for a swelling strain of 80 percent for the 50 percent sample. Intermediate mixture ratios respond even less than the 50 percent sample.

4.1.3 Bentonite Pellets

Bentonite pellets also introduce a larger pore scale, corresponding to individual bentonite pellets. For the purposes of this discussion, a bentonite pellet is the smallest discrete unit of bentonite that might be used for emplacement. A pellet is a manufactured piece of dried and compressed bentonite, and includes numerous aggregates. Depending on the manufacturing process, pellets can range from submillimeter to centimeter scales. Bentonite pellets are analogous to aggregates, relatively hard when dry and increasingly deformable as they wet. Transport behavior in a bentonite-pellet buffer is hysteretic, because the macropore space between pellets heals as the pellets swell and deform upon saturation, and the original pellets are not recovered during subsequent desaturation.

4.1.4 Gas Flow in Bentonite

Bentonite is an extremely fine-grained material, with relatively few fluid molecules within individual pores. Gas transport is anomalously large in fine-grained media, because individual gas molecules can slip along surfaces (unlike liquid molecules). Gas transport in fine media is typically described using the Klinkenberg (1941) approach, which adjusts gas permeability based on gas pressure.

The Klinkenberg correction may be significant within bentonite aggregates (i.e., the inter- and intra-aggregate pores). The permeability of saturated bentonite for the bentonite column test is roughly 10^{-20} m^2 , implying that gas permeability would be increased by roughly a factor of 50 to 200 at atmospheric pressure using two correlations collected by Tanikawa and Shimamoto (2009). The correction decreases to a factor of two for intrinsic permeability somewhere near 10^{-16} m^2 , and is negligible for more permeable media. There is roughly an order of magnitude range in measured correction factors for a given permeability. It is not clear whether the correlations were developed for dry media; if so, the correlations should also account for the reduced pore size available for flow under partially saturated conditions. Bentonite intra-aggregate pores shrink as the medium dries, decreasing intrinsic permeability, but the air-available fraction increases.

The Klinkenberg correction may be relatively unimportant in dry macropores of sand/bentonite mixtures with small bentonite content and dry macropores between bentonite pellets, because gas permeability should be much larger than 10^{-16} m^2 in these scenarios.

4.1.5 Liquid Flow in Bentonite

Liquid transport in bentonite is anomalously small relative to coarser media, because a significant fraction of the liquid is in the first few molecular layers and surface forces strongly attract these layers. These surface forces disproportionately restrict liquid flow under small applied gradients, in essence lowering the hydraulic gradient. Liu and Birkholzer (2012) discuss this phenomenon, indicating that the nonlinear behavior manifests as a threshold hydraulic gradient in the form

$$q = K[i - f(i, I, \alpha)]I \quad (4-2a)$$

derived by integrating the relationships

$$\frac{dq}{di} = K[1 - \exp(-(i/I^*)^\alpha)] \quad (4-2b)$$

$$I = \frac{I^*}{\alpha \gamma(1/\alpha)} \quad (4-2c)$$

where q is flux, i is the hydraulic gradient, K is hydraulic conductivity for large i , I is the threshold hydraulic gradient, I^* is a scaling parameter related to I and α , γ is the Gamma function, and $f(i, I, \alpha)$ is a function of hydraulic conductivity that approaches zero at large I . The scaling parameter α determines the degree of deviation from linearity. Swartzendruber (1961) considered $\alpha = 1$; $\alpha = 0$ implies that $f(i, I, \alpha) = 0$. Liu and Birkholzer (2012) suggest that $\alpha = 5$ is consistent with data for a sand/bentonite mixture presented by Cui, et al. (2008).

Liu and Birkholzer (2012) collected data over a range of intrinsic permeabilities from 10^{-20} to 10^{-14} m^2 that suggest I is approximately inversely proportional to intrinsic permeability raised to an exponent. The permeability of saturated bentonite for the bentonite column test is about 10^{-20} m^2 , implying a threshold gradient of roughly 10^4 . Liu and Birkholzer (2012) suggest scaling intrinsic permeability by relative permeability under unsaturated conditions, and Liu and Birkholzer (2013) further suggest accounting for temperature effects using viscosity. In summary, Liu and Birkholzer (2013) suggest that the appropriate scaling relationship should be

$$I = A \left(\frac{kk_r \mu_{ref}}{\mu} \right)^b \quad (4-2d)$$

where $A = 4.0 \times 10^{-12} \text{ m}^{-2b}$ and $b = -0.78$. The same effect is obtained using unsaturated hydraulic conductivity while adjusting A to account for the change in units. A convenient nondimensional form is

$$I = A^* \left(\frac{kk_r \mu_{ref}}{\mu k_{ref}} \right)^b \quad (4-2e)$$

where $A^* = 2.0047$ and $k_{ref} = 10^{-15} \text{ m}^2$.

For the column test, the initial suction pressure is approximately 10^8 Pa [$1.5 \times 10^4 \text{ psi}$]. A representative gradient for the column test might be calculated by applying 10^8 Pa

[1.5×10^4 psi] pressure difference over 0.1 m [0.33 ft] to yield 10^9 Pa/m. A unit hydraulic gradient is approximately 10^4 Pa/m, implying that the average gradient over the wetted zone in the column test exceeded the threshold gradient by a factor of 10 or more and accordingly surface effects would not be expected to be important. The relative permeability outside the wetted zone is orders of magnitude smaller than 1, however if it were appropriate to scale I using relative permeability, the threshold gradient would increase by orders of magnitude in the dry zone and may tend to sharpen the wetting front.

4.2 Constitutive Models for TH Processes in Bentonite Media

The *xFlo* and FLAC models currently have a somewhat different representation of TH processes. The *xFlo* model represents flow processes using the concepts of porosity on a fixed (Eulerian) grid. Extending *xFlo* to multimodal media requires partitioning the pore space into different continua, at least conceptually, to properly capture the hydraulic behavior. FLAC performs quasi-steady analyses, using the concept of void ratio to partition space, but uses a moving (Lagrangian) grid. The grid cells follow the deformation of the solid fraction of the medium.

Porosity and void ratio are related concepts. Porosity, θ , is defined as the volume of void space divided by the total volume, ranging from 0 to 1. Void ratio, e , is defined as the volume of void space divided by the volume of solids, ranging from 0 to ∞ . The two are related by

$$e = \frac{\theta}{1 - \theta} \quad (4-3)$$

In FLAC calculations, the change in e within a grid cell is due to a change in the grid size (i.e., the boundaries expand or contract) and all volume change in a cell is assigned to the void volume. The total solid volume remains essentially constant in a fixed domain, aside from swelling or shrinking due to thermal changes, thus the total void volume and the integral of porosity over the domain also remain essentially constant. However, the integral of e over a fixed domain may change as the medium deforms within the fixed boundaries, even when the total solid and void volumes remain constant. Some constitutive relationships are defined in terms of e . For properties defined with such relationships, local changes in e across the domain during deformation may result in changes to the average of the properties across the domain even when the total volume is unchanged.

If the FLAC domain is represented in *xFlo* using a fixed grid, deformation in the FLAC grid means that solid matrix passes across *xFlo* cell boundaries as the FLAC grid deforms. In some of the column test simulations, displacements of 3 mm occurred, corresponding to replacing more than half of the solid mass in a 5-mm *xFlo* grid cell. Changes in solid mass within a cell would need to be accounted for to accurately represent the pore space. The correction may be more important in a radial problem, such as around a heater. Further, Darcy's Law is defined in relation to the solid medium, thus the fluid velocity across a cell boundary should also include a correction factor accounting for the velocity of the solid matrix. This correction is only important when swelling or shrinking is actively occurring, and probably was negligible in the column test because deformations were constrained by the column walls.

The *xFlo* computational structure allows the FLAC domain to be represented in *xFlo* (with some modifications to *xFlo* input) by simply adjusting the cell volumes and link descriptions. This has the advantage of preserving direct links between the two models and allowing Darcy's Law to be used without correction. Translating FLAC grids to *xFlo* is particularly desirable in

two-dimensional (2-D) and three-dimensional (3-D) domains, because of the significant grid distortion that might occur.

FLAC considers the total void space without partitioning the void space into different continua, treating the entire mixture as an equivalent continuum. Due to the fine granularity of the buffer materials, an equivalent continuum approach is also warranted for TH processes. However, to represent the TH consequences of the swelling behavior, it is useful to partition the total void space into different continua to consider processes at different pore scales, then aggregate the different scales into an equivalent continuum. *xFlo* will need to consider relationships for water retention, intrinsic permeability, liquid and gas relative permeability, vapor diffusion, and thermal capacity and conductivity that acceptably change with void ratio and water content. These relationships will require that *xFlo* allocates appropriate computer memory for the parameters in each continuum. Some parameters can be tabulated by the type of medium; other parameters depend on the swelling state, thus must be calculated on the fly during iterations.

Mixture theory provides a means for aggregating continuum processes at different scales into an equivalent continuum. In this approach, continuity, mass, momentum, and energy balance equations are defined for each phase and continuum, along with linking constitutive relationships. The balance equations for each of the different continua and phases are added together, weighted by the volume or mass fraction of the continuum. Components of the balance equations corresponding to storage terms are usually combined in a straightforward way, but components corresponding to transport terms may be more complex due to interactions between different continua.

4.2.1 Multicontinuum Retention

In a conference presentation, Dieudonné, et al. (2014) extended the classic van Genuchten water retention curve to consider bimodal media (micro- and macropores). Micro- and macropores appear to correspond to intra- and inter-aggregate pores. This general approach may provide a useful framework for a larger range of pore scales. Rewritten for multiple continua, the relationship can be expressed in terms of mixture theory by

$$e_w(P_c) = \sum_i e_i \theta_{wi}(P_c) = \sum_i e_i \left[1 + \left(\frac{P_c}{P_{0i}} \right)^{n_i} \right]^{-m_i} \quad (4-4)$$

where e_w is total water ratio (defined as volume of water per unit volume of solid), e is void ratio, θ_w is water saturation, P_c is capillary pressure, P_o is a reference capillary pressure, n and m are van Genuchten exponents, and subscript i indexes a particular continuum. Dieudonné, et al. (2014) link the parameters for each medium to its respective pore-size distribution (PSD): (i) the maximum value of the PSD links to P_o , (ii) the width of the PSD links to n , and (iii) the shape of the PSD links to m .

Dieudonné, et al. (2014) tacitly neglect inter-layer pore space in this representation, presumably because the measurement techniques for determining the PSD cannot reach such small scales. The inter-layer pore space may be comparable to the intra-aggregate pore space for pure montmorillonite when several water layers exist in each layer, but is small when the montmorillonite minerals are a small fraction of the total solid mass. Inter-layer retention is considered in the chemical swelling model proposed by Xie and coworkers (e.g., Xie, et al., 2006, 2007).

Dieudonné, et al. (2013) considered experimental data from seven different media, including MX-80 bentonite and sand/bentonite mixtures, to fit a bimodal distribution of pore sizes with various structural changes. Dieudonné, et al. (2014) suggest that the e_i and P_{0i} values tend to vary with water content but the other parameters are almost constant. The n and m van Genuchten exponents are not related with the usual assumptions of $m = 1 - 1/n$ for the data sets.

Dieudonné, et al. (2014) describe the evolution of P_{0i} with void ratio using exponential relationships

$$P_{0m}(e_m) = P_{1m} \exp(-\alpha_m e_m) \quad (4-5)$$

$$P_{0M}(e_M) = P_{1M} \exp\left(-\alpha_M \frac{e - e_m}{e}\right) \quad (4-6)$$

where the m and M subscripts represent the micro- and macrostructures. Dieudonné, et al. (2014) give parameter values for Boom clay and London clay, which have much smaller specific surface than MX-80 and FEBEX bentonite.

Dieudonné, et al. (2014) relate microstructural void ratio to water ratio using

$$e_m = e_{m0} + \beta_1 e_w + \beta_0 e_w^2 \quad (4-7)$$

where e_{m0} is the microstructural void of the dry material and β_0 and β_1 quantify the swelling tendency of the aggregates. This is described as a generalization of linear ramp relationships proposed by Romero (2013) in the form

$$e_m = e_m^* + \beta \max(0, e_w - e_m^*) \quad (4-8)$$

where e_m^* is the water ratio enough to saturate the aggregate while leaving the interaggregate pores empty ($S_{rm} = 1$). Both relationships require iteration with Eq. (4-4) to determine a compatible pair of e_m and e_w for a given value of P_c .

The presented data suggest that it may be appropriate to allow the projection where $e_w < e_m^*$. For compacted bentonites, Romero (2013) uses several data sources to develop e_m^* and β values of 0.56 and 0.43, respectively. Romero (2013) shows that there is a strong relationship between the log of specific surface area and the two linear parameters in the form

$$e_m^* = \left[0.01 + 0.088 \ln\left(\frac{S_s}{S_{sr}}\right)\right] \pm 0.03 \quad (4-9)$$

$$\beta = \left[0.08 + 0.065 \ln\left(\frac{S_s}{S_{sr}}\right)\right] \pm 0.03 \quad (4-10)$$

where S_s is total specific surface area (m^2/g) and S_{sr} is a reference value ($1 m^2/g$). For both microstructural parameters, MX-80 and FEBEX bentonite fall on the low end of the parameter range given the specific surface area. Specific surface area accounts for both texture and compaction.

Romero (2013) collects several other relationships from the literature linking e_m , e , and saturation for different media. The relationships include power laws, exponentials, and ramps.

Tuller and Or (2003) discuss models for retention and permeability in clay, including relationships between layer spacing and chemical potential in the solution. The dominant behavior for two presented data sets and corresponding theoretical relationships are consistent with chemical potential proportional to $1/h^2$, where h is the layer spacing, when $h > 1$ nm. Spacings of 1 and 100 nm corresponds to capillary pressures of 10 MPa and 1 kPa, respectively. If change in intra-aggregate pore space is proportional to change in inter-layer pore space, the combination of swelling stress and microstructural void ratio may provide a relationship to determine an inter-layer retention relationship.

Figure 4-3 illustrates bulk retention relationships using the Dieudonné, et al. (2014) approach with parameters following Dieudonné, et al. (2014) and Romero (2013). The van Genuchten retention parameters are slightly modified to follow the restriction for relative permeability described in Section 4.2.2. As a first attempt to consider a third pore scale, the inter-layer pores are assumed to follow Eq. (4-1), with the macropore porosity reduced accordingly. The data are digitized from figures presented by Romero, et al. (2011). The FEBEX data are from a constrained system with e set to 0.74. The Barcelona clayey silt data are from a constrained system with e set to 0.37, 0.47, and 0.67. The Boom Clay data are from constrained systems with e set to 0.65 and 0.93. There is clear hysteresis between the wetting and drying curves, and several model parameters required small adjustments. In each of the panels, all parameters except for e are held fixed.

It became clear from fitting the retention curves in Figure 4-3 that there are a number of degrees of freedom available to match particular data sets, even with some constraints available from the literature. Further constraints will be useful in guiding parameter selections. These constraints may stem from studies explicitly measuring pore-size distributions in conjunction with other properties depending on pore-size distributions, such as hydraulic and thermal conductivities.

The multicontinuum formulation should be extensible to consider macropores arising from bentonite pellets or sand/bentonite mixtures. In this case, it is necessary to differentiate between the inter-aggregate and macropore continua in the same way that the micro- and macro-continua are treated above. This requires a second set of relationships. Parameters for this second set of relationships would need to be developed. It is probably appropriate to lump the inter-aggregate and macropore continua when considering the intra-aggregate scale, so it should not be necessary to greatly modify the microscale relationships developed above.

Under modest volume changes, such as would be expected for buffers, bentonite swelling may be largely reversible at the aggregate scale in solid blocks and in sand/bentonite mixtures (especially when the bentonite fraction is either large or small relative to the natural porosity of the sand). Even if the grains do not return to the same configuration, repeated drying and wetting cycles may yield a statistically similar arrangement of grains due to intergranular surface forces. For reversible media, wetting and drying behavior can be described with the same set of relationships.

Irreversible changes occur when bentonite pellets and granules are used, however, because the pellets “heal” on wetting to create a homogeneous mass. The macropore volume around the emplaced pellets is lost on healing. On drying, the macropore pore space is transferred to the inter-aggregate pore volume. A reasonable approach to irreversible swelling might simply allow the macropore volume to decrease on wetting but not increase on drying.

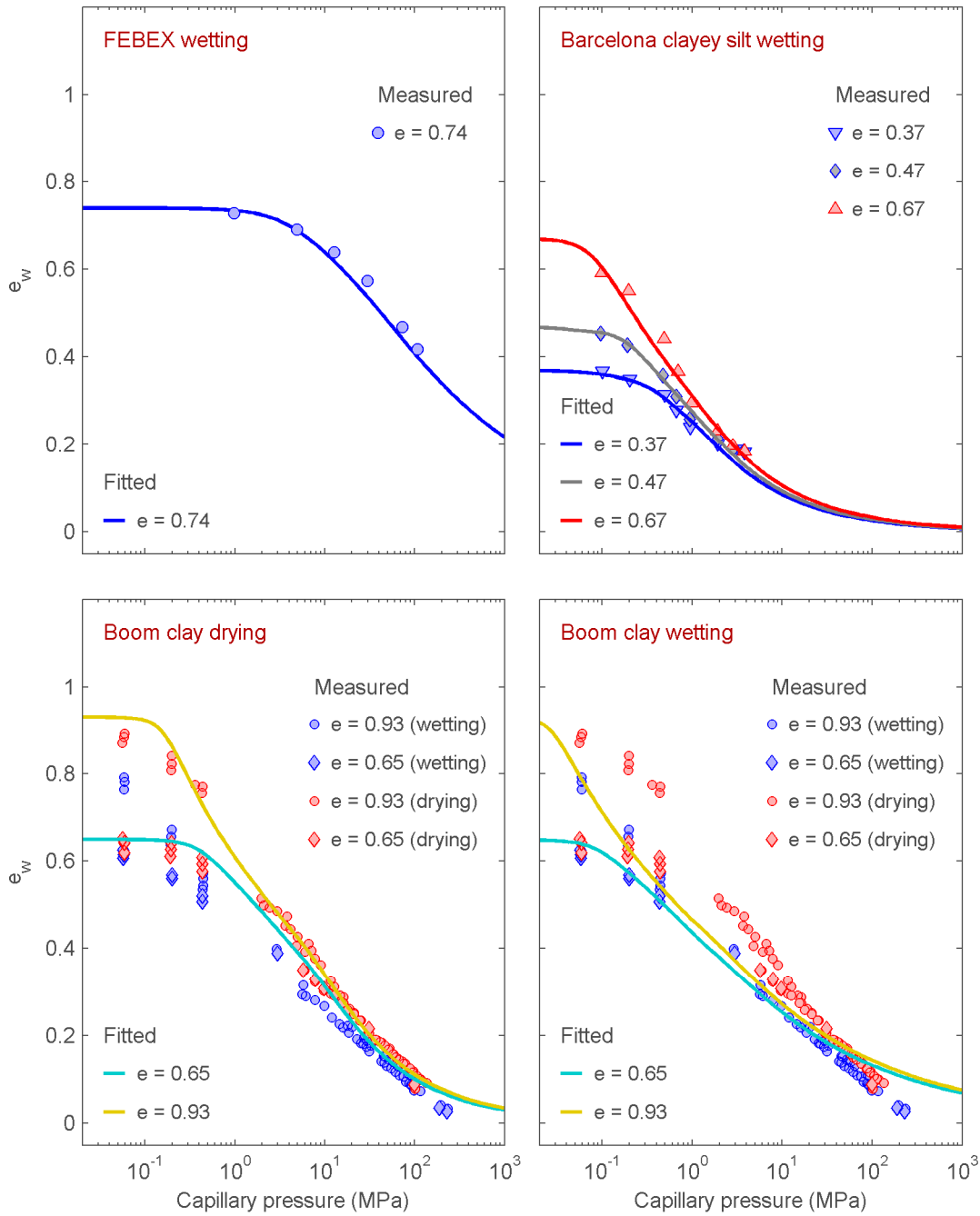


Figure 4-3. Bulk Water Retention as a Function of Capillary Pressure for Several Data Sets Digitized From Figures by Romero, et al. (2011). [1 MPa = 145 psi].

4.2.2 Multicontinuum Permeability

As a first approximation, multicontinuum permeability should be well described using mixture theory. All structure is at a fine scale relative to the typical model grid cell, thus the representative elementary volume is very small compared to the grid cell size. Internal structure should be relatively homogeneous and isotropic, except near wetting fronts.

Assuming mixture theory is appropriate, it should be adequate to simply sum the contributions for each pore space. In essence, this assumes parallel flow paths for each continuum. The reality may be somewhere between the parallel and sequential cases.

$$K_{\alpha}(P_c) = \sum_i e_i K_{\alpha i}(P_c) \quad (4-11)$$

where K_{α} is the product of intrinsic permeability and relative permeability for phase α , and i represents the selected continuum.

The intrinsic permeability for a continuum pore space is strongly dependent on the pore-size distribution, but simply knowing the pore-size distribution is not sufficient. Various correlations can be drawn between the pore-size distribution and intrinsic permeability. For practical purposes, intrinsic permeability can be represented for a reference pore size distribution. Changes to the distribution should then be accounted for using scaling behavior. For example, permeability might be considered proportional to either the void ratio raised to a power or the capillary pressure (uncorrected for surface tension changes) raised to a power. Capillary pressure scaling is reasonable, because the capillary pressure in a tube is inversely proportional to the tube radius and volumetric flux is proportional to the fourth power of the radius. It is important that flexibility is available in $xFl\sigma$ to test different options.

Available gas permeability data on FEBEX pellets (Villar Galicia, 2002) suggest that the macropores between pellets are the dominant component of gas permeability. The measurements were made on a medium constructed by adding a fixed amount of water to dry pellets, then compacting the mixture to a fixed density, thus the gas permeability data are more representative of rewetting conditions than drying conditions. Intrinsic permeability measured with nitrogen gas under dry conditions was 7 orders of magnitude larger than intrinsic permeability measured with liquid water under saturated conditions. Measured intrinsic permeability for both gas and water decreased with increasing dry density. The macropores between pellets permanently disappear under saturated conditions, thus it is likely that the discrepancy between gas and liquid intrinsic permeability would be much smaller if the medium was dried from full saturation.

The relative permeability function for each continuum can be assumed to be consistent with the retention parameters. The liquid relative permeability function using the Mualem approximation (van Genuchten, 1980) is

$$k_{rl}(P_c) = \left[1 + \left(\frac{P_c}{P_0} \right)^n \right]^{-m/2} \left\{ 1 - \left(\frac{P_c}{P_0} \right)^{n-1} \left[1 + \left(\frac{P_c}{P_0} \right)^n \right]^{-m} \right\}^2 \quad (4-12)$$

where the coefficients are the same as the corresponding retention relationships. A similar expression is found using the Burdine approximation. Unlike the retention relationship, $m - 1 + 1/n$ must be an integer for a closed-form relative permeability relationship; if not, k_{rl} does not remain between 0 and 1 over the entire range of capillary pressures. Parameters derived

strictly from retention measurements (e.g., Dieudonné, et al., 2014) may not obey this restriction, but Dieudonné, et al. (2014) presents parameters similar to the Mualem approximation for the micropores and similar to the Burdine approximation for the macropores.

Figure 4-4 illustrates gas and water permeability for FEBEX bentonite, color-coded according to dry density. The gas permeability data are presented by Villar Galicia (2002), and were measured using bentonite granules prepared the same way as the Column Test (described previously). To prepare samples, water was first mixed with the granules and then the mixture was packed to the desired equivalent dry density. This process yields samples more analogous to a wetting curve than a drying curve, thus inter-granule porosity is likely to be significant for relatively dry conditions. The curves use the same retention parameters developed for Figure 4-3, and the measured gas permeability is clearly much larger than the estimated permeability. This disparity is consistent with significant inter-granule porosity even under fairly wet conditions, and may be a substantial help in constraining the volume ratios assigned to different pore scales.

Water is preferentially segregated into the smallest pores in clay material. This preferential segregation may influence liquid relative permeability in multiscale media under dry conditions by limiting flow at contact points. For example, the intra-aggregate pore space may be nearly saturated while the pore space between pellets remains dry. In this case, flow is limited by the small pellet-to-pellet contact area, analogous to reduction in thermal conductivity under dry conditions (see Section 4.2.4). It is not clear whether this effect is significant relative to other hydraulic processes.

Gas relative permeability functions already existing in xFl_0 may be appropriate, except that the Klinkenberg relationship should include scaling based on changes in permeability. It is critical that the pore space at the largest pore scale is considered in deriving the intrinsic and relative permeability functions, because this scale dominates gas movement. Options should be provided for scaling based on both (i) intrinsic permeability and (ii) the product of intrinsic and gas relative permeability.

4.2.3 Multicontinuum Vapor Diffusion

Multicontinuum vapor diffusion should be well described using mixture theory, because the pore spaces at different scales are well connected. The bentonite-granule column test results suggest that thermally driven vapor transport is enhanced as the medium wets. Vapor diffusion primarily occurs in the inter-granule pores, which have much smaller saturations than the intra-pellet pores. Enhanced vapor transport may be due to liquid bridging within the granules. A similar phenomenon might be expected for sand/bentonite mixtures with low bentonite content. Future work should consider this behavior further if vapor diffusion becomes significant.

4.2.4 Multicontinuum Thermal Capacity and Conductivity

Multicontinuum thermal capacity should be well described using mixture theory. Volume-fraction-weighted thermal capacity is quite adequate for this purpose, because thermal capacity is dependent primarily on the specific heat capacity and mass of each phase.

Multicontinuum thermal conductivity is generally nonlinearly dependent on moisture content, but should be well described using mixture theory to weight individual continua when the nonlinear dependence is accounted for. All structure is at a fine scale relative to the typical grid cell size,

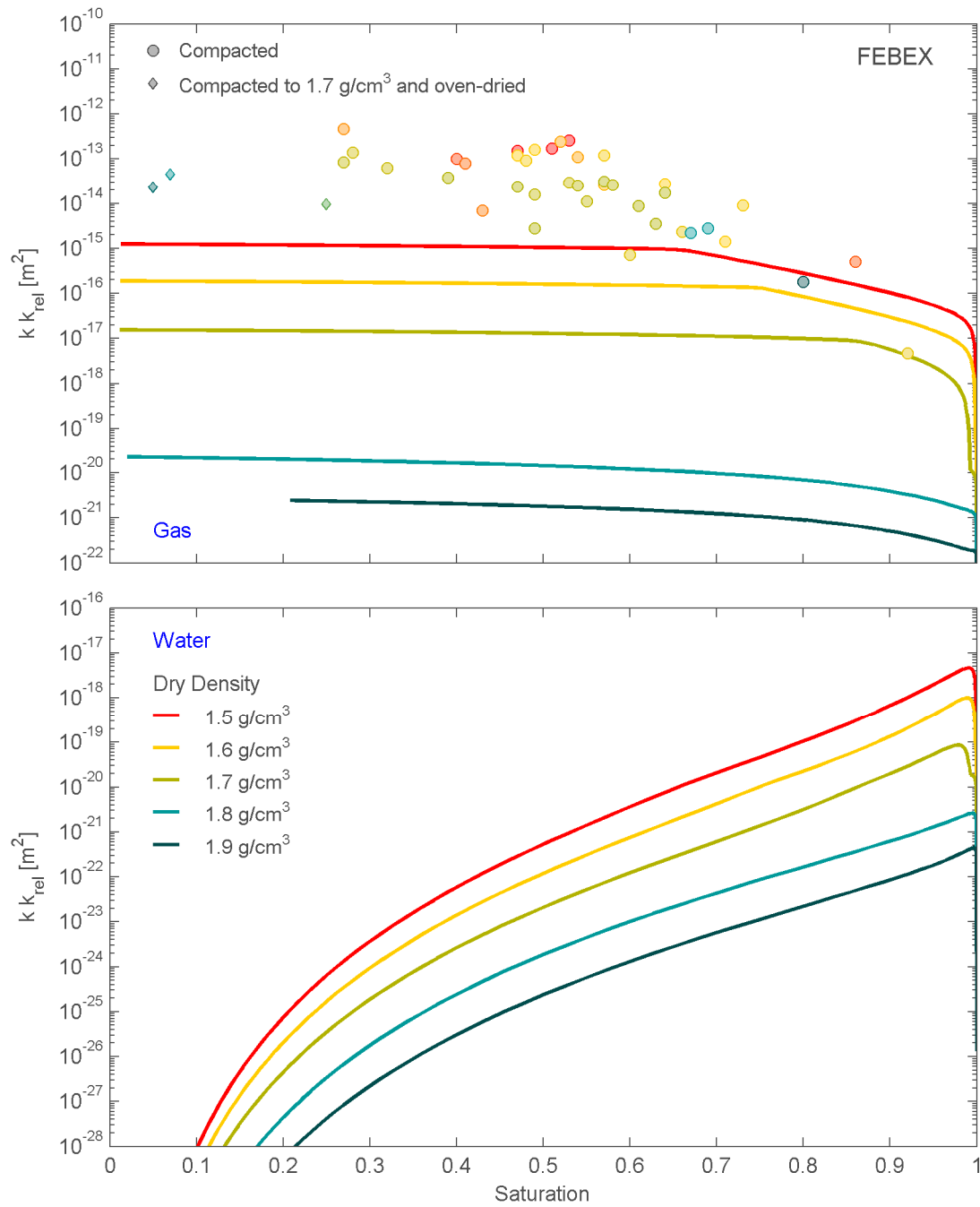


Figure 4-4. Estimated Gas and Liquid Permeability, Scaled by Relative Permeability, as a Function of Saturation for FEBEX Bentonite. Gas Permeability Data Is Presented by Villar Galicia (2002).

thus the representative elementary volume is very small compared to the grid cell size. Internal structure should be relatively homogeneous and isotropic, except near wetting fronts.

For small moisture content, grain-to-grain contact area limits bulk thermal conductivity, because gases have negligibly small thermal conductivity relative to minerals and water. When pendular water becomes prevalent, the pendular water greatly increases the effective grain-to-grain contact area, disproportionately increasing thermal conductivity. This behavior is typically described with a square-root relationship, which *xFlo* includes as an option for describing thermal conductivity, in the form

$$k_t(S_w) = k_{tdry} + S_w^{1/2}(k_{twet} - k_{tdry}) \quad (4-13)$$

where k_t is thermal conductivity, S_w is effective water saturation, k_{tdry} , and k_{twet} are the thermal conductivity values at dry and wet extremes (Somerton, et al., 1974). In this approach, dry and wet thermal conductivities are approximately estimated using

$$k_{twet} = k_{ts}^{1-\varepsilon} k_{tw}^\varepsilon \quad (4-14)$$

$$k_{tdry} = k_{ts}^{1-\varepsilon} k_{ta}^\varepsilon \quad (4-15)$$

where k_{ts} , k_{tw} and k_{ta} are the solid mineral, water, and air thermal conductivities and ε is porosity. Both water and air thermal conductivities increase with temperature (not considered in the *xFlo* model), but this would influence k_t by less than 15 percent over the temperature range in the column test.

Available thermal conductivity data on FEBEX pellets (Villar Galicia, 2002) suggest that the square-root relationship might apply at two or more scales. The data in Figure 4-5 were obtained for FEBEX pellets with the same pellet-size distribution as the MX-80 pellets used in the DECOVALEX test. These pellets were mixed with water then compressed to a volume comparable to the specified dry density, thus are comparable to the initial wetting curve on a fixed-volume sample. The dry density is indicated by color in Figure 4-3. The measured thermal conductivities tend to increase with dry density at a given saturation. For reference, the thermal conductivity is shown in Figure 4-5 for MX-80 bentonite measured under as-received conditions prior to the column test (0.12 W/m-K by Villar, et al., 2012 and 0.45 W/m-K by Wieczorek and Miehe, 2011), as is the thermal conductivity (0.33 W/m-K) staff estimated using the COMSOL models. The MX-80 value measured by Villar, et al. (2012) is distinctly smaller than the FEBEX values, even though the mineral composition is similar, but the Wieczorek and Miehe (2011) value is quite comparable.

Eleven of the Villar Galicia (2002) samples with saturation values between 0.51 and 0.95 were allowed to swell in one direction and examined for thermal conductivity in the directions parallel and perpendicular to swelling. The thermal conductivity is slightly larger parallel to swelling than perpendicular to swelling (8 of 11 samples), but this difference is of the same order of magnitude as experimental variability. The thermal conductivity ranges from -5.2 to 13.1 percent larger in the parallel direction, averaging 4.4 percent larger. The direction of anisotropy appears to depend on water content or saturation. Thermal conductivity within a grain is an arithmetic average between mineral and water parallel to the layers (larger) and a harmonic average perpendicular to the layers (smaller). The bulk thermal conductivity anisotropy is consistent with the clay grains preferentially rotating to align the inter-grain layers perpendicular to the swelling direction at moderate saturation levels, but this effect appears to be negligible near saturation. Linear extrapolation suggests that the effect may induce approximately 20 percent discrepancy under dry conditions.

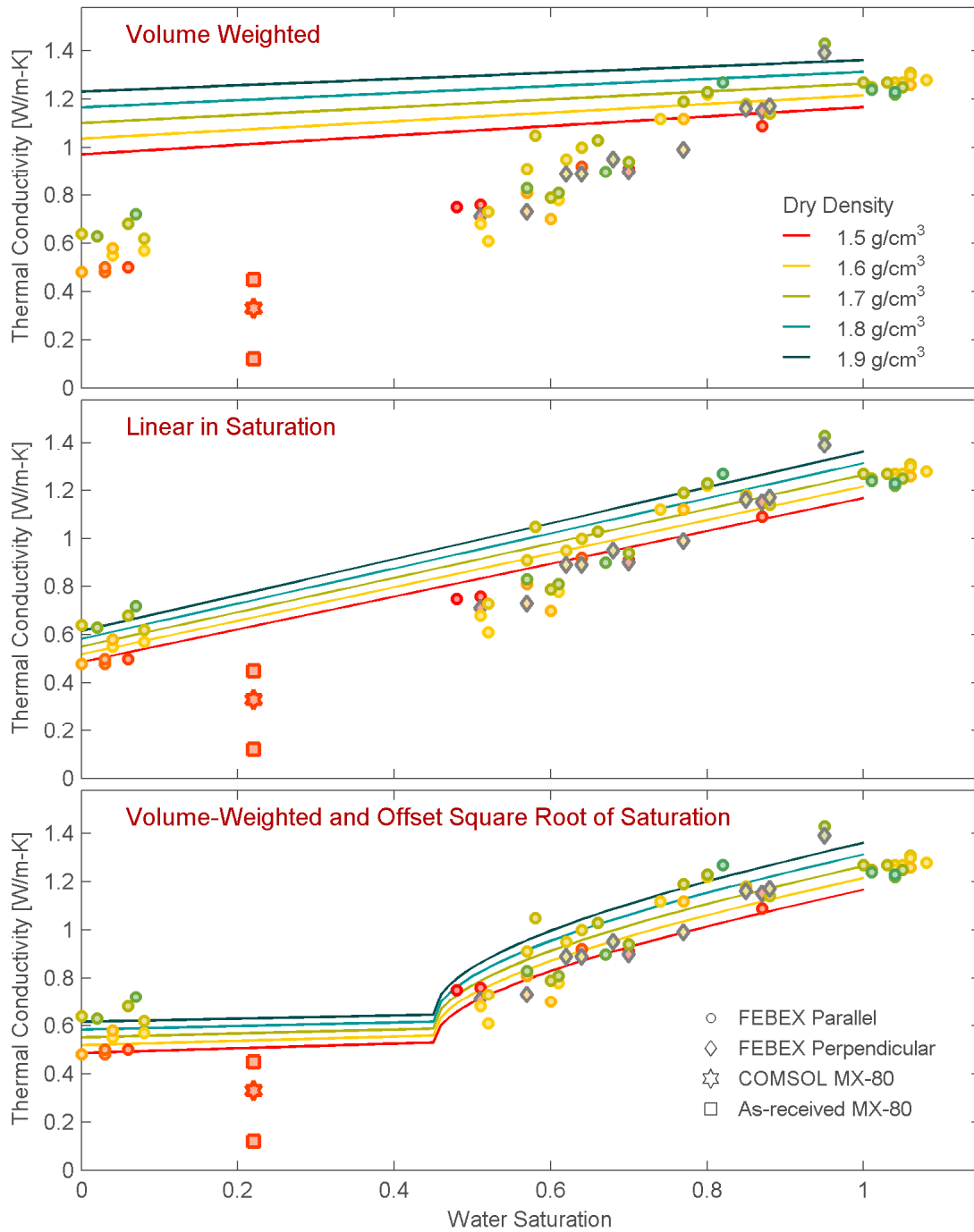


Figure 4-5. Measured Thermal Conductivity for FEBEX Bentonite at Various Void Ratios (Villar Galicia, 2002). Symbols Indicate Measured or Estimated Values and Lines Indicate Fitting Relationships.

For this dataset, the thermal conductivity data at full saturation are reasonably well described by a porosity-weighted mixing model for thermal conductivity of water and minerals, assuming a mineral thermal conductivity of 1.75 W/m-K. A volume-weighted mixing model is shown in Figure 4-3 (top) in the form

$$k_t(S_w) = (1 - \varepsilon)k_{ts} + \varepsilon S_w k_{tw} \quad (4-16)$$

The volume-weighted relationship overestimates the measured data under unsaturated conditions.

One approach to adjusting the thermal conductivity approximately accounts for the interaction of water and solid thermal conductivities by scaling the thermal conductivity of the solid mineral in the volume-weighted mixing model. Figure 4-5 (middle) shows a linear scaling model, equivalent to the model in Eq. (4-13) with the exponent on S_w set to 1, in the form

$$k_t(S_w) = [f + S_w(1 - f)](1 - \varepsilon)k_{ts} + \varepsilon S_w k_{tw} \quad (4-17)$$

where f is a reduction factor for $S_w = 0$ (0.5 in Figure 4-3). This linear scaling overestimates the measured data in the middle of the saturation range. Applying Eq. (4-13) would result in thermal conductivity values larger than the linear relationship for intermediate saturations, deviating even further from the measured data.

The data in Figure 4-3 imply that an approximate square-root relationship may apply for saturations above 50 percent with little sensitivity below 50 percent saturation. This behavior is consistent with a dry inter-pellet pore space constraining thermal conductivity below 50 percent saturation, and closure of the inter-pellet pore space constraining thermal conductivity at large saturations. If this is the case, it is likely that thermal conductivity is hysteretic, because the inter-pellet pore space would not exist during drying from a fully saturated state. Figure 4-3 (bottom) uses a fitting function that assumes the pellet thermal conductivity is described by Eq. (4-16), combined with a square-root relationship describing increasing pellet contact area above a threshold saturation based on Eq. (4-13), in the form

$$k_t(S_w) = k_{tp} \left[f + (1 - f) f_{ramp}^{1/2} \right] \quad (4-18)$$

where f is a reduction factor for $S_w = 0$; k_{tp} is inter-pellet thermal conductivity, which is calculated using Eq. (4-16); and f_{ramp} is a ramp function that goes from 0 to 1 over a subset of the saturation range (from 0.5 to 1 in Figure 4-5). This offset square-root relationship appears to describe the data reasonably well except perhaps in the middle of the saturation range.

4.2.5 Threshold Gradients and Flexible Flux Definitions

Implementation of a threshold-gradient model would require that the $xFlo$ procedure for calculating inter-cell flow be modified to account for reduction in hydraulic gradients as described in Section 4.1.5.

Figure 4-6 illustrates how the threshold gradient reduces flux for various combinations of permeability, α , and applied gradient. The three applied gradients correspond to a pressure difference of 1 MPa applied over a distance of 0.1, 1, and 10 cm [0.03, 0.39, and 3.9 in], respectively, roughly corresponding to different stages of the column test. The vertical axis describes the reduction in flux relative to the linear model of $\alpha = 0$; a value approaching 1 indicates that the threshold gradient effect is negligible. The vertical line corresponds to the

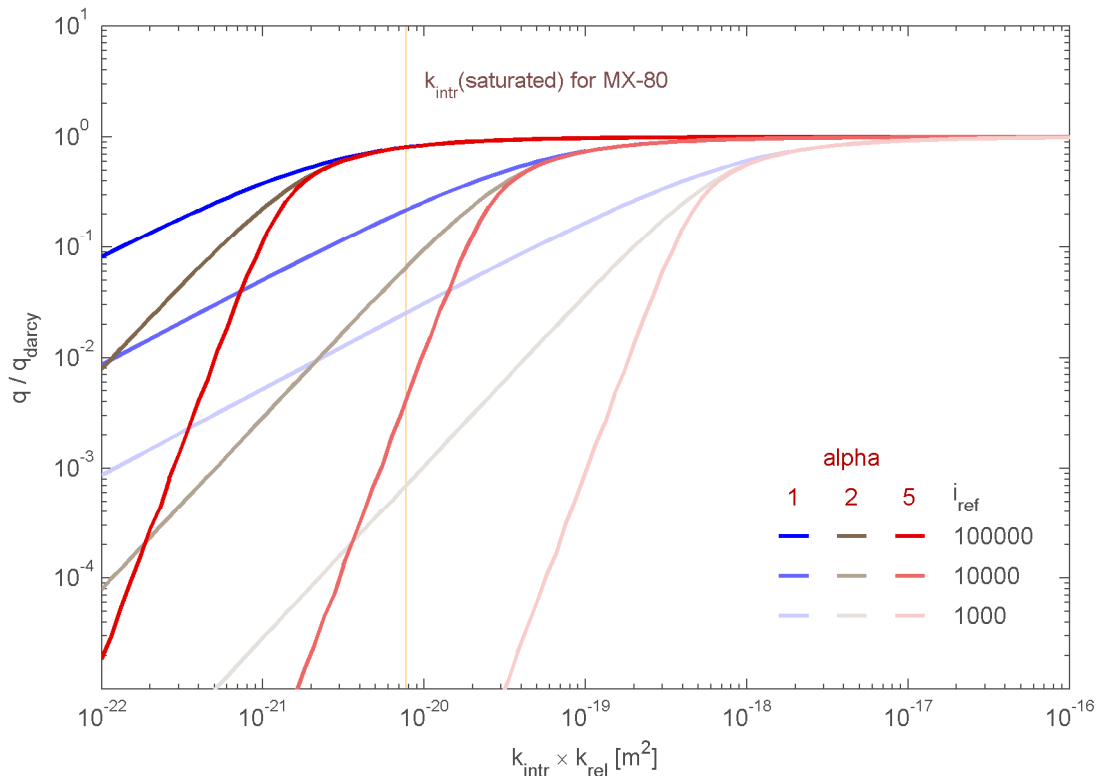


Figure 4-6. Flux Reductions Stemming From Gradient Reduction in Low-Permeability Media for Selected Reference Hydraulic Gradients Using Liu and Birkholzer (2012) Approximations

measured saturated hydraulic conductivity for the dry density in the column test. Based on Figure 4-4, the threshold gradient would be expected to reduce imbibition significantly once the wetting front progresses some fraction of the column length and would strongly reduce imbibition with a unit gradient (gravity drainage). Increasing α does not affect the threshold permeability for which the reduction becomes significant, but does strongly influence the reduction factor for permeability values below the threshold permeability. Figure 4-7 shows the effect of the threshold flux for an isothermal one-dimensional (1-D) semianalytic imbibition model using the base permeability and van Genuchten parameters from the DECOVALEX bentonite column test. The semianalytic model (Stofoff and Pinder, 1992) is based on moving a discretized set of saturation values using their characteristic velocity. The characteristic velocity is determined using the relationship

$$v(\theta) = \frac{(q_p - q_m)}{(\theta_p - \theta_m)} \quad (4-19)$$

where v is the velocity, q is flux, θ is volumetric water content, and subscripts p and m represent discretized values on either side of the characteristic. The model is implemented in MATLAB. In this semi-infinite model, (i) the upper boundary is held near saturation, (ii) the initial saturation is 0.2 throughout the domain except for a linear ramp from maximum to minimum saturation in the upper millimeter of the domain, and (iii) the saturation profile moves based on gravity and pressure gradients.

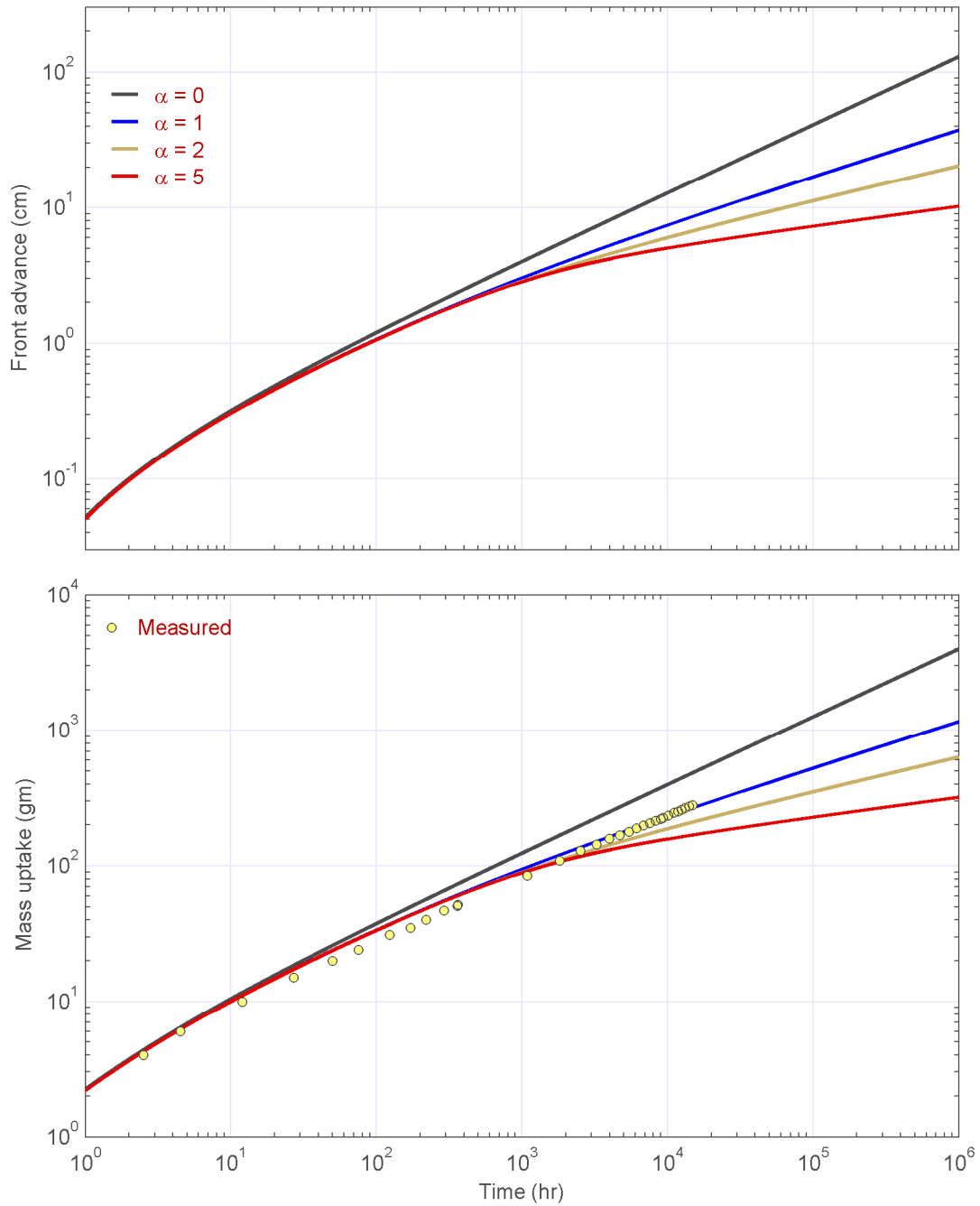


Figure 4-7. Wetting-Front Advance (Top) and Total Mass Uptake (Bottom) for a Semi-Analytic Isothermal Model With Parameters for the DECOVALEX Bentonite-Pellet Column. Measured Uptake Closely Aligns With the Swartzendruber (1961) Model. [1 cm = 0.39 in]

The threshold gradient has no effect at early times because of the steep pressure gradient. The threshold gradient begins to influence imbibition between 10 and 100 hour after start of injection with no differentiation between the various values for α . The simulation results for the various values for α begin to separate after 500 to 1,000 hours.

Currently *xFlo* does not permit flexible adjustment of fluxes for boundary conditions and assumes that the medium is isotropic for all phases. In the process of modifying the model to account for reduced hydraulic gradients, it would be useful to address these limitations. Should resources permit, it would also be useful to add capability for simple radiation boundary conditions, allowing better interpretation of column tests involving heating. The radiation boundary condition is important for representing energy fluxes with substantial temperature differences across an air gap, thus it is unlikely that the radiation boundary condition will be important for field experiments.

4.3 Potential Modifications to *xFlo*

In working with the DECOVALEX column test and planning for the HE-E test, staff have identified several suggestions where improving *xFlo* would aid in analysis of the HE-E test. Some areas represent improved program structure for ease of use, while others address fundamental representation of TH processes. Not all of the suggested modifications are feasible within the near future, and implementation strategies remain to be developed. Table 4-1 lists these areas to summarize current thinking regarding model-capability needs. The suggested improvements to input and output listed in Table 4-1 are desirable for improved analysis capabilities and better documentation.

The improvements to account for reversible multiscale swelling and threshold gradient directly address pneumatic, hydraulic and thermal conductivities that are demonstrably not well represented with the current constitutive relationships available in *xFlo* (see Section 4.2). Staff are actively pursuing strategies for developing improved constitutive relationships.

Staff envisions implementing alternative constitutive models either as FORTRAN routines or as input lookup tables, depending on model complexity.

The suggested improvement with respect to gridding stems from experience with the column test. It is relatively straightforward to simplify a FLAC grid into an *xFlo* grid but less so to expand an *xFlo* grid into a FLAC grid. The simple geometry of the column test allowed the grid generation for both to be done using the same specification; however, once the FLAC grid deforms due to swelling the *xFlo* grid is no longer consistent. It may not be as straightforward to develop an *xFlo* grid that is used to create a FLAC grid for the more complex HE-E test, and deformation may be more extensive in the HE-E test. If deformation is significant, it makes sense to maintain consistency between the grids driven by FLAC. Depending on the details of the TH and mechanical deformation model, which are currently being discussed among the staff, grid coordinates and perhaps swelling pressure may be the only information necessary to pass from FLAC to *xFlo*.

The suggested improvement with respect to the coordinate system also stems from experience with the column test. It may not be practical to enforce an exponentially expanding grid in the radial direction, which is required for best computational results in *xFlo*. If this is not practical, it may be appropriate to explicitly account for the radial coordinate system in the *xFlo* formulation.

Table 4-1. Areas Identified for Potential <i>xFlo</i> Augmentation		
Modification	Priority	Description
Flexible Input	Moderate	Allow hard-coded parameters to be input Provide command-driven options Provide scale and shift for input variables (unit conversion)
Flexible Output	Moderate	Allow user-selected parameter outputs Snapshots (output at all cells at selected times) Traces (output at selected cells at all times) Provide scale and shift for output variables (unit conversion)
Reversible Multiscale Swelling	High	Two- and three-continuum models accounting for changes in TH properties due to changes in water content and compaction
Threshold Gradient	High	Account for surface forces that reduce the effective liquid pressure gradient
Irreversible Swelling	Low	Not important if only rewetting is considered
Lagrangian Grid	High	Needed for radial swelling in small grid cells
Explicit Coordinate System	Moderate	<i>xFlo</i> does not explicitly consider radial coordinates, so the calculations are inaccurate unless exponentially expanding grids are used in the radial direction

4.4 Proposed Modifications to Link *xFlo* and FLAC

The *xFlo* and FLAC models run on different operating systems (Linux and Windows, respectively). Simulations for the column test were run in a one-way coupling mode, with the full set of *xFlo* simulations run to completion and selected intermediate output passed to FLAC for a subsequent set of simulations. This approach should be adequate for problems that have minimal deformation. Under the current approach, input sets are prepared by a set of MATLAB preprocessor and postprocessor routines. A separate *xFlo* simulation is run whenever the boundary conditions change significantly, resulting in sequence of four *xFlo* simulations for the column test. For the column test, the execution process was largely automated with a few manual steps.

The column test execution includes a series of automated steps to create, run, and interpret *xFlo* simulations, then transfer the files for FLAC execution.

- A MATLAB shell loops over a series of selected parameters
- For each loop, the shell drives preprocessor routines that create (i) four separate *xFlo* input decks and (ii) associated Linux shell scripts to drive the four *xFlo* simulations
- The shell copies the created files to separate directories on the Linux cluster
- The shell pauses until manual input confirming that the four *xFlo* simulations have ended
- A Linux shell driver is manually started when all files have been copied to the Linux cluster

- The driver sequentially executes a Linux shell script for each of the four *xFlo* simulations, copying output from one simulation to provide input to the next
- Once all *xFlo* simulations are complete, the paused MATLAB shell is allowed to continue
- The MATLAB shell transfers all files from the Linux cluster back to Windows
- Postprocessor MATLAB shell routines transform the *xFlo* output into FLAC input
- The FLAC input files are transferred to the appropriate computer for FLAC execution
- The MATLAB shell repeats the loop to create the next set of *xFlo* input files

In this sequence, the two manual steps are (i) initiating a Linux shell script to run an *xFlo* sequence and (ii) notifying the MATLAB shell that the Linux shell has terminated. These manual steps can be eliminated using temporary files to flag whether a sequence should be initiated or has terminated. In the updated process, instead of manually starting a Linux shell to run an *xFlo* sequence, a Linux shell is started manually, but the Linux shell continues to loop through *xFlo* sequences until a termination signal is provided.

- The MATLAB shell copies the *xFlo* files to the Linux cluster, creates a temporary Linux file to signal that the files are ready to run, and waits while the file exists
- The Linux shell waits until the temporary file exists or a termination signal is given, runs an *xFlo* sequence, signals that the sequence is done by removing the file, and repeats to start waiting again
- The MATLAB shell continues processing once the file is removed, looping as many times as necessary
- The MATLAB shell sends the termination signal to the Linux shell

The same process can be easily adapted to drive FLAC in an automated fashion. With the MATLAB shell running on the machine dedicated to FLAC, the shell simply calls the FLAC preprocessing routines, executes FLAC as a command-line system call from within MATLAB, and post-processes the FLAC routines for input to *xFlo*. These steps are all easily automated.

There is a certain amount of unavoidable overhead involved with copying files from machine to machine, but typically this overhead is small relative to execution time for a simulation. The execution process also involves checking for *xFlo*-related files after timed pauses. The duration of the pauses should be set to be a small fraction of the typical execution time to minimize the wait time, but frequent checking does not impose a computational burden because checking only occurs when the machine is otherwise idle.

5 SUMMARY

Task B1 of the current phase of **Development of Coupled Models and Their Validation Against Experiments (DECOVALEX) (D-2015)** focuses on understanding thermohydrological-mechanical (THM) processes in bentonite buffer and argillaceous host rock, using information and data from field tests at Mont Terri Underground Research Laboratory (URL) in Switzerland. Modeling THM processes in the buffer, as observed in the column test, was the second step of Task B1 and is the focus of this report.

This report summarizes a current snapshot of progress related to developing (i) a numerical model for the column test for granular bentonite and (ii) an approach to represent thermohydrological (TH) behavior of swelling clays at a pore-scale (macro- and micropores) in *xFlo*. As modeling is an iterative process, insights gained in this report and in subsequent HE-E test modeling may be used to update the column test model in the future.

The laboratory column test was designed to mimic the boundary conditions for the buffer material in the HE-E test by prescribing the temperatures of the heater (at the bottom) and a room-temperature cooling bath (at the top), and providing a source of hydration (host rock rewetting) at the top. The test used a Teflon column with a nominal internal diameter of 7 cm [2.76 in] and length of 50 cm [19.7 in]. Semi-cylindrical steel sheets covered the Teflon to prevent deformation caused by bentonite swelling. The outer wall of the cell was wrapped in insulation wool to reduce lateral heat losses. The bottom heater was set to 100 °C [212 °F] for the first 3500 hours and then increased to 140 °C [284 °F] until the end of the experiment. Substantial lateral heat losses were observed through the dense foam initially used as insulation. Additional insulation (Superwool, with an outer layer of ISOVER material near the heater) was added after the first approximately 1,500 hours. The hydration phase, from ~5,000 hours to 19,000 hours, allowed water to imbibe into the bentonite from a pressure bladder surcharged with a pressure of 0.01 MPa [0.1 bar]. Three probes, located at various distances from the heater, measured temperature and relative humidity. Water intake and axial pressure on the top of the cell were also measured.

The THM model was implemented in a two-dimensional (2-D) axisymmetric coordinate system centered along the axis of the column. The numerical modeling approach coupled two existing simulators, *xFlo* (which models TH processes) and FLAC (which models mechanical processes with a user-defined constitutive model for unsaturated expansive soils). In addition, COMSOL Multiphysics was used to develop a model that represented the experimental apparatus and thermal processes in detail without considering moisture redistribution. The COMSOL model provided insights related to the effect of different thermal boundary condition treatments and thermal properties, and provided guidance for selection of the domain and boundary conditions used for *xFlo* thermal analyses.

Comparisons of measured temperature and relative humidity with model results at three probe locations indicated that *xFlo*, in general, is able to adequately represent the evolution of the moisture redistribution in response to heat and hydration. Using the temperature- and capillary-pressure-dependent vapor pressure and adjusting the capillary pressure to account for changes in temperature enables appropriate characterization of vapor transport in bentonite during the heating phase. Determining an appropriate value for the thermal conductivity for bentonite was difficult because of uncertainties related to heat loss and the dominant effect of highly conductive steel reinforcement sheets in the laboratory setup. The COMSOL model suggested a value of 0.33 W/m/K, while the *xFlo* model suggested a value of 0.12 W/m/K. The Klinkenberg relationship was used to increase the gas relative permeability by several orders of

magnitude in order to represent the increased pore space available to gas in the dry media; this step was necessary to match the temperature and relative humidity measurements during the thermal phase.

Comparison of water intake measurements indicated that *xFlo* poorly represented moisture redistribution during the hydration stage using the initial top boundary condition specification. The hydration stage features large changes in hydraulic conductivity as the granular bentonite swells. A subsequently developed semianalytic moisture redistribution model calculated inflow rates similar to the measured rates without adjusting the hydraulic parameters, thus the discrepancy between *xFlo* output and measured values was identified to be due to an input or implementation error associated with the injection boundary condition. Placing a porous plate between the inlet nozzle and the bentonite, a boundary representation better matching the experimental conditions, yielded intake rates quite similar to the measured rates. The semianalytic approach provides a good comparison model to identify the source of the discrepancy between *xFlo* output and measured values, and allows rapid testing of potential modifications to constitutive relationships in *xFlo* that may better represent the properties of swelling media.

Geomechanical calculations used the initial boundary representation, as the porous-plate boundary representation was not implemented until after the DECOVALEX workshop. Comparing the measured and calculated axial pressure suggests that the geomechanical model qualitatively represents the observed behavior (i.e., the changes in axial pressure), although the response is obscured by the poor representation of moisture redistribution during the hydration stage without the porous plate included in the model. Parameter adjustments may be necessary once the geomechanical model is revisited using hydrological model results that account for the porous plate.

The conceptual model for TH processes in swelling clays was examined to consolidate insights from the Column Test and prepare for the full-scale simulations of the HE-E test. Available data suggest that buffer media features several distinct pore scale modes, including inter-layer pores, inter-grain pores, and intra-aggregate pores. An even larger pore scale may exist in sand/bentonite mixtures and between bentonite granules and pellets prior to wetting. There may be distinctly different hydraulic responses for each of the pore scale modes, resulting in constitutive relationships that may not be well described with models based on a single mode. Retention relationships that agree reasonably well with observations are currently being developed in the literature based on bimodal pore-size distributions, but these relationships less successfully represent gas conductivity, water conductivity, and thermal conductivity because (i) water preferentially segregates into the smallest pore scales, (ii) gas and liquid properties are strongly affected by solid interactions at small pore sizes, and (iii) pore-size distributions change as the water content changes in swelling media. An equivalent continuum approach that considers multimodal pore-size distributions and their response to swelling offers promise of consistently accounting for processes active over the range of pore scales.

Several further modifications to the modeling approach are necessary or desirable to complete HE-E test modeling. The link between FLAC and *xFlo* remains to be formalized, which will require software development (i) augmenting *xFlo* and FLAC input and output, and (ii) performing file manipulations across the network. Staff are in the process of defining the necessary data to be passed between models based on the needs of the constitutive models under consideration, but all data under consideration are readily available from the respective simulators. All input files for the Column Test were generated using MATLAB, and prototype file

manipulations across the network were successfully performed using MATLAB as a driver; these routines will be augmented to fully couple *xFlo* and FLAC.

6 REFERENCES

- Cui, Y.-J., A.M. Tang, C. Loiseau, and P. Delage. "Determining the Unsaturated Hydraulic Conductivity of a Compacted Sand-Bentonite Mixture Under Constant Volume and Free-Swell Conditions." *Physical and Chemistry of the Earth*. Vol. 33. pp. S462–S471. 2008.
- De Bock, C., J.-M. Bosgiraud, B. Breen, M. Johnson, T. Rothfuchs, H. Weber, and P. Van Marcke. "Deliverable 6 Module 1 Work Package 6, Module 1 Final Report." Contract Number FI6W–CT–2004–508851. Chatenay-Malabry Cedex, France: Engineering Studies and Demonstrations of Repository (ESDRED). January 30, 2009.
- Dieudonné, A.C., R. Charlier, S. Levasseur, G. Della Vecchia, and C. Jommi. "Evolution of Clay Fabric and Water Retention Properties Along Hydromechanical Stress Paths." 8th European Conference on Numerical Methods in Geotechnical Engineering. NUMGE 2014. Delft; Netherlands, 18 June 2014 through 20 June 2014. Vol. 2. pp. 971–975. 2014
- Dieudonné, A.C., S. Levasseur, R. Charlier, G. Della Vecchia, and C. Jommi. "A Water Retention Model Including the Effects of Structure." Proceedings of the Groupe De Contact FNRS Géomécanique, Ouvrages, Couplages, Brussels, Belgium, January 31, 2013. Belgique, Belgium: Université de Liège. 2013. <http://www.facsu.ulg.ac.be/upload/docs/application/pdf/2013-11/07_dieudonne_gcfnrns_31012013.pdf> (18 August 2014).
- Gaus, I., K. Wiczorek, K. Schuster, B. Garitte, R. Senger, R., Vasconcelos and J. C. Mayor "EBS Behaviour Immediately After Repository Closure in a Clay Host Rock: HE-E Experiment (Mont Terri URL)". Geological Society. London. Special Publications. Doi 10.1144/SP400.11. 2014.
- Ho, C.K. "Vapor Transport Processes". *Gas Transport in Porous Media*. C.K. Ho and S.W. Webb, eds. Dordrecht, The Netherlands: Springer. 2006.
- Holmboe, M., S. Wold, and M. Jonsson. "Porosity Investigation of Compacted Bentonite Using XRD Profile Modeling." *Journal of Contaminant Hydrology*. Vol. 128. pp.19–32. 2012.
- Klinkenberg, L.J. "The Permeability of Porous Media to Liquids and Gases." *API Drilling and Production Practice*. pp. 200–213. 1941.
- Komine, H. "Predicting Hydraulic Conductivity of Sand–Bentonite Mixture Backfill Before and After Swelling Deformation for Underground Disposal of Radioactive Wastes." *Engineering Geology*. Vol. 114. pp. 123–134. 2010.
- Liu, H.-H. and J. Birkholzer. "Report on Hydrologic Flow in Low-Permeability Media." LBNL–6634E. Berkeley, California: Lawrence Berkeley National Laboratory. November, 2013.
- _____. "On the Relationship Between Water Flux and Hydraulic Gradient for Unsaturated and Saturated Clay." *Journal of Hydrology*. Vol. 475. pp. 242–247. 2012.
- Low, P.F. "The Swelling of Clay. II. Montmorillonites." *Soil Science Society of America Journal*. Vol. 44, No 4. pp. 667–676. 1980.
- Mualem, Y. "A New Model for Predicting the Hydraulic Conductivity of Unsaturated Porous Media." *Water Resources Research*. Vol. 12, No. 3. pp. 513–522. 1976.

Nowamooz, H. and F. Masrouri. "Relationships Between Soil Fabric and Suction Cycles in Compacted Swelling Soils." *Engineering Geology*. Vol. 113. pp. 444–455. 2010.

Ofoegbu, G., B. Dasgupta, C. Manepally, and R. Fedors. "Thermal-Hydrological-Mechanical Modeling of a Saturated Clay Shale Report on HE-D Test Modeling." San Antonio, Texas: Center for Nuclear Waste Regulatory Analyses. (In review) 2013a.

Ofoegbu, G., B. Dasgupta, C. Manepally, H. Basagaoglu, and R. Fedors. "Modeling Swelling and Swelling Pressure in Expansive Clays." 2013 International High-Level Radioactive Waste Management Conference, Albuquerque, New Mexico, April 28–May 2, 2013. La Grange Park, Illinois: American Nuclear Society. 2013b.

Painter, S. "xFlo Version 1.0 β User's Manual." San Antonio, Texas: Center for Nuclear Waste Regulatory Analyses. 2006.

Philip, J.R., and D.A. de Vries. "Moisture Movement in Porous Materials Under Temperature Gradients." *Transactions of the American Geophysical Union*. Vol. 32 No. 2. pp. 222–232. 1957.

Pruess, K., C. Oldenburg, and G. Moridis. "TOUGH2 User's Guide, Version 2.1." Report LBNL–43134. Berkeley, California: Lawrence Berkeley National Laboratory. 2012. <http://esd.lbl.gov/files/research/projects/tough/documentation/TOUGH2_V2_Users_Guide.pdf> (5 August 2014)

Rizzi, M., A. Seiphooori, A. Ferrari, D. Ceresetti, and L. Laloui. "Analysis of the Behaviour of the Granular MX-80 Bentonite in THM-Processes." AN 12-102. Wetingen, Switzerland: Nagra. 2012.

Romero, E. "A Microstructural Insight Into Compacted Clayey Soils and Their Hydraulic Properties." *Engineering Geology*. Vol. 165. pp. 3–19. 2013.

Romero, E., G. Della Vecchia, and C. Jommi. "An Insight Into the Water Retention Properties of Compacted Clayey Soils." *Geotechnique*. Vol. 61, No. 4. pp. 313–328. 2011.

Rutqvist, J., F. Chen, and J. Birkholzer. "Modeling of THM Column Experiment on Bentonite for DECOVALEX-2015 Task B1." DECOVALEX 2015–4th Workshop, November 11–15, 2013. Mont Terri, Switzerland. 2013.

Seiphooori, A., A. Ferrari, and L. Laloui. "An Insight Into the Water Retention Behaviour of MX-80 Granular Bentonite." International Conference on the Performance of Engineered Barriers. February 6–7, 2014. Hannover, Germany. 2014. <http://infoscience.epfl.ch/record/196669/files/Seiphooori%20et%20al.%20PEBS_2014.pdf?version=1> (5 August 2014)

Somerton, W.H, J.A. Keese, and S.C. Chu. "Thermal Behaviour of Unconsolidated Oil Sands." *Society of Petroleum Engineers Journal*. Vol. 14. pp. 513–521. 1974.

Stoehoff, S. A. and G. F. Pinder. "A Boundary Integral Technique for Multiple-Front Simulation of Incompressible, Immiscible Flow in Porous Media." *Water Resources Research*. Vol. 28, No 8. pp.1,067–1,076. 1992.

Swartzendruber, D. "Modification of Darcy's Law for the Flow of Water in Soils." *Soil Science*. Vol. 93. pp. 22–29. 1961.

Tanikawa, W. and T. Shimamoto. "Comparison of Klinkenberg-Corrected Gas Permeability and Water Permeability in Sedimentary Rocks." *International Journal of Rock Mechanics & Mining Sciences*. Vol. 46. pp. 229–238. 2009.

Tuller, M. and D. Or. "Hydraulic Functions for Swelling Soils: Pore Scale Considerations." *Journal of Hydrology*. Vol. 272. pp. 50–71. 2003.

van Genuchten, M.T. "A Closed-Form Equation for Predicting the Hydraulic Conductivity of Unsaturated Soils." *Soil Science Society of America Journal*. Vol. 44. pp. 892–898. 1980.

Villar Galicia, M.V. "Thermo-Hydro-Mechanical Characterization of a Bentonite From Cabo de Gata. Publicación Técnica 04/2002. Madrid, Spain: Empresa Nacional de Residuos Radiactivos: June, 2002.

Villar, M.V., P.L. Martin, R. Gomez-Espina, F.J. Romero, and J.M. Barcala. "THM Cells for the HE-E Test: Setup and First Results." PEBS Report D2.2.7a. Madrid, Spain: Long-Term Performance of Engineered Barriers Systems Project. 2012.

Villar, M.V., P.L. Martin, R. Gomez-Espina, and F.J. Romero. "Long-term THM Tests Reports: THM Cells for the HE-Test: Update of Results Until February 2014." PEBS Report D2.2-7.3. Madrid, Spain: Long-Term Performance of Engineered Barriers Systems Project. 2014.

Warkentin, B.P., G.H. Bolt, and R.D. Miller. "Swelling Pressure of Montmorillonite." *Soil Science Society of America Proceedings*. Volume 21. pp. 495–497. 1957.

Wieczorek, K. and R. Mieke. "Measurement of Thermal Parameters of the HE-E Buffer Materials." Deliverable D2.2-5 of the PEBS Project. European Commission. 2011.

Xie, M., W. Wang, J. de Jonge, and O. Kolditz. "Numerical Modelling of Swelling Pressure in Unsaturated Expansive Elasto-Plastic Porous Media." *Transport in Porous Media*. Vol. 66. pp. 311–339. 2007.

Xie, M., S. Bauer, O. Kolditz, T. Nowak, and H. Shao. "Numerical Simulation of Reactive Processes in an Experiment With Partially Saturated Bentonite." *Journal of Contaminant Hydrology*. Vol. 83. pp. 122–147. 2006.